SU-SEL-71-055

ELF Propagation in the Plasmasphere Based on Satellite Observations of Discrete and Continuous Forms

by

J.L.R. Muzzio

December 1971

Technical Report No. 3439-2

Prepared under

National Aeronautics and Space Administration

Grant NGR-05-020-288
Grant NGL-05-020-008
Contract NAS 5-3093

RADIOSCIENCE LABORATORY

STANFORD ELECTRONICS LABORATORIES

STANFORD UNIVERSITY · STANFORD, CALIFORNIA

SEL-71-055

ELF PROPAGATION IN THE PLASMASPHERE BASED ON SATELLITE OBSERVATIONS OF DISCRETE AND CONTINUOUS FORMS

by

J. L. R. Muzzio

December 1971

Technical Report No. 3439-2

Prepared under

National Aeronautics & Space Administration

Grant NGR-05-020-288
Grant NGL-05-020-008
Contract NAS 5-3093

Radioscience Laboratory

Stanford University Stanford, California

ABSTRACT

Analysis of data from the Stanford University ELF and VLF experiment on OGO-4 satellite has revealed new types of ion whistlers and also some new features of low to medium latitude ELF hiss not previously identified. The ion whistlers identified and interpreted are the 1^- proton whistler, the ion-cutoff whistler and combinations of both forms. The observations of ELF hiss permitted the identification of a hiss band and its interpretation in terms of propagation effects, using computer ray tracings. The band exhibits the previously observed low frequency cutoff characteristics of downward propagating hiss and also a peculiar upper cutoff in the vicinity of 600 Hz, which is nearly independent of the satellite altitude ($\sim$ 430 to 900 km) and latitude above $\sim 15^{\circ}$. This hiss band is called band-limited ELF hiss, or simply BLH. It is observed between $\sim 10^{\circ}$ and $\sim 55^{\circ}$ dipole latitude, where there is merging of the nearly constant upper cutoff and the increasing (with latitude) lower cutoff. Around $\sim 10^{\circ}$ dipole latitude the BLH exhibits a sloping upper cutoff decreasing in frequency toward the equator (equatorial erosion). The BLH is seen most frequently from $\sim$ 0600 to $\sim$ 2200 LT, although some examples have been found between 0200 and 0500 LT, with less intensity. In the range 0 to 3 kHz and up to $\sim 55^{\circ}$ dipole latitude the BLH is the strongest signal observed. Its peak amplitude may reach $2 \times 10^{-4}\ \gamma^2/\text{Hz}$ between 40° and 50° dipole latitude during daytime ($\sim$ 1000 LT). After prolonged periods of low magnetic activity ($K_p \leq 2$) the upper cutoff may decrease to as low as 420 Hz but recovers about one day after a sharp increase in magnetic activity, such as a sudden commencement. The decrease and smearing of the lower cutoff of the background hiss, observed at latitudes greater than about 58°, indicates the presence of the light ion trough.

The similarity of the upper cutoff frequency on the two sides of the equator is taken as conclusive evidence that the source lies on the equator. An equatorial source near $L = 4$ and large initial wave normal angles were found adequate to explain the characteristics of the BLH as well as some of the observations of ELF hiss previously reported. Two possible generation mechanisms, Cerenkov and Doppler-shifted cyclotron (DSC), are briefly examined. For the Cerenkov mechanism electrons of energy of the order of 1 kev are required, while for the Doppler-shifted cyclotron mechanism, much higher energies, of order 1 Mev are needed. For a typical distribution of energetic particles the number density of electrons for the Cerenkov mechanism is of order 10^4 times greater than that for the DSC mechanism. However, in either case a certain amount of emission coherency or amplification is necessary to obtain the observed power fluxes.

The propagation of electromagnetic waves in a nonhomogeneous anisotropic medium is examined from the point of view of geometrical optics. In particular, the propagation of ELF waves in the magnetosphere is described in terms of the electron and ion densities and the intensity and inclination of the earth's magnetic field. The analysis of the variations of wave normal angle along the ray path is extended to include the effects of ions. A comparison of the relative importance of each of the above parameters in controlling the orientation of the wave normals is made in the region of the magnetosphere where most of the ion whistlers have been detected.

CONTENTS

CONTENTS (cont.)

TABLES

ILLUSTRATIONS

ILLUSTRATIONS (cont.)

ILLUSTRATIONS (cont.)

ILLUSTRATIONS (cont.)

ACKNOWLEDGMENTS

The author wishes to thank R. A. Helliwell, J. Katsufrakis, J. J. Angerami, T. Bell and C. Park for helpful discussions related to this work. The use of a tridimensional raytracing program developed by F. Walter is also acknowledged.

The research for this work was supported by the National Aeronautics and Space Administration under contract NAS 5-3093, grant NGR-288 and grant NGL-008. Computer facilities were sponsored in part by the Office of Computer Sciences of the National Science Foundation under grant NSF GP-948.

I. INTRODUCTION

A. PURPOSE

The purpose of the present work is to discuss and interpret a certain class of electromagnetic waves occurring naturally in the earth's magnetosphere. They are found in the ELF range of frequencies (100 Hz to 3000 Hz) and are detected aboard artificial satellites. They include phenomena both whistlers and hiss and are interpreted in terms of the known properties of the propagation of electromagnetic waves in anisotropic dispersive media.

The propagation of plane electromagnetic waves in a dispersive medium can be described in terms of the quantity known as refractive index. This quantity, defined by the ratio of the speed of light in a vacuum to the magnitude of the actual phase velocity of the wave considered, is a function of the characteristics of the medium and, of course, of the frequency of the wave. When the medium is the earth's upper atmosphere, which is a composite semi-ionized gas, the propagation problem becomes particularly interesting due to the anisotropic characteristics of this medium. This means that the phase velocity of a plane wave is not only a function of position, but also of the direction of propagation.

The anisotropy in the magnetosphere is caused by the presence of the earth's magnetic field, which puts some constraints on the movements of the charged particles (electrons and ions) that constitute the ionized atmosphere. When these particles are displaced from their positions of equilibrium, they will describe curved trajectories around magnetic field lines. The projection of this trajectory on a plane perpendicular

to the magnetic field direction is a circular motion with an angular frequency (gyrofrequency) that depends on the particle's e/m ratio and on the field intensity. It is therefore to be expected that when these particles are set in motion by the electric field of a passing wave, they will have some effect upon the propagation of such a wave. When the frequencies of interest are much higher than the ion gyrofrequencies, the ions may be considered as stationary in comparison with the much lighter electrons, so their influence may be neglected. However, when the frequencies are in the range of the ion gyrofrequencies, that approximation is no longer valid. The so called ELF range of frequencies falls under this category and the presence of the ions in the higher atmosphere (oxygen, helium and hydrogen) contributes appreciably to the dispersive properties of the medium.

B. BACKGROUND OF THE PROBLEM

The natural phenomena to be studied in this work belong to two broad categories known as:

1. Whistlers, which are dispersed forms of electromagnetic energy produced in the atmosphere by lightning discharges.
2. Hiss, which consists of continuous broadband noises believed to be produced by radiation from charged particles.

In the case of whistlers, the energy released in the lower atmosphere by the sudden discharge must penetrate the atmosphere-ionosphere boundary. For the frequency range of interest in this work (100 to 3000 Hz), this boundary may be assumed to be sharp. For typical conditions of the lower ionosphere the decrease in phase velocity of the entering wave is of the order of 50:1. This decrease in phase velocity means, according to Snell's law, that for any angle of incidence below the boundary, the waves will emerge on the other side with their wave normals practically

perpendicular to the boundary. The details of this penetration mechanism can be rigorously treated only by the application of full wave methods (see Budden [1961] and Scarabucci [1969]). However, the full wave approach has confirmed in general the simple geometrical optics reasoning used above and, unless one is particularly interested in studying the amplitude of the waves across the transition, the geometrical optics approach is adequate. For the present purposes, it is also satisfactory to consider the atmosphere-ionosphere boundary fixed at approximately 100 km altitude. Until 1968, the only particular whistler traces whose characteristic dispersion could be attributed to specific ion effects were the proton and the helium whistlers (see Gurnett et al. [1965] and Barrington et al. [1966]). Since then, additional "ion whistlers" have been identified and interpreted by the author and their study is included in the present work.

ELF and VLF hiss or continuous noises have been reported extensively in the magnetosphere, mainly from analysis of satellite data. The range of latitudes and frequencies is quite broad, from low latitudes to the polar region and from a few hundred Hz to dozens of kHz. In particular, the so-called auroral hiss, in the range of $\sim$ 5 kHz to dozens of kHz and confined to the auroral zone has been treated extensively in the literature (see Jørgensen [1968]; Laaspere et al. [1971] and references in those papers) and is not the object of the present study. The kind of hiss of interest here (ELF hiss extending from a few hundred Hz to approximately 3 kHz) has been reported and discussed also extensively (see discussion in Chapter 4), but most investigators have confined their attention to invariant latitudes greater than 35^{o} and/or high altitudes. In the low to medium latitudes and altitudes of

the order of 1000 km, the only particular feature of the ELF hiss established by previous investigators is the low frequency cutoff (see Gurnett and Burns [1968]).

C. CONTRIBUTIONS OF THE PRESENT WORK

The contributions of the present work can be stated briefly as follows:

1. Expressions for the rate of variation of the wave normal direction along the ray path are developed and applied, including the effects of ions. This is an extension of previous work by Cerisier [1967] in which the effect of ions are not included.
2. Certain new types of whistlers are identified and explained, including the transequatorial or 1^- proton whistler, the ion cutoff whistler and hybrid forms of both.
3. New characteristics of an ELF hiss band (here called band limited ELF hiss or simply BLH) are found. Their interpretation has led the author to suggest a model with the source located on the geomagnetic equator near $L = 4$. This new model provides alternative explanations of some previously reported properties of ELF hiss.

D. PLAN OF THE WORK

In Chapter 2, some introductory material is presented on the propagation of waves in anisotropic media, followed by the development and application of expressions for the rate of variation of the wave normal orientation along the ray paths.

In Chapter 3, the 1^- proton whistler, the ion cutoff whistler and hybrid forms of both phenomena are presented and interpreted using ray tracing techniques and concepts from Chapter 2.

Chapter 4 deals with the observations and characteristics of ELF hiss and an interpretation also based on propagation properties. A range of wave normals at the source and a region of generation are then deduced and some comments are made about generation mechanisms based on

radiation from energetic electrons.

Finally in Chapter 5 some conclusions are drawn and recommendations are made for future work. There are also four appendices where derivations and auxiliary material are presented.

II. EFFECTS OF THE MEDIUM ON THE PROPAGATION OF ELF WAVES

A. INTRODUCTION

In the following analysis the medium is supposed to be a cold, collisionless, electrically neutral plasma composed of electrons plus three singly-charged positive ion species: oxygen, helium and hydrogen. Furthermore, this plasma is immersed in a static dipole type magnetic field. For the low frequency end of the spectrum, the refractive index μ at a fixed point in such a medium varies, as a function of frequency, as shown if Fig. 1 (for details see Stix [1962]; Smith and Brice [1964]; Gurnett et al. [1965]). The branches labeled R and L represent the values of μ^2 corresponding to a wave normal direction along the static magnetic field, the R and L standing, respectively, for the right-hand and left-hand circularly polarized modes. The branches labeled e (for extraordinary) represent the values of μ^2 for a wave normal direction perpendicular to the static magnetic field, with linear polarization (static and wave magnetic fields parallel). For intermediate wave normal directions μ^2 lies inside the shaded regions. Using Stix's nomenclature and MKS units we can write:

$$R = 1 - \sum_j R_j , \qquad R_j = \frac{X_j}{1 + s_j Y_j}$$

$$L = 1 - \sum_j L_j , \qquad L_j = \frac{X_j}{1 - s_j Y_j}$$

$$P = 1 - \sum_j X_j$$

$$X_j = \frac{\omega_{pj}^2}{\omega^2} \qquad \text{where} \qquad \omega_{pj}^2 = \frac{N_j e^2}{\epsilon_o m_j} \quad \text{(plasma frequency)}$$

$$Y_j = \frac{|e| B}{m_j \omega}$$

where

j corresponds to the electron and ion species

e is the elementary charge

s_j is the charge sign of the j^{th} species particle

m_j is the mass of the j^{th} species particle

ω is the angular wave frequency

ω_{pj} is the angular plasma frequency of the j^{th} species particles

B is the static magnetic field intensity

ε_o is the permitivity of vacuum

The two values of μ corresponding to the two propagation modes are the real solutions of the following equation:

$$\sin^2\psi\left(\frac{1}{1-R/\mu^2}+\frac{1}{1-L/\mu^2}-2\right)+2\cos^2\psi\left(\frac{1}{1-P/\mu^2}-1\right)=0 \qquad (2.1)$$

where ψ is the angle between the static magnetic field and the wave normal. From now on the angle ψ will be simply called "wave normal angle."

In Fig. 1 the frequencies labeled f_1 to f_8 are characteristic frequencies and correspond to the various resonances (where $\mu \to \infty$) and cutoffs (where $\mu \to 0$). Frequencies f_1, f_4 and f_7 are, respectively, the gyrofrequencies of the oxygen, helium and hydrogen ions. Frequencies f_2 and f_5 are called two-ion resonances and f_8 is normally called the lower hybrid resonance frequency (LHR). Similarly, frequencies f_3 and f_6 are called two-ion cutoffs. Frequencies f_{x1} and f_{x2} are the crossover frequencies, where the polarization of the R and L modes become linear (static and wave magnetic fields perpendicular) and interchange signs. The ion gyrofrequencies depend only on the e/m ratios of each particle species and the intensity of the static magnetic field.

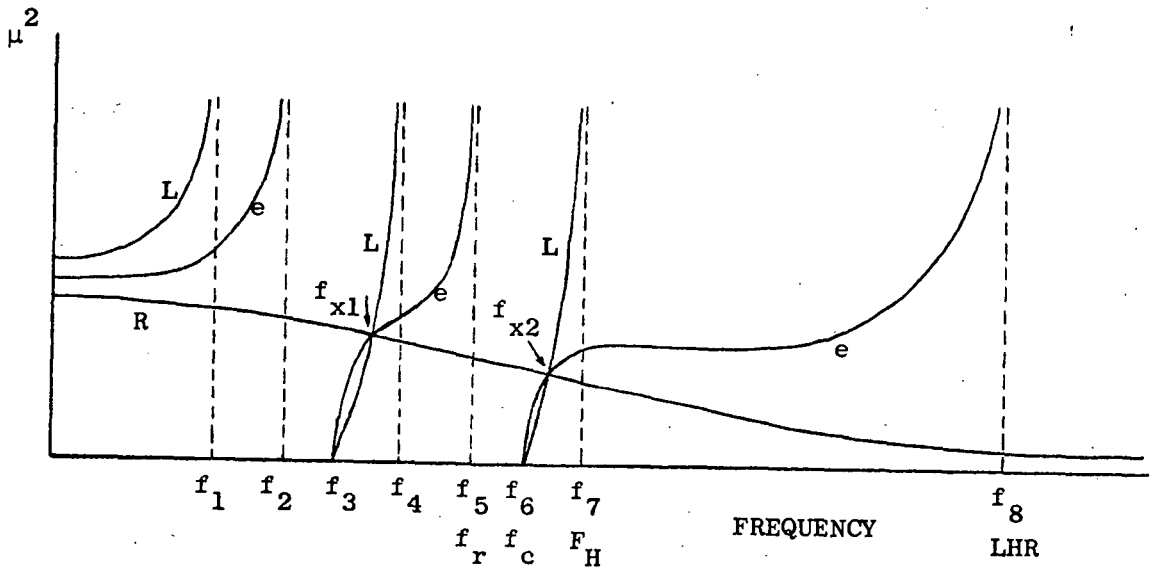

FIGURE 1. CURVES OF μ^2 AS A FUNCTION OF FREQUENCY IN A MEDIUM COMPOSED OF ELECTRONS AND THREE ION SPECIES (OXYGEN, HELIUM AND HYDROGEN). The several characteristic frequencies caused by the presence of these ions are indicated (f_1 to f_8).

For the models considered here their ratio is always 1:4:16. At a fixed point in space, frequencies f_1, f_4 and f_7 are constant and the others vary with the relative ion composition. It should be noted, however, that frequencies f_2 and f_3 are always situated between the ion gyrofrequencies f_1 and f_4, while f_5 and f_6 are always situated between f_4 and f_7. Figures 2a-g illustrate what happens with the two ion resonances and cutoffs when the relative ion concentrations are varied.

Due to the fact that the static magnetic field (and thus all the gyrofrequencies) vary with the inverse cube of geocentric distance, an observer moving up or down inside this medium will see the group of frequencies f_1 to f_8, respectively, decrease or increase monotonically.

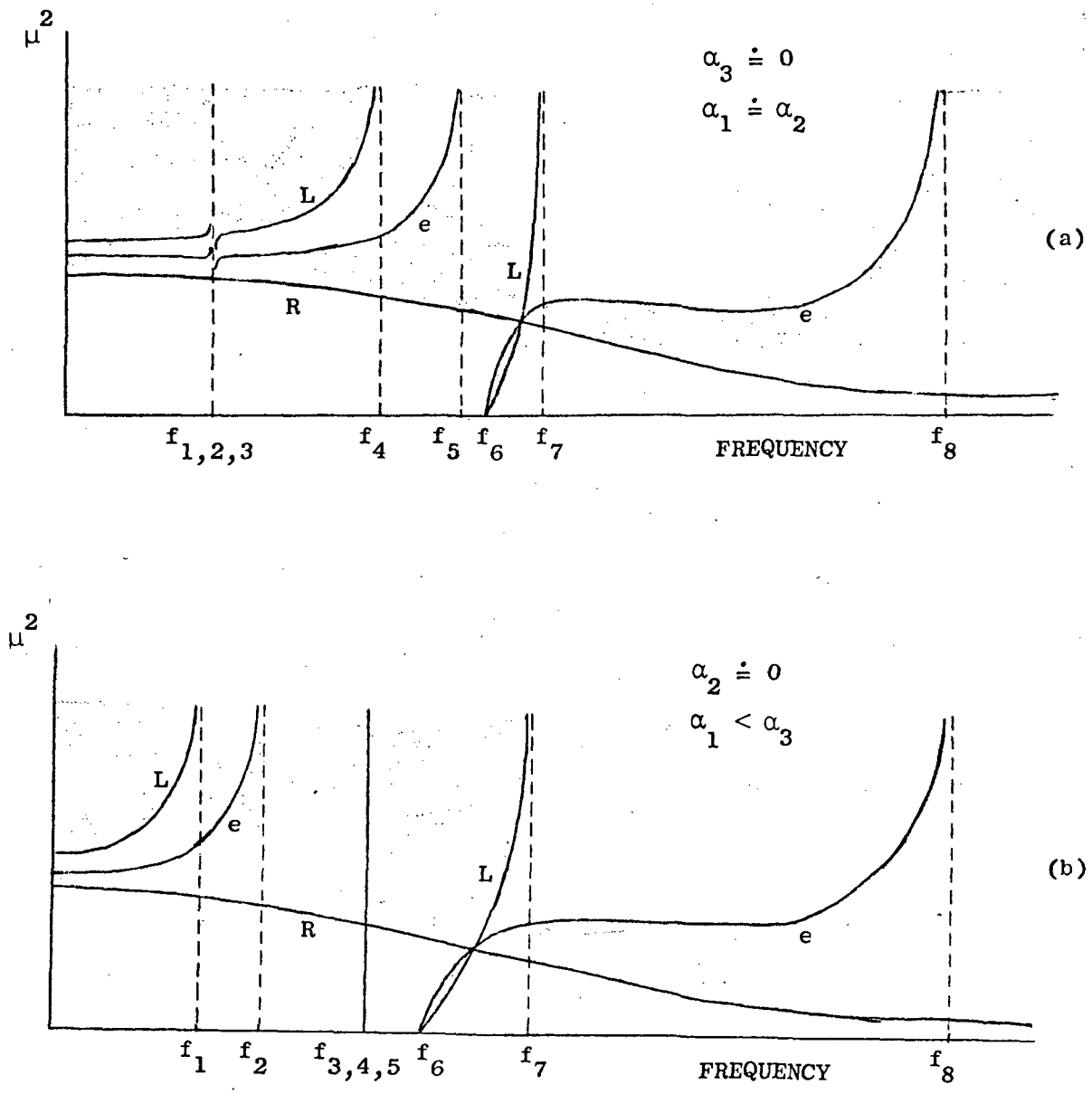

FIGURE 2a,b. CURVES OF μ^2 AS A FUNCTION OF FREQUENCY FOR TWO DIFFERENT IONIC COMPOSITIONS. The several characteristic frequencies are indicated (f_1 to f_8). In (a) the oxygen relative concentration is negligible when compared with the other two ions. In (b) the helium relative concentration is negligible and the hydrogen relative concentration is smaller than that of oxygen.

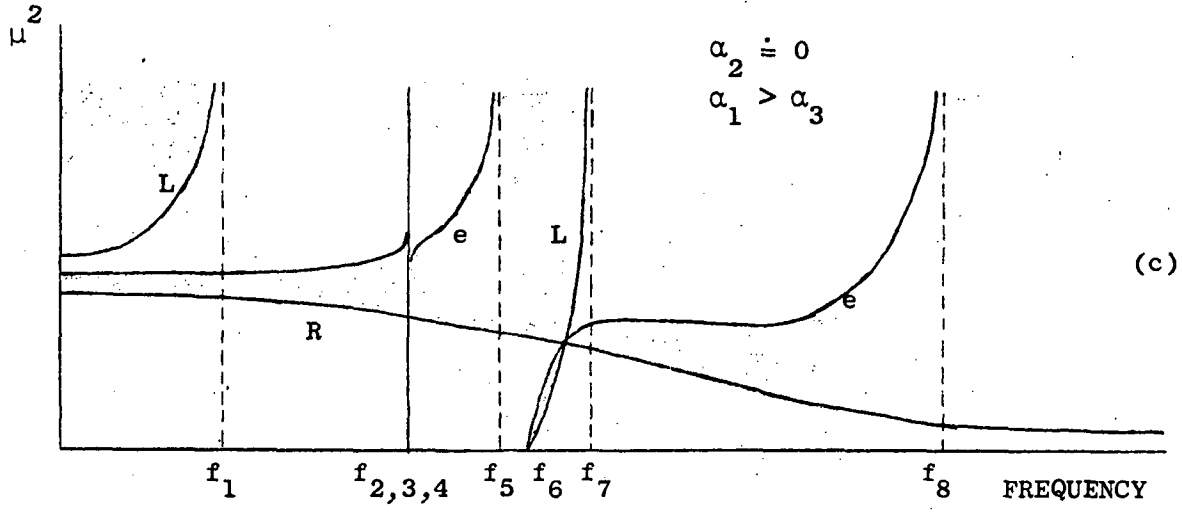

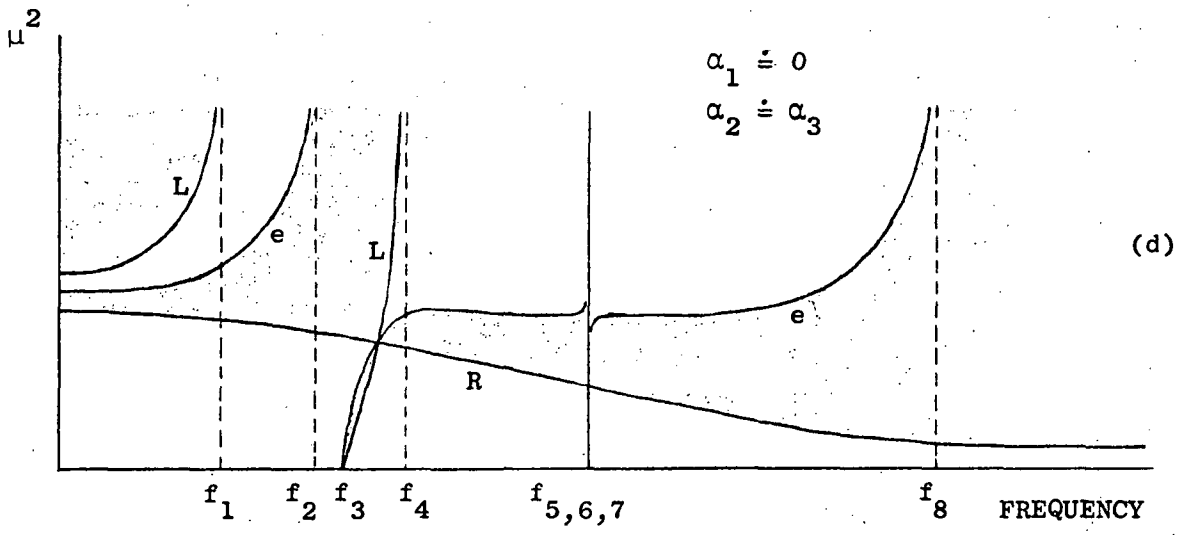

FIGURE 2c,d. IN (c) THE HELIUM RELATIVE CONCENTRATION IS NEGLIGIBLE AND THE HYDROGEN RELATIVE CONCENTRATION IS LARGER THAN THAT OF OXYGEN. In (d) the hydrogen relative concentration is negligible.

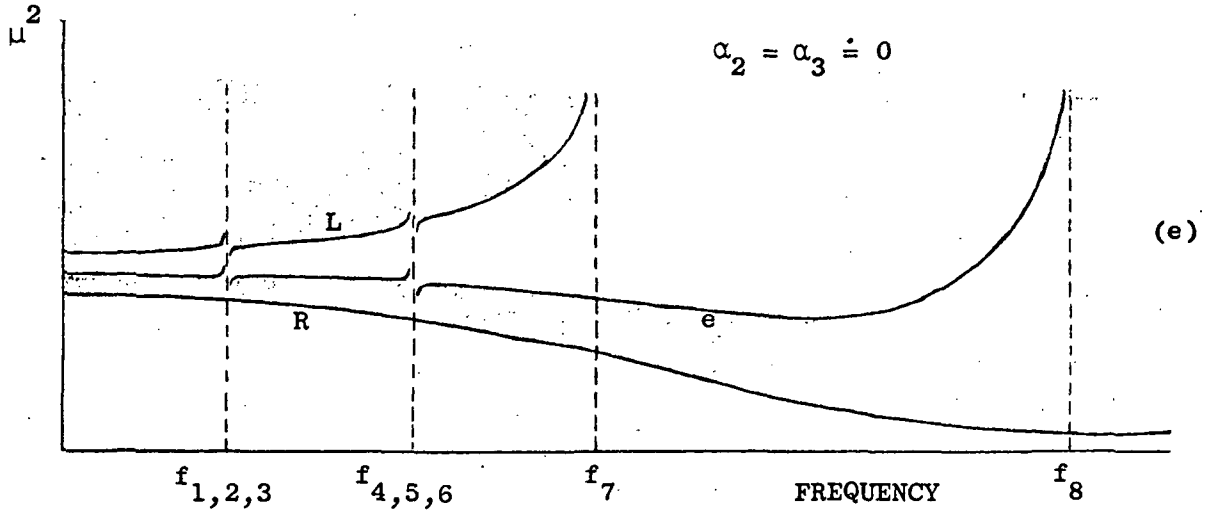

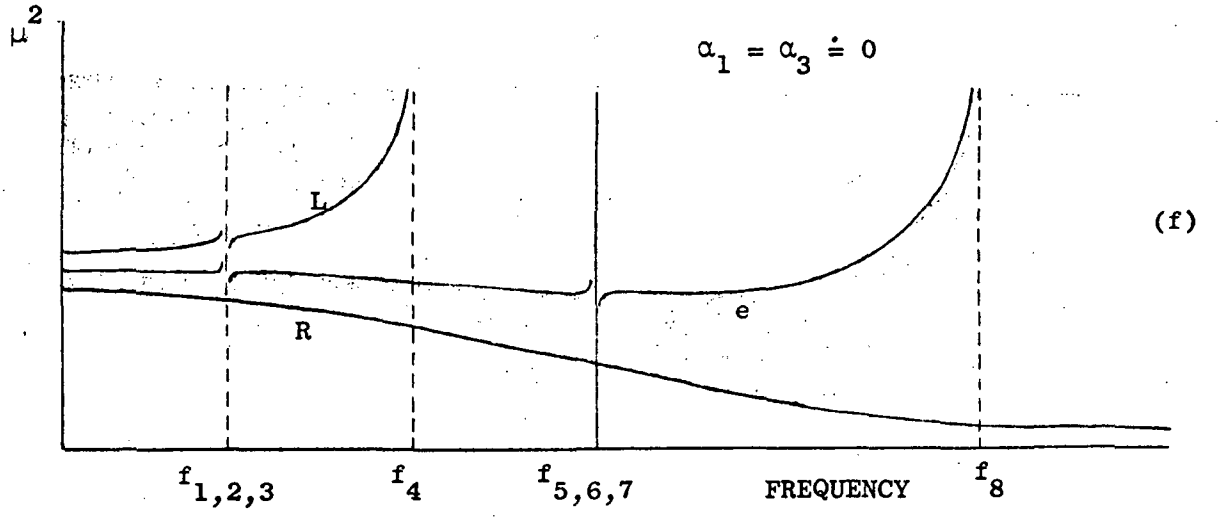

FIGURE 2e,f. IN THESE EXAMPLES ONLY ONE OF THE ION SPECIES IS OF IMPORTANCE. In (e) the helium and oxygen relative concentrations are negligible. In (f) the hydrogen and oxygen are negligible.

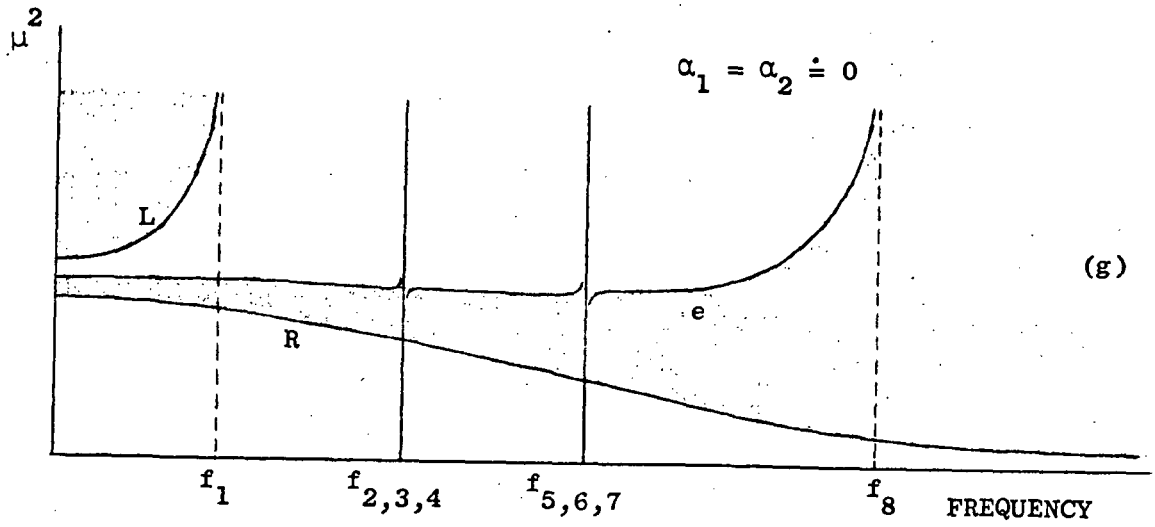

FIGURE 2g. HERE THE ONLY ION OF IMPORTANCE IS THAT OF OXYGEN; THE HYDROGEN AND HELIUM RELATIVE CONCENTRATIONS ARE NEGLIGIBLE.

This means that the topology of the curves of μ^2 versus frequency for a fixed point in the magnetosphere is similar to the topology of curves of μ^2 versus altitude for a constant frequency. Now, there will be characteristic levels in analogy with the former characteristic frequencies. Consequently, a point moving along the positive frequency axis in Figs. 1 or 2 may also be interpreted as a constant frequency wave moving upwards.

At each point inside the magnetosphere one can define a vector with length equal to μ and same direction as the wave normal. The tips of all possible refractive index vectors describe a surface that is called the refractive index surface. As the medium is uniaxial, the refractive index surfaces are figures of revolution around the static magnetic field direction. Figure 3 shows the intersection of a typical

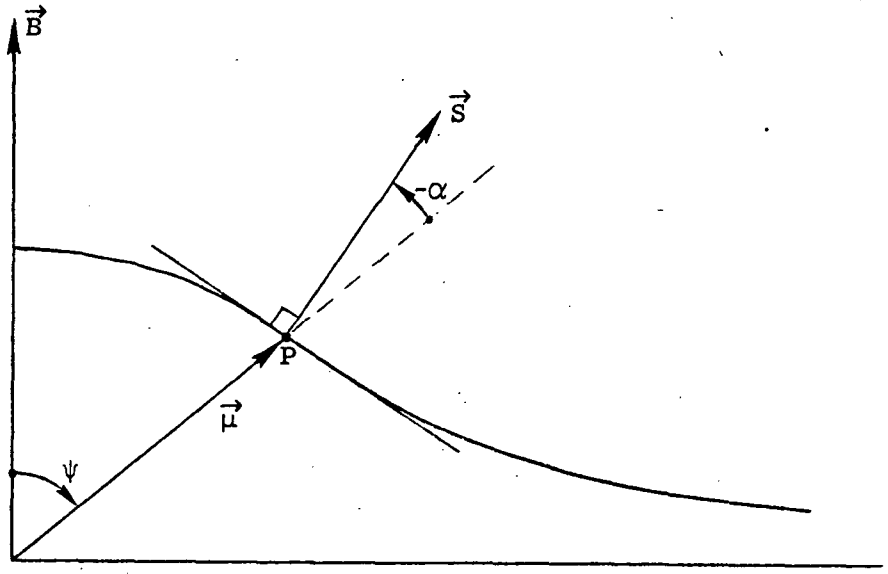

FIGURE 3. THE RAY DIRECTION ($\vec{S}$) IS ALWAYS PERPENDICULAR TO THE REFRACTIVE INDEX SURFACE.

refractive index surface with a plane containing $\vec{B}$. It can be shown (see Stix [1964]) that the direction of energy flow or ray direction $\vec{S}$ is normal to the refractive index surface at the point P where the vector $\vec{\mu}$ meets that surface. It can be also shown that:

$$\tan \alpha = - \frac{1}{\mu} \frac{\partial \mu}{\partial \psi} \qquad (2.2)$$

where α is the angle from the wave normal direction to the ray direction. Therefore, at each point, the three vectors $\vec{S}$, $\vec{\mu}$ and $\vec{B}$ are contained in the same plane. Furthermore, as $\partial\mu/\partial\psi$ is positive for $0 \leq \psi \leq \pi/2$, the ray direction lies between the magnetic field and the wave normal directions.

Finally, one may observe that each two-ion resonance divides the neighboring (μ,f) space and its analogue, the (μ,h) space, in two regions where the refractive index surfaces have different topologies. The region

immediately below f_2 or f_5 is characterized by closed refractive index surfaces, while the region immediately above f_2 or f_6 is characterized by open refractive index surfaces. For large wave normal angles then, waves propagating in the two regions will have very different ray directions (see Fig. 4). Therefore, it can be expected that a wave starting its path at the base of the ionosphere between, for example, frequencies f_4 and f_5 (see Fig. 1) and propagating upwards, will experience a noticeable change in ray path when it crosses the resonance level. This effect will be shown in Chapter 3 with the aid of ray tracings.

B. FACTORS AFFECTING THE ORIENTATION OF THE WAVE NORMALS

The propagation of ELF waves throughout the magnetosphere is affected by the presence of positive ions mainly through the cutoffs and resonances that they introduce in the dispersion relation. In order to understand the effects of the electron and ion densities and also of the earth's magnetic field on the orientation of the wave normals along the ray paths, the following expression, derived by Cerisier [1967] from the Haselgrove [1954] ray tracing equations will be used:

$$\frac{d\psi}{ds} = \cos\alpha \left[\sum_j \frac{1}{\mu} \frac{\partial \mu}{\partial N_j} \nabla N_j \cdot \hat{k}_\perp + \frac{1}{\mu} \frac{\partial \mu}{\partial B} \nabla B \cdot \hat{k}_\perp - \nabla \beta \cdot \hat{k} \right] \qquad (2.3)$$

where

- ds represents an element of ray path
- N_j represents the electron and ion number densities
- B is the magnitude of the static magnetic field
- β is the inclination of the magnetic field relative to the dipole axis (see Fig. 5)
- $\hat{k}$ is a unit vector along the wave normal direction
- $\hat{k}_\perp$ is a unit vector perpendicular to the wave normal direction, oriented along $\psi + \pi/2$ (see Fig. 5).

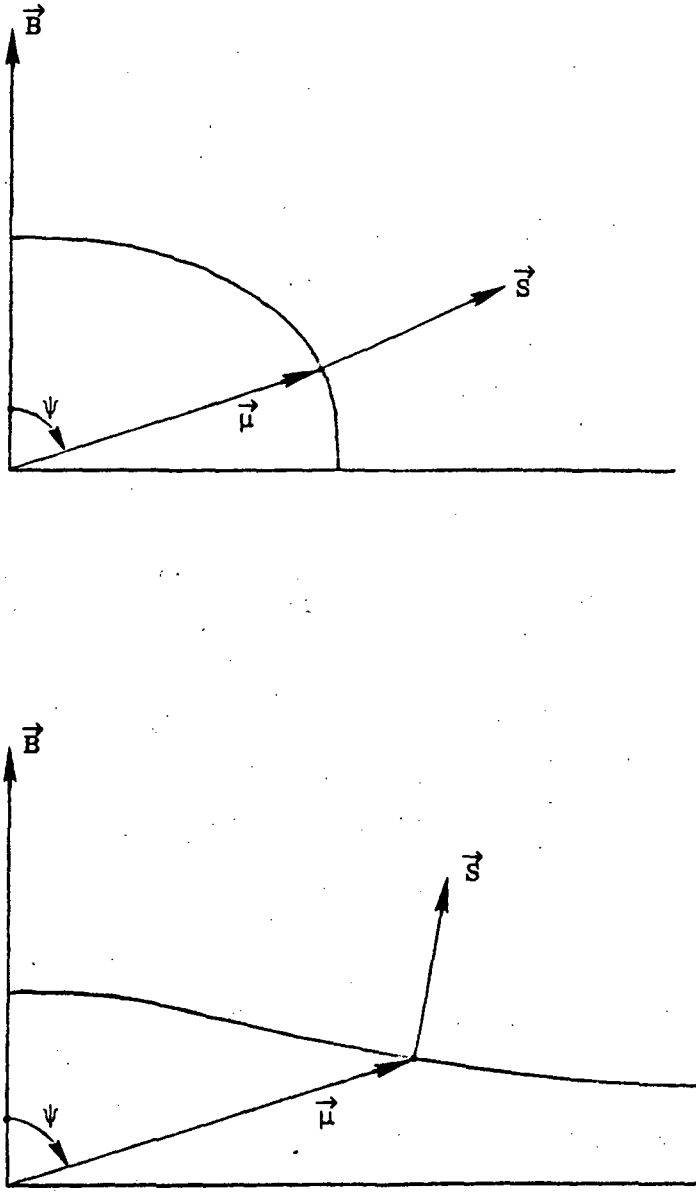

FIGURE 4. SHAPE OF THE REFRACTIVE INDEX SURFACE BELOW (a) AND ABOVE (b) THE TWO ION RESONANCE FREQUENCY f_r.

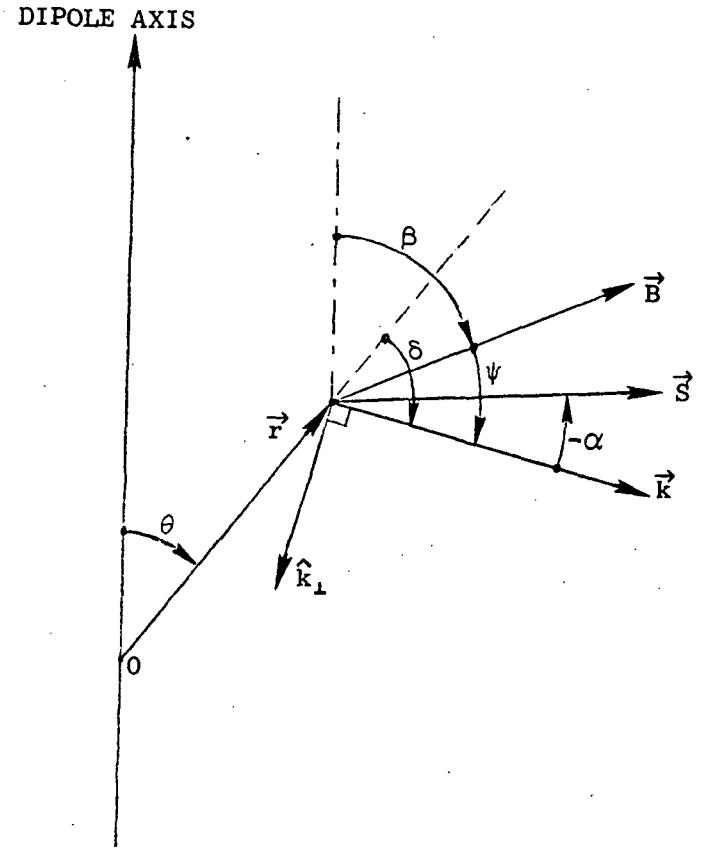

FIGURE 5. POLAR COORDINATE SYSTEM. All angles are measured clockwise from the references shown.

The three terms inside the brackets are the contributions of the electron and ion densities, the magnitude of the dipole magnetic field and the inclination of this magnetic field. Equation (2.3) is derived in Appendix A.

To apply Eq. (2.3) Cerisier used an approximate expression for the refractive index, neglecting the influence of the ions. In the following analysis the complete expression for μ will be used. The derivation of the equations that follow can be found in Appendix A.

The first term inside the brackets in Eq. (2.3), which corresponds

to the contribution of the electrons and ions can be written as:

$$\sum_j \frac{1}{\mu} \frac{\partial \mu}{\partial N_j} \nabla N_j \cdot \hat{k}_\perp = - \sum_j \left[\frac{1}{\mu} \frac{\partial \mu}{\partial R} R_j + \frac{1}{\mu} \frac{\partial \mu}{\partial L} L_j + \frac{1}{\mu} \frac{\partial \mu}{\partial P} X_j \right] \frac{\nabla N_j}{N_j} \cdot \hat{k}_\perp \qquad (2.4)$$

where

$$\frac{\nabla N_j}{N_j} \cdot \hat{k}_\perp = - \frac{1}{N_j} \left[\frac{\partial N_j}{\partial r} \sin \delta - \frac{1}{r} \frac{\partial N_j}{\partial \theta} \cos \delta \right] \qquad (2.5)$$

δ is the angle between the local vertical and the wave normal direction and (r,θ) are the polar coordinates of a point in the magnetic meridian plane (see Fig. 5).

Similarly, the second term in Eq. (2.3), which corresponds to the contribution of the magnitude of the static magnetic field (dipole), can be written:

$$\frac{1}{\mu} \frac{\partial \mu}{\partial B} \nabla B \cdot \hat{k}_\perp = \sum_j \frac{s_j Y_j}{X_j} \frac{1}{\mu} \left[\frac{\partial \mu}{\partial R} R_j^2 - \frac{\partial \mu}{\partial L} L_j^2 \right] \frac{\nabla B}{B} \cdot \hat{k}_\perp$$

where

$$\frac{\nabla B}{B} \cdot \hat{k}_\perp = \frac{3}{r} \left[\sin \delta - \cos \delta \frac{\sin \theta \cos \theta}{1 + 3\cos^2 \theta} \right]$$

Finally, the third term, for the contribution of the inclination of the magnetic field is:

$$\nabla \beta \cdot \hat{k} = \frac{3}{r} \sin \delta \frac{1 + \cos^2 \theta}{1 + 3\cos^2 \theta}$$

The effectiveness of each of the three terms in Eq. (2.3) in determining the change in direction of the wave normals depends on the angle α between the ray and the wave normal. When α is zero, the effect is maximum and when α is $\pi/2$ the effect is zero. When $\alpha \leq \pi/2$, $\cos \alpha$ is positive and the resulting sign of $d\psi/ds$ must come from the terms inside the brackets. If the wave normal angle ψ is measured from the

direction of $\vec{B}$ with the provision that $|\psi| \leq \pi/2$, the sign will be positive (negative) when the wave normal $\vec{k}$ turns towards the inside (outside) of the field line. Because of the scalar products $\nabla N_j \cdot \hat{k}_\perp$ appearing in the first term of Eq. (2.3), each of its four components will change signs whenever the wave normal crosses the direction of the respective gradient. The same is true of the second term when the wave normal crosses the direction of ∇B. As for the third term, expressed by $\nabla\beta \cdot \hat{k}$, the change in sign occurs around the vertical direction, because $\nabla\beta$ is always horizontal for a dipole field.

C. EVALUATION OF THE COMPONENTS OF $d\psi/ds$ IN A MODEL MAGNETOSPHERE

In this section, the three components of $d\psi/ds$ are evaluated in a model magnetosphere for a given ELF wave. The computation is made as a function of altitude, maintaining a constant wave normal direction in order to compare the magnitudes of the three terms in several regions of the (μ,r) space around the characteristic levels of the hydrogen ion (where the wave frequency is equal to one of the characteristic frequencies). The density model used here is composed of electrons and three ion species (hydrogen, helium and oxygen). The electrons and ions are assumed to be in diffusive equilibrium along magnetic field lines in the manner described by Angerami and Thomas [1964]. The temperature is the same for all particles and the parameters of the model are adjusted to obtain a reasonably good fit with an electron density profile from Alouette II in the fall of 1967. It should be stressed at this point that no claims whatsoever are made here about how representative of actual conditions those parameters are. The D.E. model is chosen mainly because it is well behaved mathematically. Details of the model and derivation of expressions

for $\frac{\partial N_j}{\partial r}$ and $\frac{\partial N_j}{\partial \theta}$ appearing in Eq. (2.5) can be found in Appendix B.

Figure 6 shows the electron density profile of the model between 450 and 2000 km of altitude. The dots represent values of density measured by Alouette II in August 5, 1967 at approximately 2000 LT. The parameters of the D.E. equations are also shown in the figure and reference to Appendix B should be made for the meaning. The range of altitudes of 450 to 2000 km covers the regions where most of the so-called ion whistlers have been detected.

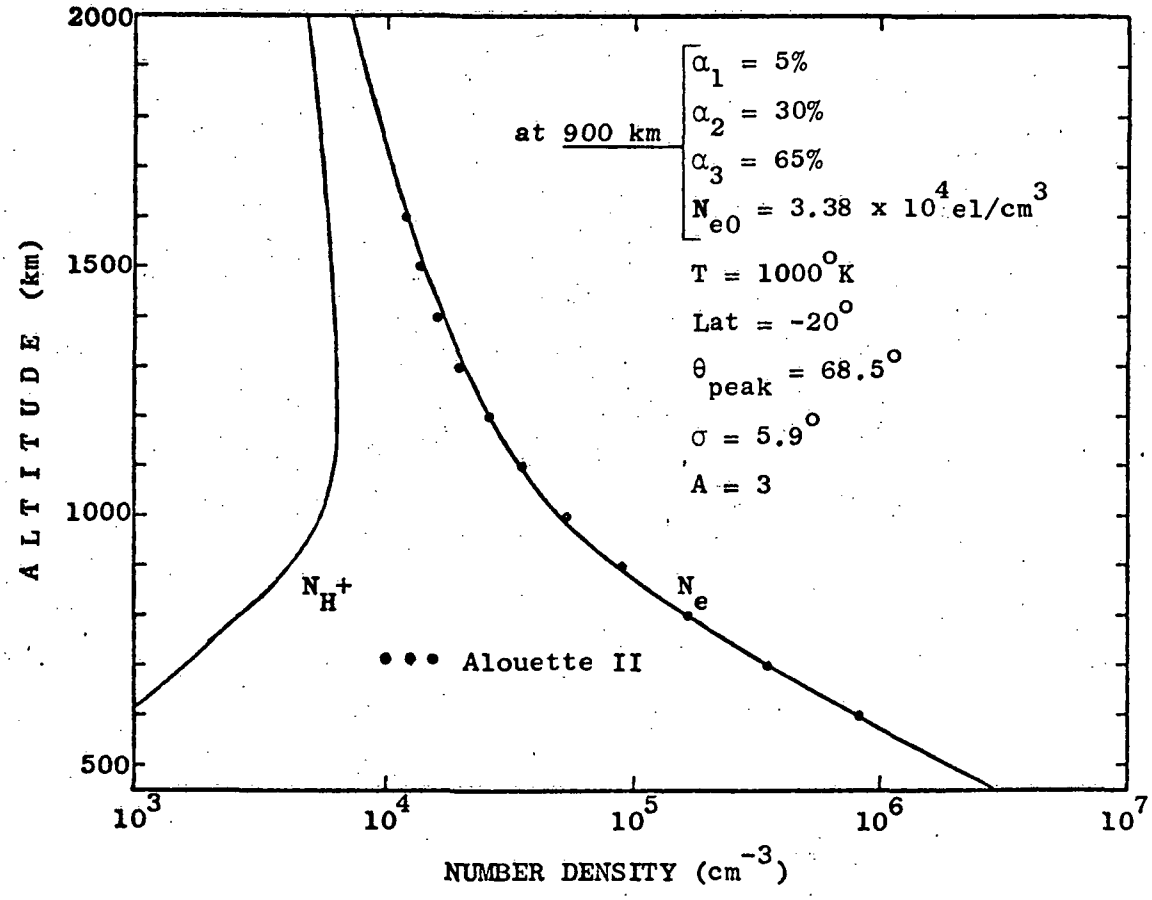

FIGURE 6. ELECTRON AND H^+ DENSITY PROFILES FOR THE DAYTIME IONOSPHERE MODEL USED THROUGHOUT THE PRESENT WORK. The parameters indicated are defined in Appendix B.

The dispersion relation admits two solutions, or modes, that may or may not correspond to propagating waves in the medium. Whenever the two modes can propagate simultaneously, the terminology "slow" and "fast" can be applied unambiguously in correspondence with the respective values of phase velocity or refractive index. However, when one of the modes is evanescent, the same terminology will be extended here as shown in Fig. 7 around the hydrogen characteristic frequencies. In this context, a typical representative of the slow mode is the proton whistler and a typical representative of the fast mode is the ion-cutoff whistler to be studied in the next chapter.

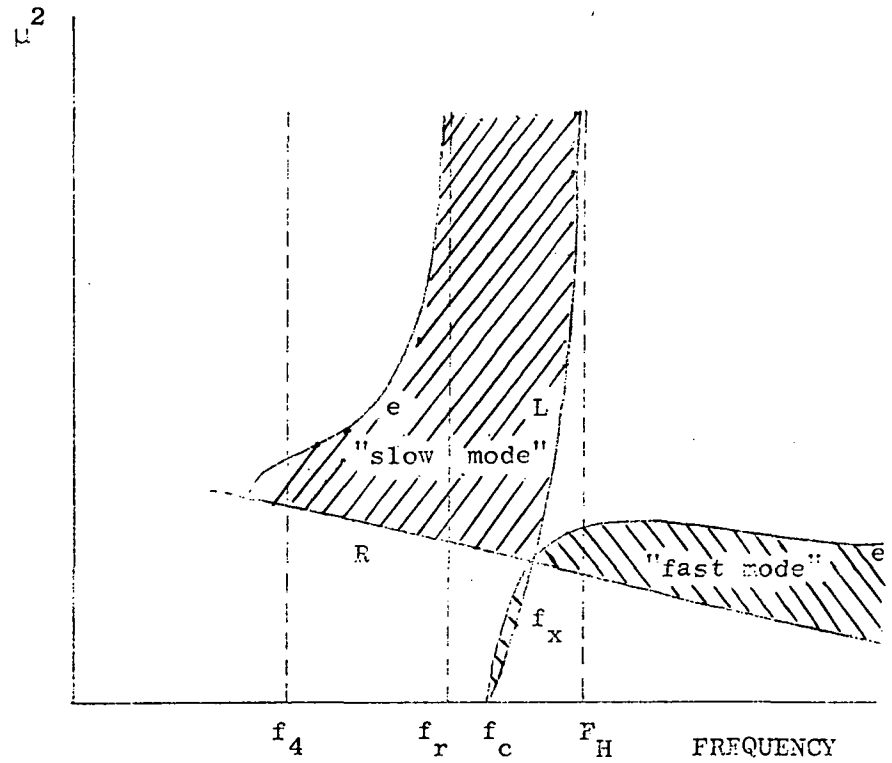

FIGURE 7. TERMINOLOGY USED FOR THE TWO PROPAGATING MODES IN THIS WORK.

Figures 8 to 11 show curves of the three components of $d\psi/ds$ between 450 and 2000 km and a latitude of 20^{o}, for a wave frequency of 300 Hz and a constant wave normal angle of -10^{o}. Because a logarithmic scale is used, the magnitude only of each term is plotted and the signs are indicated along the curves. Figures 8 and 9 correspond to the slow mode and extend up to 1150 km altitude, very close to the resonance level where $\mu \rightarrow \infty$. Above this altitude the mode is evanescent. Above 450 km the particle density term is positive and is dominated by the electron density contribution. In the vicinity of the crossover altitude, the term

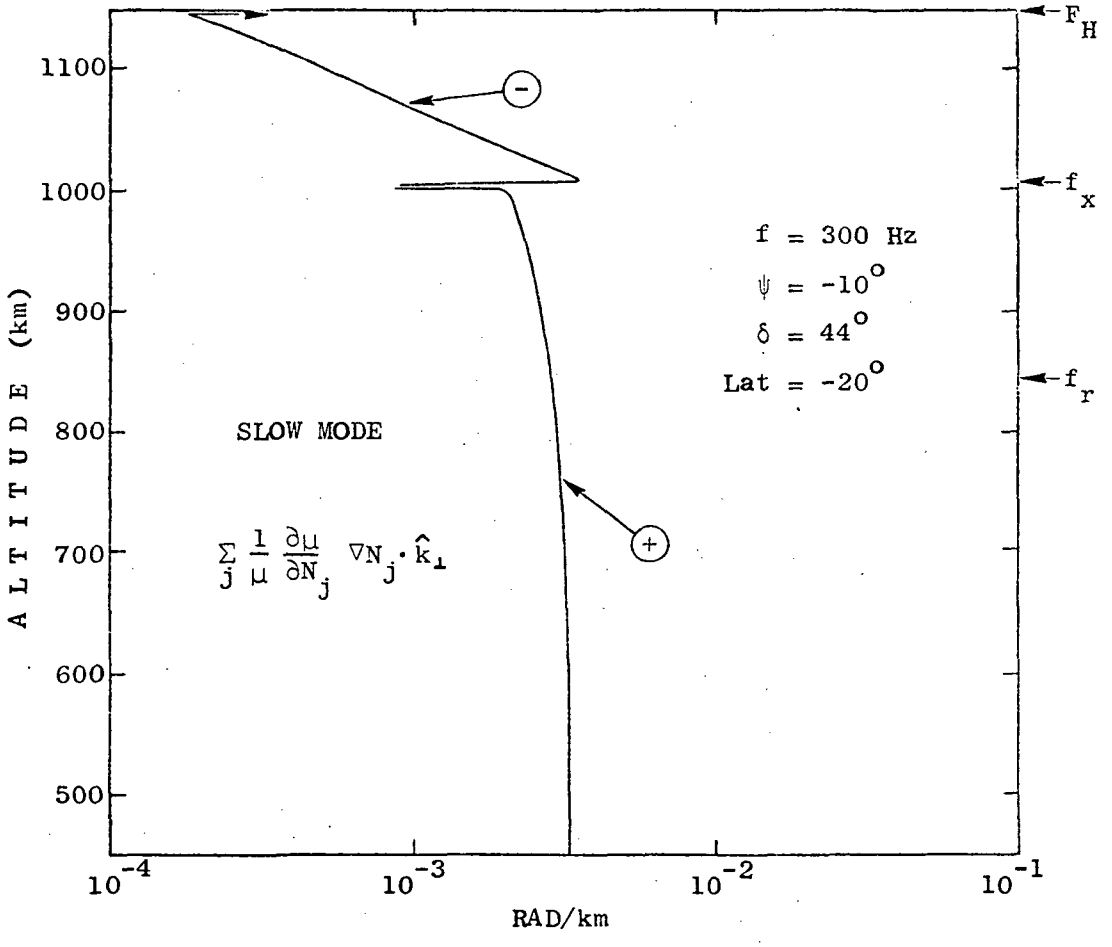

FIGURE 8. CURVES OF THE COMPONENT OF $d\psi/ds$ DUE TO THE ELECTRON AND ION DENSITIES (N_j), FOR A WAVE PROPAGATING IN THE SLOW MODE.

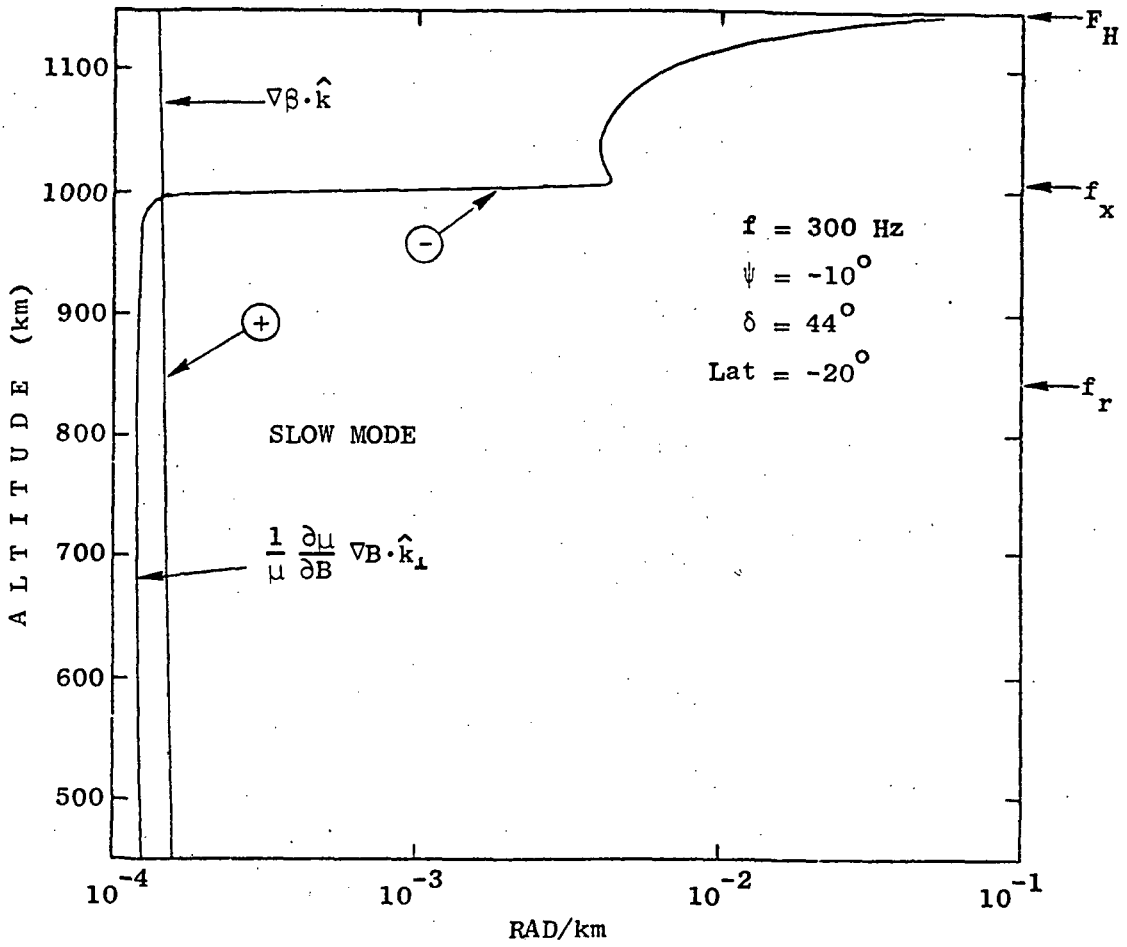

FIGURE 9. CURVES OF THE COMPONENTS OF $d\psi/ds$ DUE TO THE MAGNITUDE (B) AND INCLINATION (β) OF THE EARTH'S MAGNETIC FIELD, FOR A WAVE PROPAGATING IN THE SLOW MODE.

decreases very fast and changes sign. From this point upwards, the dominant contribution is that of the hydrogen ions. If the wave normal angle were zero, the resonance would occur exactly at the proton gyrofrequency altitude, which is independent of density variations. Therefore, if $\psi = 0$ the particle density term would remain finite up to and through the resonance altitude. However, if the wave normal angle is different from zero, it can be shown that $\frac{1}{\mu}\frac{\partial\mu}{\partial N_j} \Rightarrow \infty$ at resonance, which makes the particle density term also infinite. For small angles (such as in the examples) the magnitude of

$$\sum_j \frac{1}{\mu} \frac{\partial \mu}{\partial N_j} \nabla N_j \cdot \hat{k}_\perp$$

decreases with increasing altitude up to the immediate vicinity of the resonance and then grows very fast to infinity, as indicated in Fig. 8. The terms corresponding to the magnitude and inclination of the magnetic fields are illustrated in Fig. 9. The contribution of the magnitude of $\vec{B}$ is negligible in comparison with the particle density term up to the neighborhood of the crossover altitude and then becomes entirely dominant. However, unlike the particle density term, this one does not change sign anywhere and its magnitude always grows to infinity at resonance, independently of ψ. The term due to the inclination of $\vec{B}$ is independent of μ and decreases steadily as $1/r$.

Corresponding curves for the fast mode are shown in Figs. 10 and 11. The fast mode exists only above the two-ion cutoff altitude where the refractive index goes to zero, making the particle density term and also the term due to the magnitude of B tend to infinity. Between the cutoff altitude and approximately 1005 km both terms have the same order of magnitude and same sign. In this region, the particle density term is dominated by the contribution of the hydrogen ions. The term due to the magnitude of B continues to decrease until about 1020 km but without changing sign. Above that altitude the variations are much less pronounced and its magnitude is comparable to that of the third term ($\nabla\beta \cdot \hat{k}$). The particle density term is the most important between $\sim$ 1020 and 2000 km but decreases faster than the other two with increasing altitude. Therefore, one can expect this term to become negligible at larger altitudes.

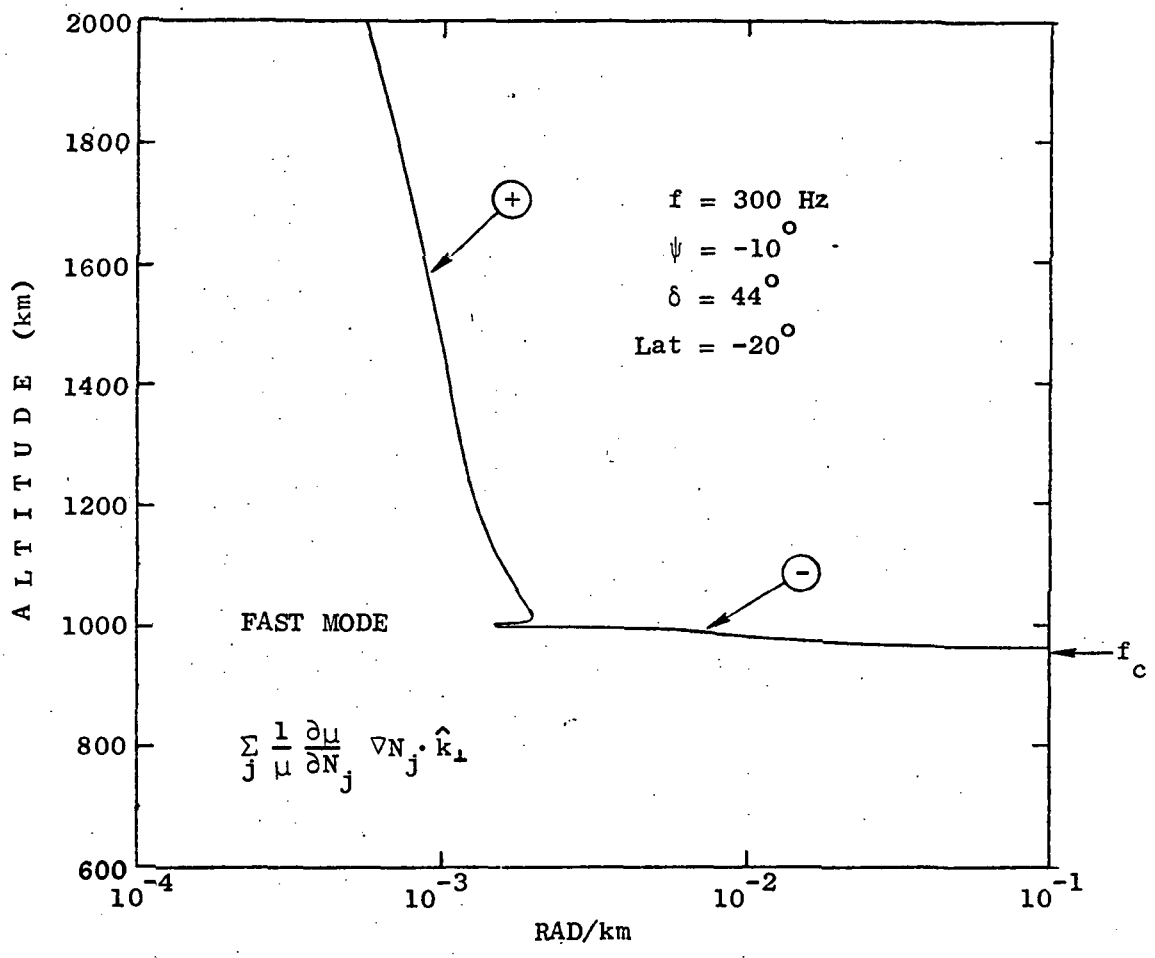

FIGURE 10. CURVES OF THE COMPONENT OF $d\psi/ds$ DUE TO THE ELECTRON AND ION DENSITIES (N_j), FOR A WAVE PROPAGATING IN THE FAST MODE.

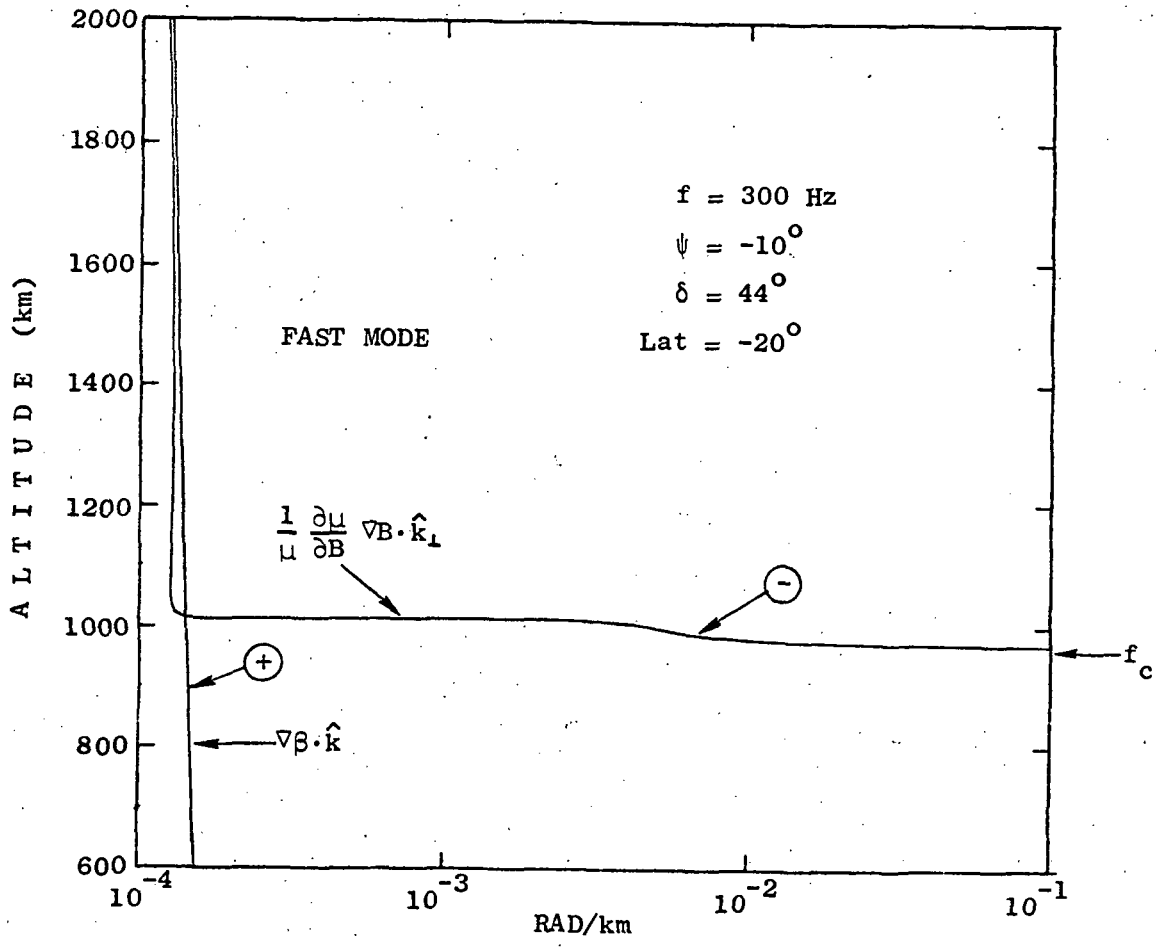

FIGURE 11. CURVES OF THE COMPONENTS $d\psi/ds$ DUE TO THE MAGNITUDE (B) AND INCLINATION (β) OF THE EARTH'S MAGNETIC FIELD, FOR A WAVE PROPAGATING IN THE FAST MODE.

III. ION WHISTLERS

A. INTRODUCTION

The natural whistler phenomena to be examined in this chapter may all be loosely called "ion-whistlers," meaning whistlers whose spectral shape is mainly a result of ion effects on the dispersion relation. These whistlers have been observed in data from the Stanford University VLF experiment flown on the OGO-4 satellite. This is a quasi-polar orbiting satellite ($\sim 86^{\circ}$ inclination) with perigee of $\sim$ 400 km and apogee of $\sim$ 900 km (orbital period $\sim$ 98 minutes). The signals are detected in a magnetic loop antenna which feeds a number of receivers serving different purposes. Of interest here are the two broadband receivers used for spectrographic analysis. The so-called ELF receiver covers the band of $\sim$ 15 to 300 Hz with a gradual rolloff between 300 and 1000 Hz. The VLF receiver covers the band of 300 Hz to 12.5 kHz. The signals are telemetered to ground and recorded in magnetic tape at the NASA telemetry stations and later they are processed at Stanford using a Rayspan real time spectrum analyzer (see Helliwell et al. [1961]). The final results are presented as frequency versus time spectra in strips of 35mm film with the time running alongside the film.

Following the conventional terminology used for whistlers detected in satellites (see Smith and Angerami [1968]), the events to be reported here will be called 0^{+} (zero plus), 1^{-} (one minus), 1^{+} (one plus), etc. according to the relative positions of the satellite and the source with regard to the magnetic equator and also according to the direction of propagation at the time of detection.

B. THE 1^- PROTON WHISTLER

This peculiar trace has been observed in some equatorial passes of OGO 4 [Muzzio, 1969] and a few examples are indicated by arrows in the spectrograms of Fig. 12. The two strips represent sections of the same pass detected at the Santiago telemetry station. The frequency range is 0 to 1.25 kHz and the time scale is indicated at the upper part of each strip. The traces are very similar to, and appear among regular or 0^+ proton whistlers from which they differ mainly by the lower value of their frequency of infinite delay time (f_∞). In addition, when the satellite moves away from the magnetic equator, the value of f_∞ for the events labeled 1^- decreases. The following analysis will show that the traces are proton whistlers propagating from the opposite hemisphere approximately along field lines. The name 1^- proton whistler is therefore appropriate. The decrease in f_∞ can be appreciated in the top panel of Fig. 13 until $\sim$ 0736, when the 1^- type traces disappear. Near 0735 some 0^+ proton whistlers from the southern hemisphere begin to be visible. Sections A and B of the top spectrogram are shown expanded in time at the middle and lower left, where individual events can be resolved. The approximate ray paths of events 1 (0^+) and 2 (1^-) are indicated in the sketch at right. In the 1^- type traces, frequencies above $\sim$ 150 Hz start their path at the base of the ionosphere already above the helium gyrofrequency level (frequency f_4 in Fig. 2e in Chapter 2). These waves are propagating in a region of closed refractive index surfaces. The ray direction is situated between the wave normal, which is initially vertical, and the direction of the static magnetic field. As the waves progress upward, they will approach the two-ion

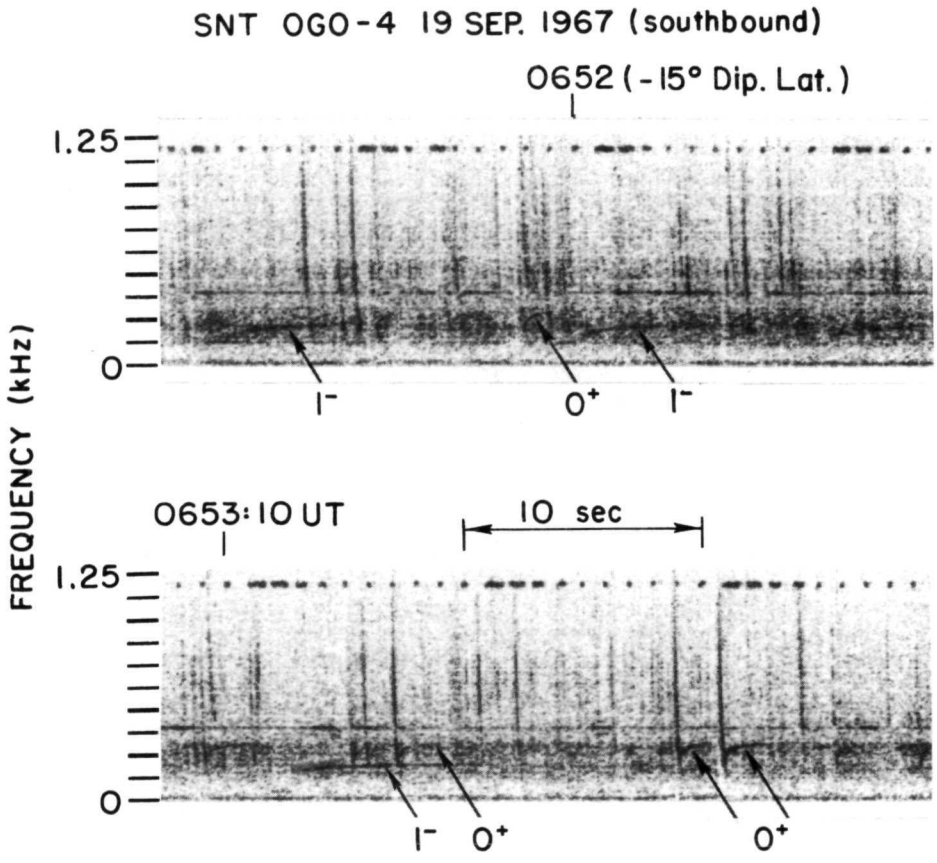

FIGURE 12. EXAMPLES OF 1^- PROTON WHISTLERS. Notice the difference in values of f_∞ between the 0^+ and 1^- events.

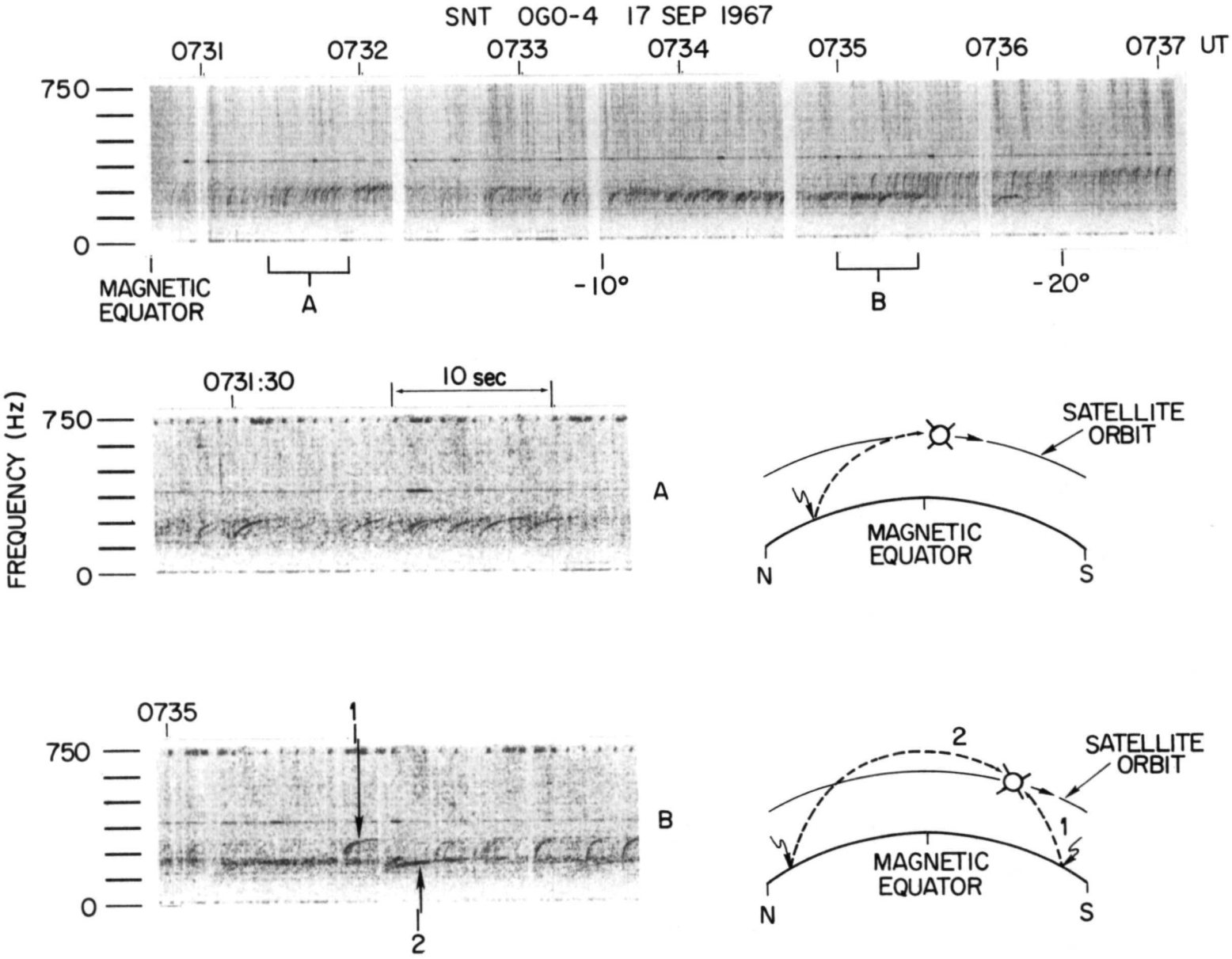

FIGURE 13. ILLUSTRATION OF THE DECREASE IN VALUE OF f_∞ OF THE 1^- PROTON WHISTLERS (LABELED 2 IN THIS FIGURE) WITH INCREASING LATITUDE. The approximate ray paths of the 0^+ (labeled 1) and 1^- events are indicated in the sketches.

resonance level (f_5), above which the refractive index surfaces open and the guiding effect of the static magnetic field becomes more and more important. To illustrate this change in ray path direction across the two-ion resonance level the ray tracing results of Fig. 14 are very useful. The frequency used is 200 Hz and the ray tracing starts at 100 km altitude and 19^o dipole latitude. The ionosphere model is the same as used in Chapter 2. The wave normal is initially vertical and the arrows along the ray path indicate subsequent orientations. The transition from closed to open refractive index surface is also indicated and the corresponding change in ray path direction can be noticed. When the ray crosses the equatorial plane the alignment with the field is already very good. The variations of wave normal angle along the ray path can be roughly compared with the values of $d\psi/ds$ for the slow mode plotted in Figs. 8 and 9. From the values of wave normal angle marked along the ray tracing of Fig. 14, one can observe the change in sign of $d\psi/ds$ close to the crossover level.

The upper frequency limit for a wave propagating in the slow mode, or similarly, the upper altitude limit for a fixed frequency, is given by the resonance condition:

$$\tan^2\psi = -\frac{P}{S} \tag{3.1}$$

where:

$$S = \frac{1}{2}(R + L) \tag{3.2}$$

When the wave normal angle ψ varies from 0^o to 90^o (see Stix [1962]) the resonance level decreases from the proton gyrofrequency to the two-ion resonance level. However, if $|\psi|$ is less than about 75^o the resonance remains close to the proton gyrofrequency level. Consequently,

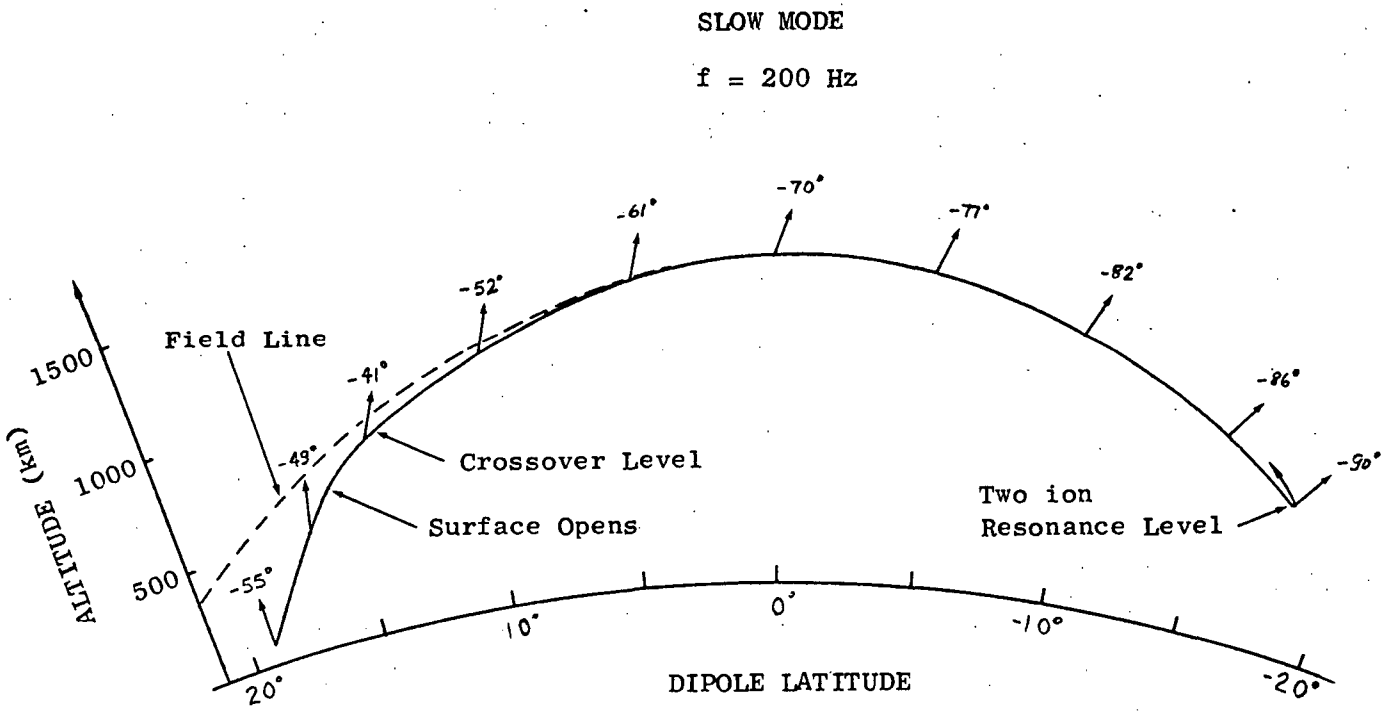

FIGURE 14. RAY PATH OF A 200 Hz WAVE IN THE SLOW MODE STARTING AT 100 KM ALTITUDE AND 19° DIPOLE LATITUDE. The wave normal is initially vertical. Subsequent wave normals and wave normal angles are indicated along the path.

for waves in the slow mode with ray paths similar to the one in Fig. 14, the upper frequency limit across the equatorial plane will be close to the minimum proton gryofrequency along the ray path, instead of the local value at the satellite. This will be the equatorial value of gyrofrequency along the field line passing through the satellite. Therefore, as the satellite moves away from the equator the minimum gyrofrequency along the ray path decreases, which is precisely the picture in Fig. 13. For each satellite altitude, there is a value of latitude beyond which it is impossible to detect 1^- proton whistlers. This limit can be understood from Fig. 15, which represents curves of proton gyrofrequency, crossover frequency and two-ion resonance frequency along a field aligned ray path containing the equatorial region. The characteristic frequencies of the other two ions have been omitted, for simplicity, but they could be used to explain the eventual occurrence of similar whistler traces at lower frequencies. The vertical lines marked ① and ② represent two satellite positions along the same field line and the corresponding spectral forms received at these two positions are illustrated in the two spectrogram sketches in the same figure. The minimum values of the characteristic frequencies occur at the equator, which is the highest point along the ray path. At higher latitudes the ray path is lower in the ionosphere. The corresponding decrease in hydrogen concentration makes the crossover and two-ion resonance frequencies approach the proton gyrofrequency, enhancing the probability of coupling between modes. This region of strong coupling is indicated in the figure. In the following analysis, waves in the slow mode are supposed to be propagating from left to right in the diagram and the effect of heavier ions will be disregarded. For simplicity, coupling near the crossover frequency will

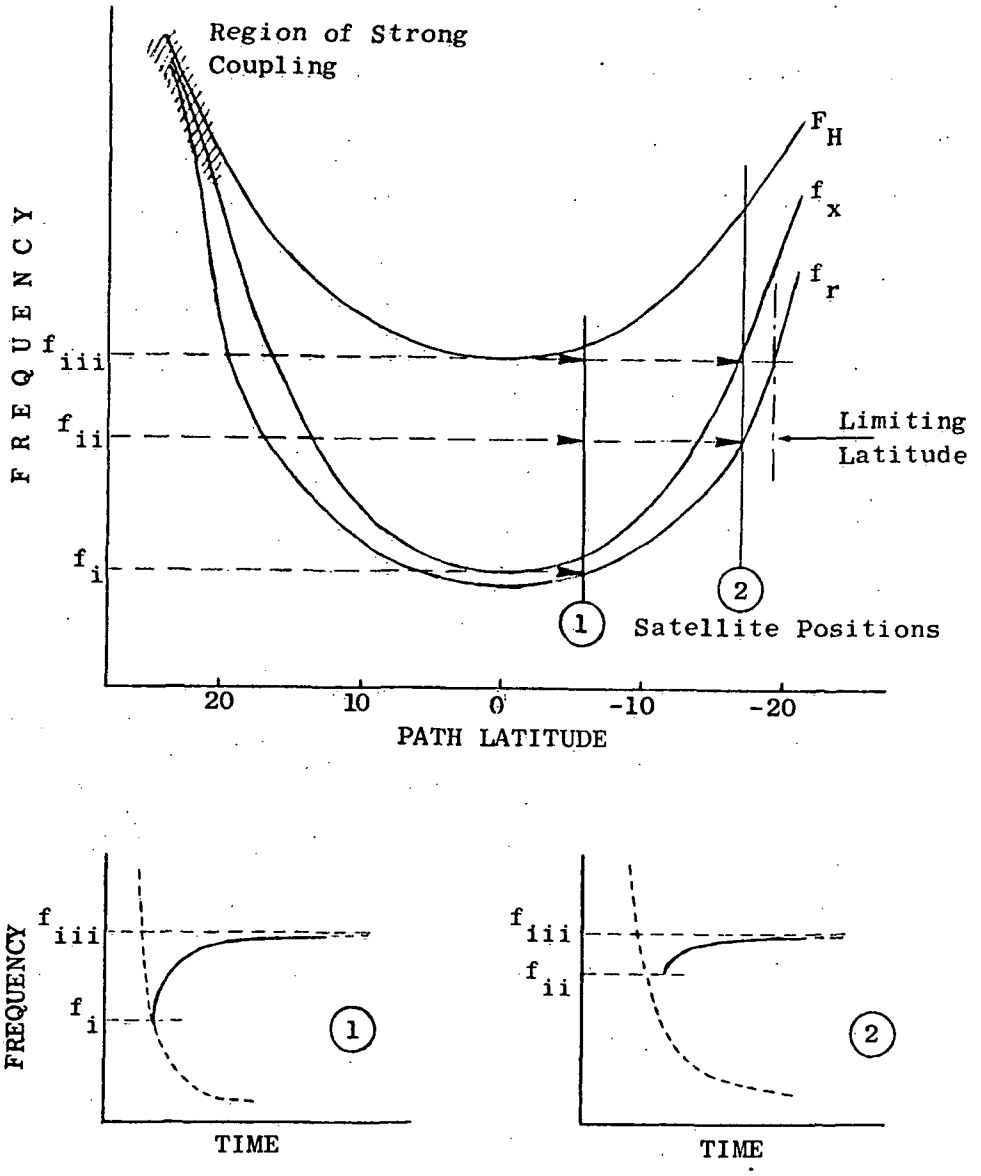

FIGURE 15. CURVES OF THE CHARACTERISTIC FREQUENCIES ALONG A FIELD-ALIGNED TRANSEQUATORIAL RAY PATH AND CORRESPONDING SPECTRA OF TWO 1⁻ PROTON WHISTLERS RECEIVED AT POSITIONS ① AND ② .

be disregarded also, except in the shaded regions where the characteristic frequencies are very near each other. With these restrictions, only frequencies below f_{iii} will be able to reach either one of satellite positions ① or ② in the slow mode. Depending on the satellite position however, there will be another limit on the low frequency side. To understand this limit, Figs. 14 and 15 have to be examined simultaneously. After crossing the equatorial plane the rays move downward and the wave normal angle approaches -90^{o}. In these circumstances, when the two-ion resonance level is attained the waves will be reflected back along a very near ray path. This mechanism is illustrated in Fig. 16 by the use of a "Poeverlein construction." On the other hand, the energy of the waves will probably be damped by lossless temperature effects across this resonance (see Stix [1962], Chapt. 3). For 1^{-} proton whistlers therefore, the minimum frequency observable will be either the minimum crossover frequency along the ray path (satellite position ① in Fig. 15), or a frequency very near the local two-ion resonance frequency (satellite position ②), whichever is bigger. This constitutes a "window" limiting the frequency range of observable 1^{-} proton whistlers. As the satellite moves to higher latitudes this window becomes narrower to a point where it collapses. This limiting latitude is indicated in Fig. 15 and it happens where the local two-ion resonance frequency equals the equatorial value of proton gyrofrequency. Above that latitude, a satellite in circular or near circular orbit will not be able to detect any additional 1^{-} proton whistlers. It should be understood that the results indicated by Fig. 15 are only approximate, since the damping due to temperature effects near the resonances have not been taken into account quantitatively. The above mechanism is very adequate to explain all the features of 1^{-}

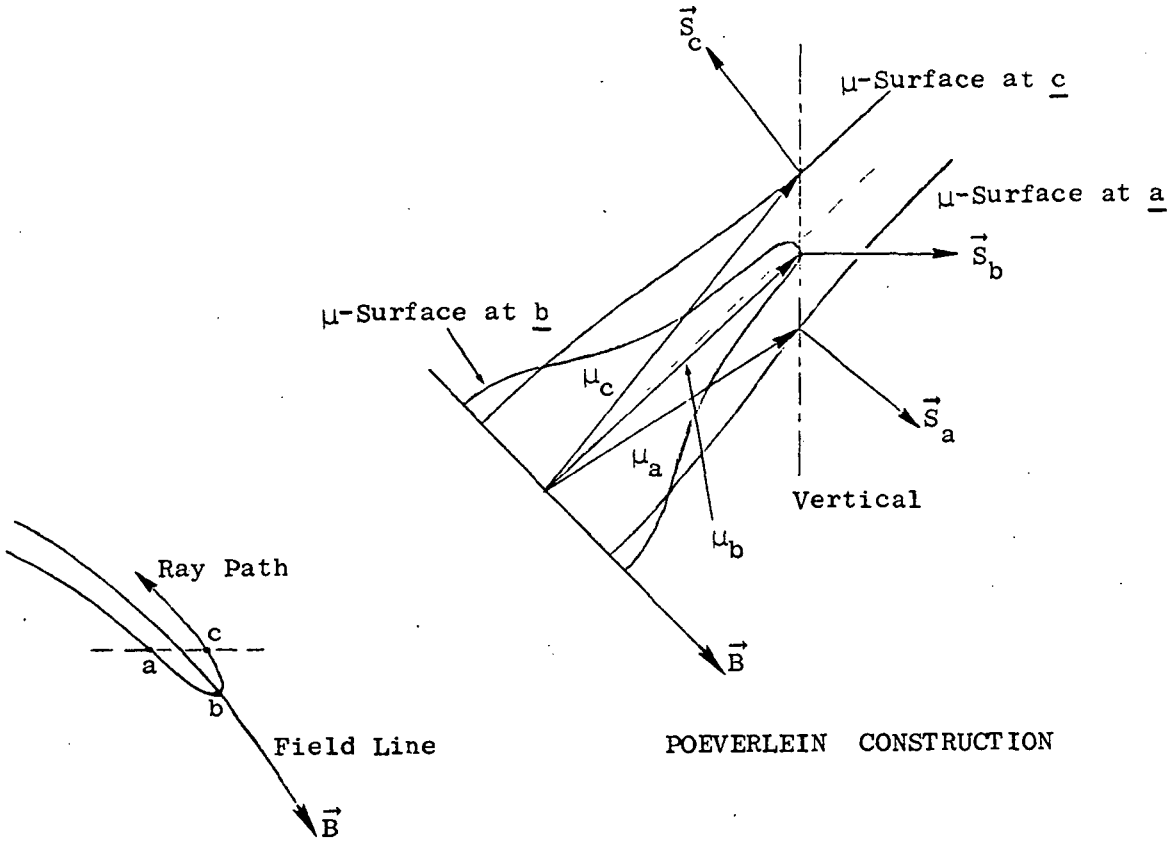

FIGURE 16. MECHANISM OF REFLECTION OF A WAVE IN THE SLOW MODE WITH LARGE WAVE NORMAL ANGLES, ACROSS THE TWO-ION RESONANCE LEVEL.

proton whistlers illustrated in Fig. 13, including their disappearance around -19^{o} dipole latitude.

Finally, one comment about the polarization of these whistlers. Due to the fact that the crossover level marks a region of polarization reversal, the actual polarization of the received 1^{-} proton whistlers will depend on the relative position of the satellite among the characteristic frequency curves. For example, in Fig. 15, the 1^{-} proton whistler received at satellite position ① is almost entirely left-hand polarized (except for the narrow frequency range below the local cross-over frequency), but the one received at position ② is entirely right-hand

polarized!

C. THE ION CUTOFF WHISTLER

The previous section dealt with effects of ions upon waves in the "slow mode." The ion cutoff whistler, on the other hand, is the result of ion effects on the "fast mode." It was discovered in recordings of the OGO-2 and OGO-4 satellites and interpreted on the basis of a reflection of downward propagating waves close to the two-ion cutoff frequency [Muzzio, 1968a,b], hence the denomination ion cutoff whistler. Some examples of this event are shown in the spectrograms of Fig. 17. Events (a) and (b) were detected over Australia, around a dipole latitude of -40^{o} and events (c) and (d) were detected at Santiago (Chile), at a dipole latitude of -21^{o}. The measured frequency-time curve for these whistlers fits a constant dispersion (Eckersley type) curve over most of the range 0-10 kHz. However, at the low frequency end the trace deviates towards increasing time delays, reaches a turning point or minimum frequency and then rises in frequency to some extent. Sometimes the trace is seen down to the minimum frequency only, the return portion being absent.

Comparison of the observed whistlers with Eckersley curves indicate dispersions of about 40 $sec^{1/2}$ for the examples of Fig. 17a,b, and about 30 $sec^{1/2}$ for the examples in Fig. 17c,d. These figures suggest the origin to be in the conjugate hemisphere, in other words, they are 1^{-} whistlers. The values of proton gyrofrequency at the two locations shown in Fig. 17 are: 570 Hz for (a) and (b), and 300 Hz for (c) and (d). The corresponding minimum frequencies of the whistlers are lower than the above values of gyrofrequency, as can be seen in Fig. 17. The rapid decrease in the refractive index of the fast mode when approaching the

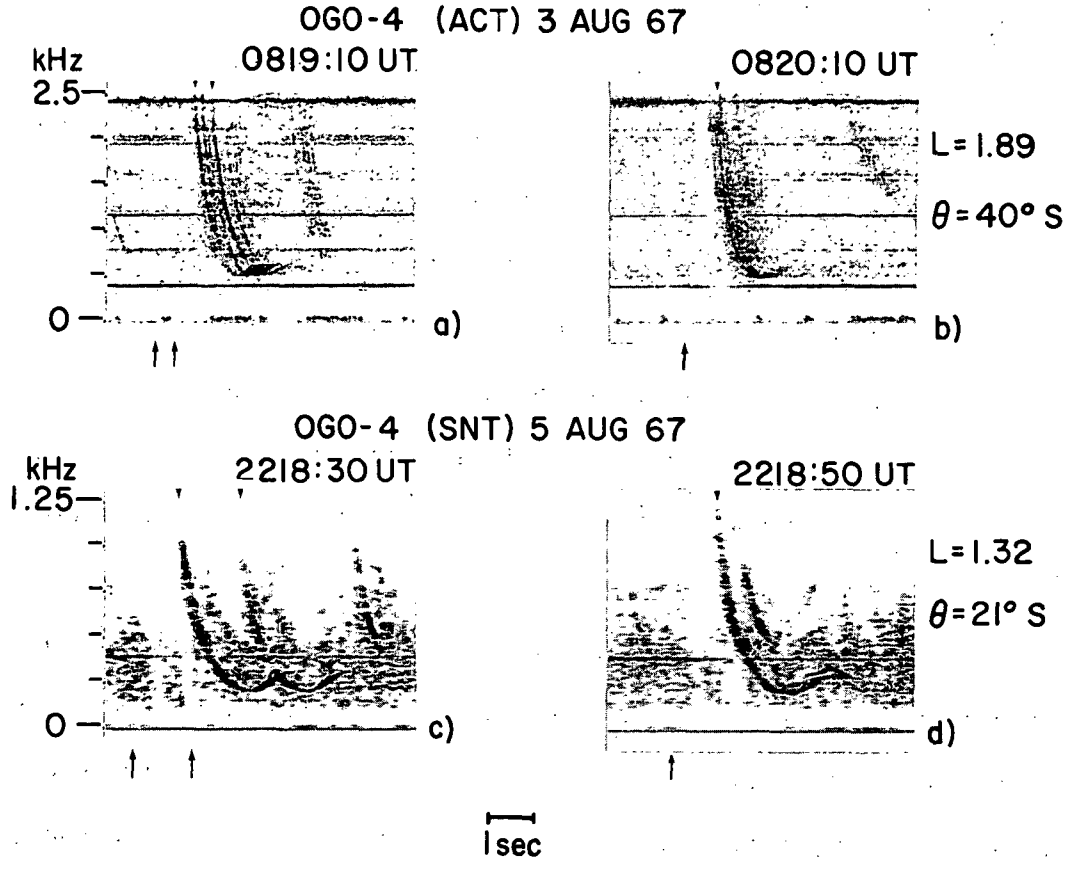

FIGURE 17. EXAMPLES OF ION CUTOFF WHISTLERS DETECTED AT TWO DIFFERENT LATITUDES. In the upper and lower panels, f_m and F_H are, respectively, the minimum frequency and the local proton gyrofrequency.

two-ion cutoff level creates a reflection condition for waves propagating downwards. This reflection can be understood by the application of Snell's law or by the Poeverlein construction illustrated in Fig. 18. As a matter of fact, the analysis of the rate of change of wave normal angle along the ray path undertaken in Chapter 2 shows a very steep increase in $d\psi/ds$ when the two-ion cutoff level is approached from above. The peculiar low frequency end of the whistlers in question suggests therefore, that the rays are being reflected somewhere below

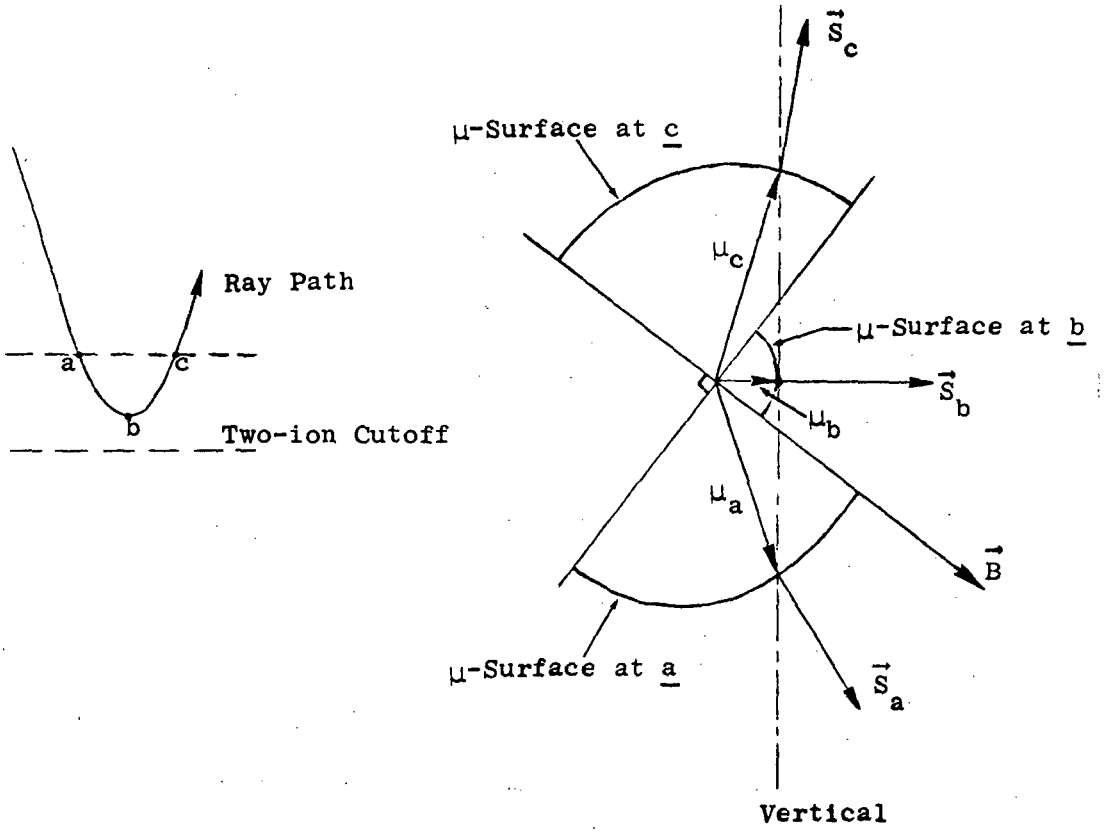

FIGURE 18. REFLECTION OF A WAVE IN THE FAST MODE (PROPAGATING DOWNWARD) NEAR THE TWO-ION CUTOFF LEVEL.

the satellite and cross the satellite orbit once more on the way up. Figure 19 illustrates the above argument. The curves marked f_c and F_H represent, respectively, the two-ion cutoff and the proton gyro-frequencies as a function of altitude. In the absence of coupling around the crossover level, a wave of frequency f propagating downward in the fast mode passes by the satellite at h_1, is reflected near the cutoff level and may be detected a second time on the way up. The time interval Δt between the reception of the downward and upward signals depends on the distance Δh between the satellite altitude and the

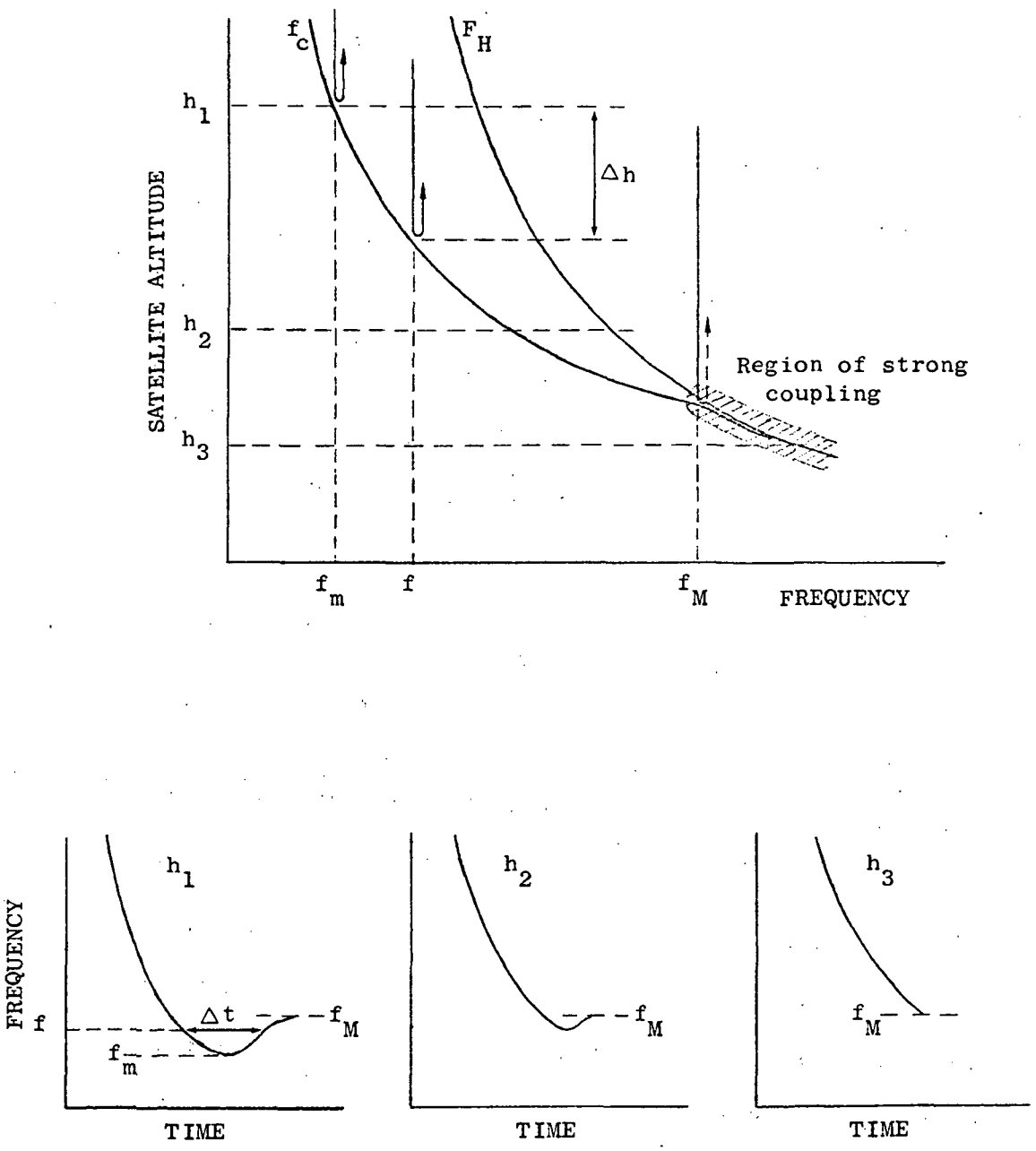

FIGURE 19. ON TOP, CURVES OF PROTON GYROFREQUENCY AND TWO ION CUTOFF FREQUENCY AS A FUNCTION OF ALTITUDE. In the lower panel, spectra of ion cutoff whistlers received at the three satellite altitudes h_1, h_2 and h_3.

reflection altitude, and also on the group velocity. The minimum frequency observed (f_m) must be reflected at the satellite altitude. Frequencies lower than f_m are reflected above the satellite and can not be detected. This mechanism of reflection of ion cutoff whistlers proposed by the author in 1968 has been experimentally verified later by other investigators (see Mosier [1969], Fig. 5). The maximum frequency observed in the "tail" (f_M), must correspond to the region where f_c and F_H come so close together that coupling occurs for any value of wave normal angle (on the subject of coupling, see Jones [1969a,b]). Figure 19 also illustrates what happens when the satellite altitude is decreased down to the region of strong coupling. The tail of the ion cutoff whistler is progressively shortened until it can not be observed anymore. An example of this effect can be seen in the spectrogram of Fig. 20, where the tails of the ion cutoff whistlers are barely visible. Note the low altitude ($\sim$ 430 km) in contrast with both examples of Fig. 17 where the satellite altitude was above 850 km.

One other effect that may limit the observability of the low frequency end of ion cutoff whistlers is the attenuation due to Coulomb collisions in the ionized medium. When collisions are involved, the refractive index becomes a complex quantity, a fact that is well known and will not be discussed in detail here (see for example Budden [1961]; Ratcliffe [1962]). It is possible to write a differential equation for the attenuation due to the imaginary part of the index and to incorporate this equation into a ray tracing program, for example. Following Budden [1961] and Kimura [1966] the rate of attenuation along the whistler ray path can be written as:

$$\frac{dA}{dt} = 181.92 \, f \, \frac{\chi}{\mu}$$

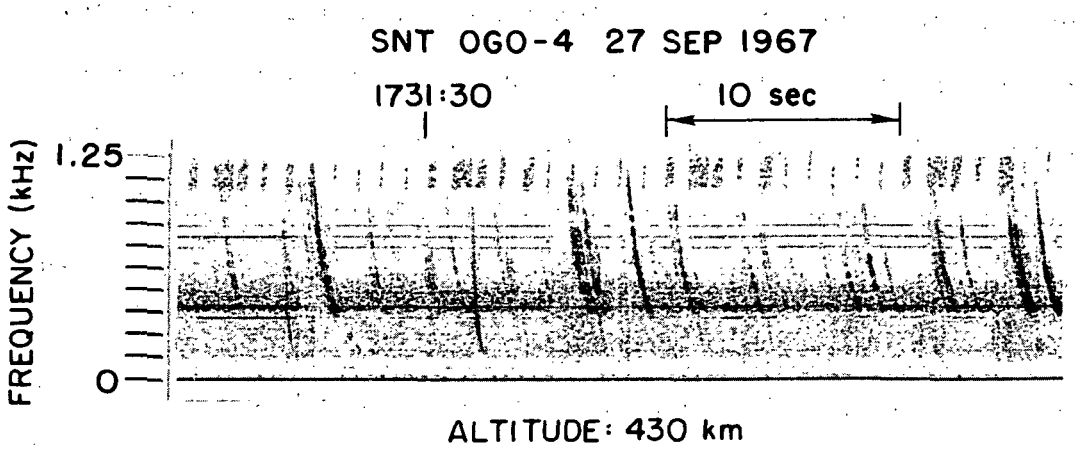

FIGURE 20. EXAMPLES OF ION CUTOFF WHISTLERS WHERE THE RETURN PART OF THE TRACE IS NOT SEEN. Notice the low satellite altitude.

where

A is the attenuation in dB

f is the frequency in Hz

χ is the imaginary part of the refractive index

μ is the real part of the refractive index

t is the time of phase travel along the ray path in sec.

In the absence of collisions, the refractive index (real) drops to zero at the cutoff frequency. When collisions are present and the index becomes complex, neither the real nor the imaginary parts can be zero anymore and in reality there are no more cutoffs. However, if the collision frequencies are small enough, μ may decrease to a sufficiently low value, close to the former cutoff, so that reflection of waves can take place. At the same time χ increases, so the resulting attenuation

may attain very large values even before reflection occurs. We are interested here in momentum transfer collisions between charged particles (electrons and ions). Expressions for the collision frequencies can be obtained from Nicolet [1953]:

$$\nu_e = 1.82 \frac{n_e}{T^{3/2}} A_1(2)$$

$$\nu_i = 4.22 \times 10^{-2} \frac{n_e}{T^{3/2}} A_1(2) \sum_{j=1}^{3} \bar{\delta}_{ij} \frac{\alpha_i + \alpha_j \eta_{ji}}{[\eta_{ji}(1+\eta_{ji})]^{1/2}}$$

where

n_e is the electron density in cm^{-3}

T is the electron temperature in ^oK

$A_1(2) = 18.7 + 2.3 \log_{10} (T^3/n_e)$

the subscripts i and j refer to the i^{th} and j^{th} ion species

$$\bar{\delta}_{ij} = \begin{cases} 0 & \text{if } i=j \\ 1 & \text{if } i \neq j \end{cases}$$

α_i is the relative concentration of the i^{th} ion species

$\eta_{ji} = \frac{m_j}{m_i}$ is the mass ratio between ion species

ν_e represent the collision frequency of the electrons with the three ion species considered throughout this work.

ν_i represent the collision frequency of each ion species with the other two. Collision of ions with electrons are disregarded because only a small fraction of the ion momentum is transfered.

The above expressions were tested in a ray tracing program with a simulated ion cutoff whistler and the resulting attenuations versus reflection altitude are plotted in Fig. 21. The attenuations are measured from the equatorial plane and only values above 1 dB are plotted. The ionospheric model is the same daytime model used in Chapter 2. For frequencies that

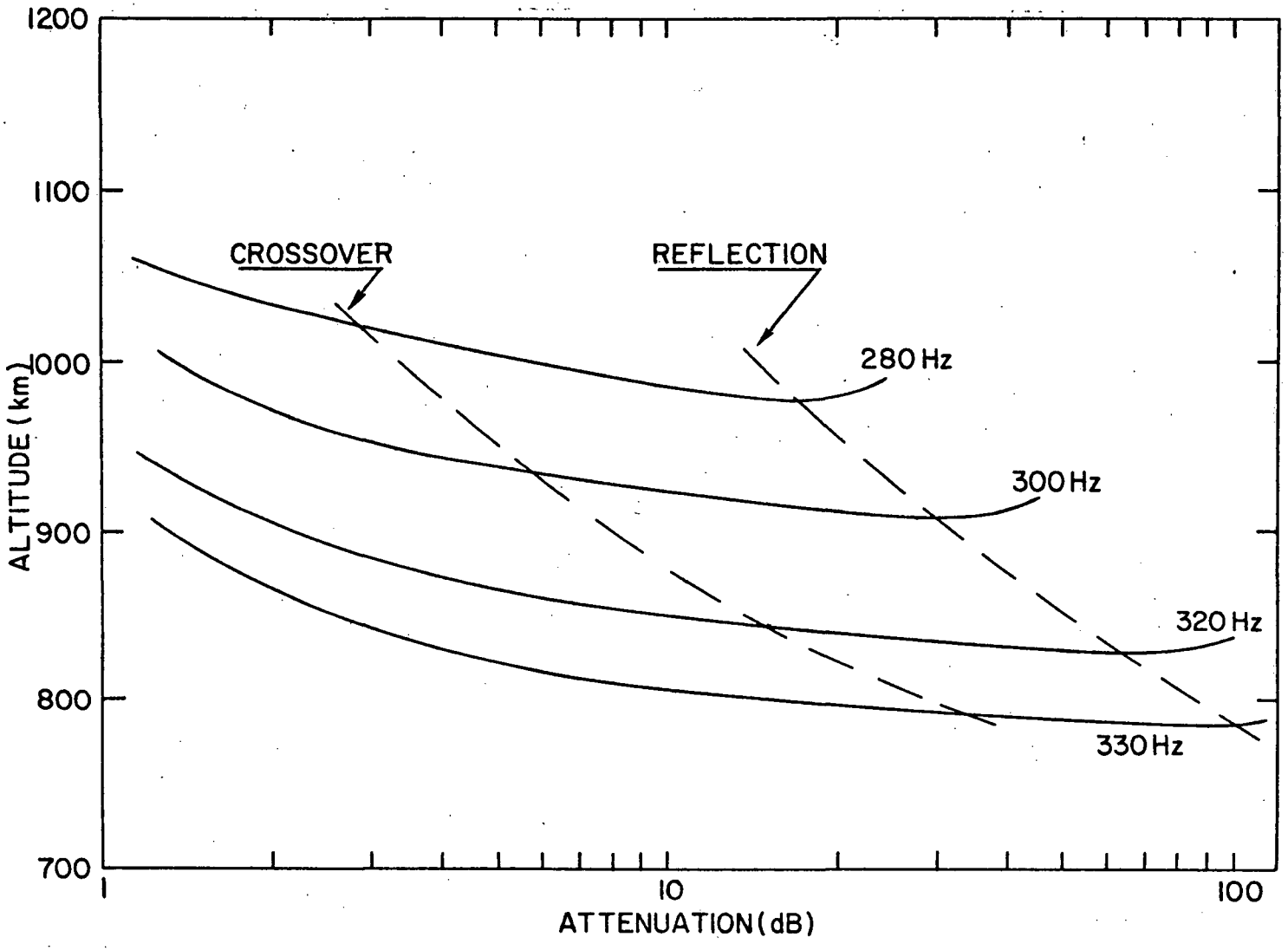

FIGURE 21. ATTENUATION VS ALTITUDE FOR WAVES IN THE FAST MODE PROPAGATING FROM THE EQUATORIAL PLANE. The attenuation is produced by the effect of Coulomb collisions. The initial wave normals are horizontal and the magnetic field intensities are applicable to a region near Santiago.

are reflected in the vicinity of 800 km altitude (or less), the attenuation is considerable, even close to the crossover level. Therefore, if the return trace is not seen in an ion cutoff whistler, one can not be sure if the apparent cutoff is caused by a reflection mechanism or by attenuation due to losses in the medium. There is still another possibility for the apparent cutoff which has to do with coupling conditions in the upward part of the ray path in the conjugate hemisphere. This condition will be dealt with in the next section regarding hybrid forms.

D. HYBRID FORMS

Having examined the propagation characteristics of the slow and fast modes separately in the last two sections, one is naturally led to ponder about the possibilities of simultaneously observing both modes associated with the same 1^- whistler trace. In fact, these hybrid forms do appear in some satellite records, and an example is shown in Fig. 22. It represents a sequence of spectra from a single pass of OGO 4. The first two panels show only ion-cutoff whistlers, but as the vehicle approaches the magnetic equator, some 1^- proton whistlers begin to appear, vestigially in (c) but stronger in (d). In (a) and (b) the satellite is too far from the equator to receive any 1^- proton whistlers (see explanation in Section B).

The spectral shape of these hybrid forms can be understood very easily by using plots of the characteristic frequencies along ray paths, as was done previously. In Fig. 23 the curves marked F_H, f_x and f_c are, respectively, the proton gyrofrequency, crossover and two-ion cutoff frequencies along a transequatorial ray path. In reality, the ray paths

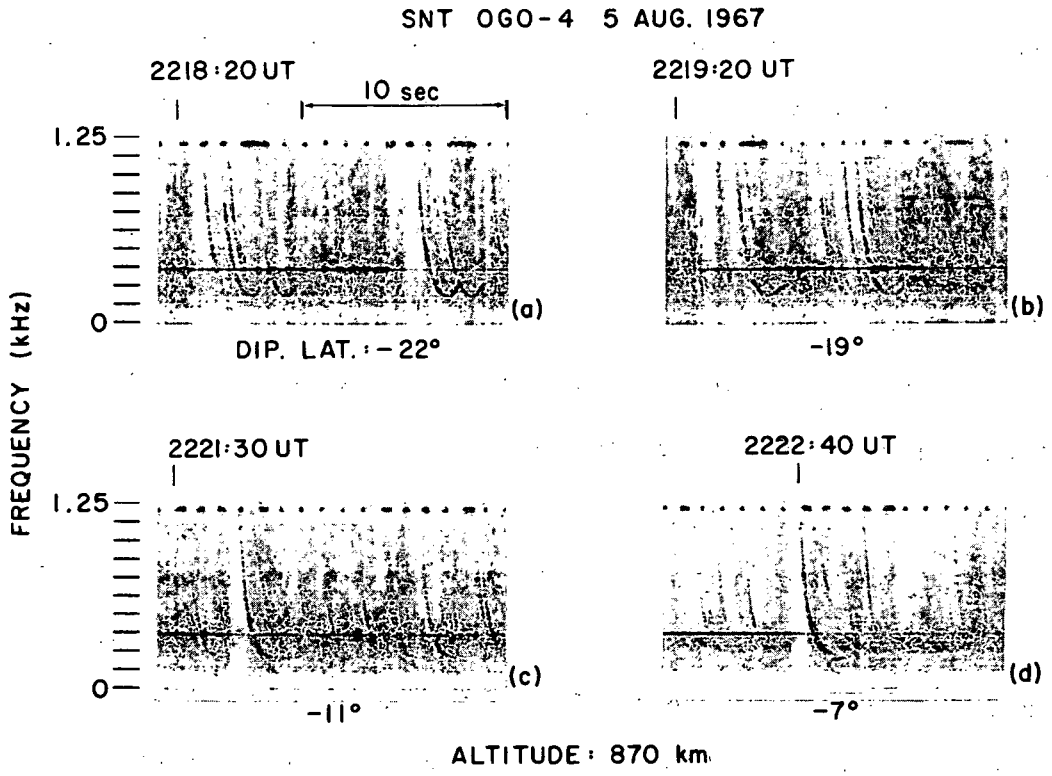

FIGURE 22. TRANSITION FROM SIMPLE ION CUTOFF WHISTLERS (IN (a) AND (b)) TO HYBRID FORMS (IN (c) AND (d)) WHEN THE VEHICLE APPROACHES THE EQUATOR.

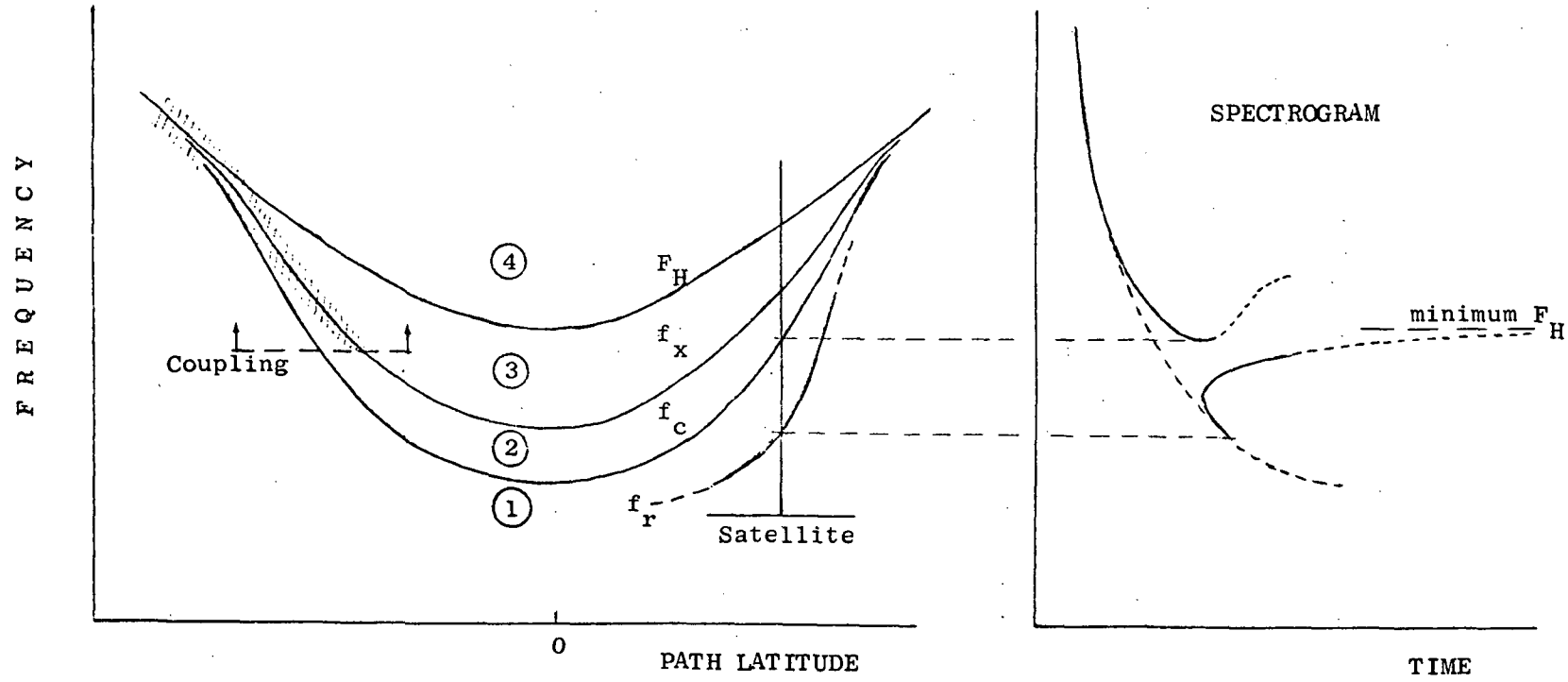

FIGURE 23. CHARACTERISTIC FREQUENCIES ALONG A TRANSEQUATORIAL RAY PATH AND SPECTROGRAM OF THE CORRESPONDING 1 HYBRID FORM.

for the two modes are not the same because of the very different shapes of the respective refractive index surfaces. However, this fact is not very important for the present discussion and would require eight curves in the diagram, an unnecessary complication. Therefore, the curves in Fig. 23 represent the characteristic frequencies along a hypothetical ray path, which is the same for both modes. The regions bounded by these curves and labeled by the encircled numbers exhibit the following properties:

1. Region ① is forbidden to the fast mode and region ④ is forbidden to the slow mode.
2. In the upward path, region ② is inaccessible to the fast mode and region ③ is only accessible if there is coupling between modes across f_x.
3. In the downward path, the transition from ③ to ② is allowed to the fast mode and there will be reflection in the vicinity of f_c. There is also the possibility of coupling across f_x.
4. In region ② the fast mode is left-hand polarized and the slow mode is right-hand polarized. Conversely, in region ③ the fast mode is right-hand polarized and the slow mode is left-hand polarized. Therefore, when there is coupling, or changing of mode, the polarization is conserved.
5. The fast mode in region ② and the slow mode in region ③ have comparatively low values of group velocity due to the large values of $\partial\mu/\partial f$.

Using the above properties in conjunction with Fig. 23, the following interpretation can be given to the hybrid forms: Frequencies below the minimum proton gyrofrequency along the path, while in the slow mode, will behave exactly as discussed in Section B (1^- proton whistlers). Above a certain frequency indicated in the figure, mode coupling becomes possible around f_x in the upward path and so the fast mode can be excited. From this point on, the fast mode will propagate as an ion cutoff whistler and everything that was said in the previous section is

applicable here. The probability of mode coupling around f_x increases when the characteristic curves approach each other, e.g., for higher frequencies (see Jones [1969a]). Ignoring for the moment the possibility of coupling in the downward path, and assuming that there is coupling in the upward path for frequencies equal or larger than the two-ion cutoff frequency at the satellite, the corresponding whistler trace received may exhibit the typical hook form (subjected to the problem of attenuation examined in the previous section). However, if conditions are such that coupling only occurs at higher frequencies, then the fast mode trace may not show any appreciable deviation from an Eckersley type dispersion curve and the cutoff seen will have nothing to do with a reflection phenomenon. These two situations are illustrated in the sketches of Fig. 24 where, in the left are seen typical "coupled" and "uncoupled" electron-proton whistler pairs detected in the upward or 0^+ path, and on the right, the corresponding forms after crossing the magnetic equator. In the uncoupled example the cutoff seen in the fast mode across the equator is the same as in the 0^+ trace and is not caused by reflection. The frequencies in the "gap" stayed in the slow mode and became trapped in region ③ (see Fig. 23).

If coupling in the downward path is taken into account, the energy could go from the fast to the slow mode across f_x before reflection close to the two-ion cutoff and a spectral form approximately equal to the sketch in Fig. 25 would result. To the author's knowledge, however, this kind of trace has not been observed yet.

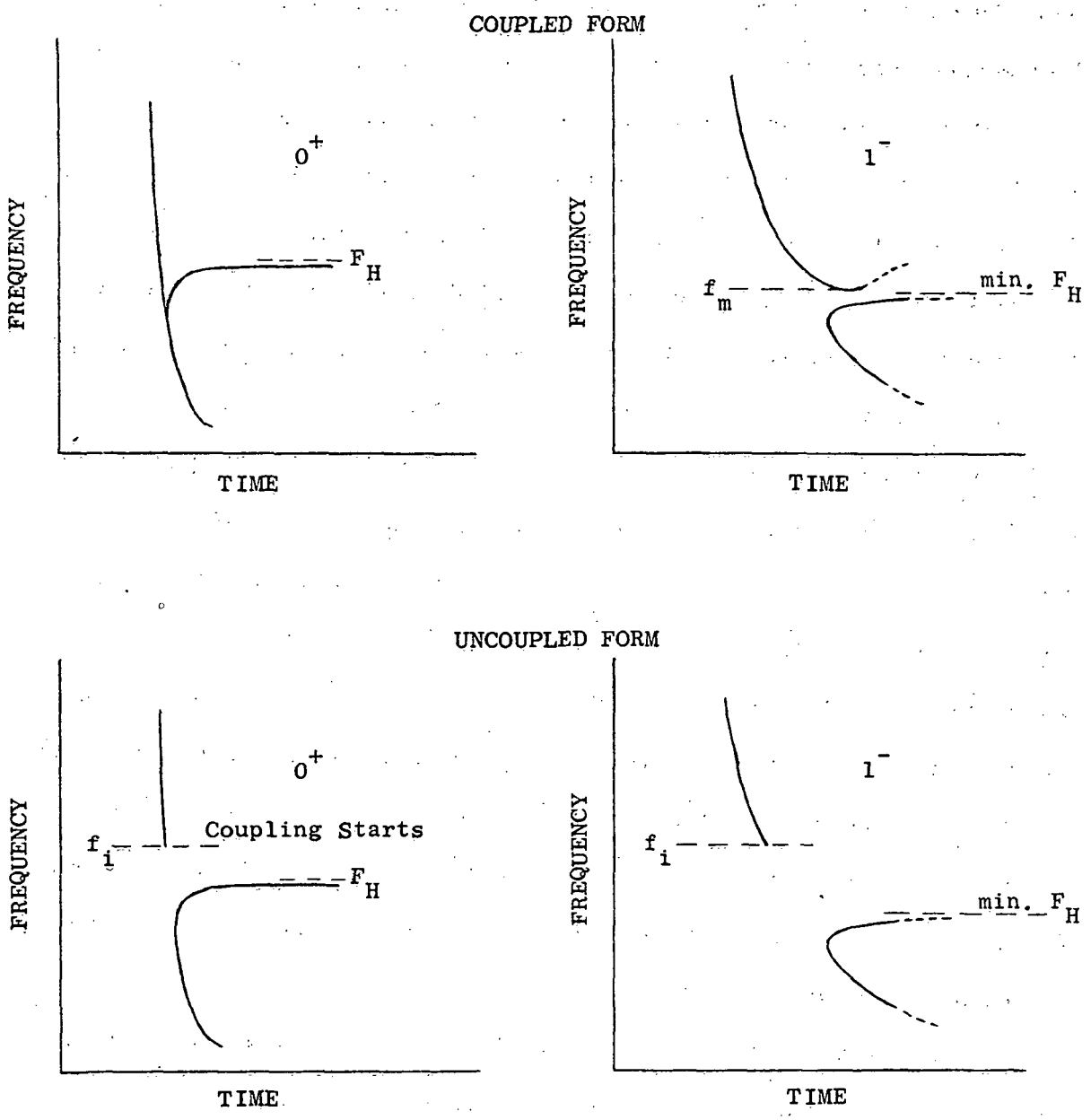

FIGURE 24. COUPLED AND UNCOUPLED ELECTRON-PROTON WHISTLER PAIRS SEEN AS 0^+ AND 1^- EVENTS. IN THE LOWER PANELS, f_i INDICATES THE FREQUENCY ABOVE WHICH COUPLING STARTS FROM THE SLOW MODE TO THE FAST MODE IN THE UPWARD PATH.

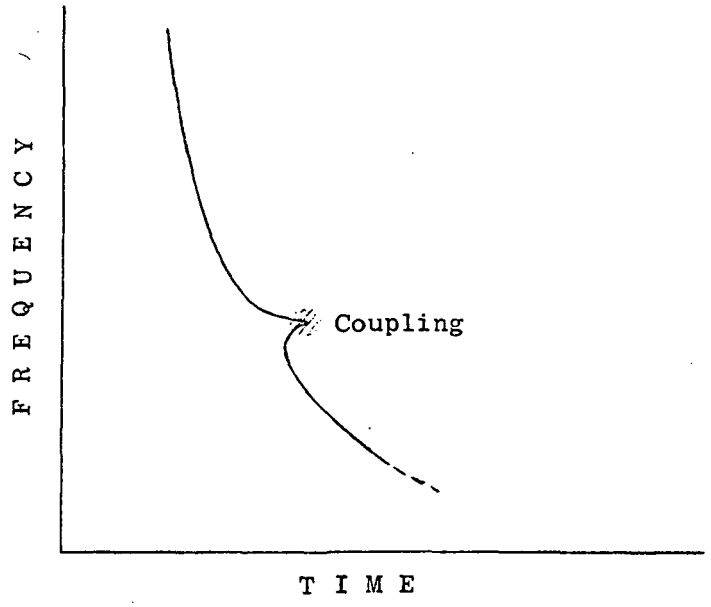

FIGURE 25. EXAMPLE OF COUPLING FROM THE FAST MODE TO THE SLOW MODE IN THE DOWNWARD PATH.

IV. ELF HISS

A. INTRODUCTION

ELF hiss or continuous noise in the range of a few hundred Hz up to about 2 or 3 kHz has been observed in the magnetosphere and reported by a number of authors (Guthart et al. [1968]; Taylor and Gurnett [1968]; Gurnett and Burns [1968]; Russell et al. [1969]; Dunckel and Helliwell [1969]; Mosier [1971]). Their work, however, deals almost exclusively with high latitude and/or high latitude events.

This chapter presents and discusses observations of ELF hiss from the Stanford University VLF experiment flown on the OGO-4 satellite ($\sim$ 430 up to 900 km altitude) and covering the entire range between $\pm 84^{\circ}$ invariant latitudes. Analysis of real time spectrogram data acquired at the Rosman (North Carolina), Quito and Santiago (South America) telemetry stations extending from September 1967 to March 1968 revealed the occurrence of a hiss band with characteristics not previously identified. The band is seen from low to medium latitudes and will be referred to as band limited ELF hiss or simply BLH. Examination of several records from the telemetry stations at Johannesburg (South Africa) and Orroral (Australia) also revealed the same kind of hiss but a more thorough analysis of data from these stations has yet to be conducted.

Furthermore, amplitude information from the digital stepping sweeping receivers of the same experiment was gathered from 14 satellite passes extending the range to $\pm 84^{\circ}$ invariant latitude. However, the results and conclusions from this sample are to be considered as preliminary until a more extensive study can be undertaken.

Based on wave propagation properties, it is proposed that the BLH is generated at large wave normal angles in the equatorial region near L = 4. This model can be used to explain the characteristics of the BLH and also to interpret previous observations of ELF hiss reported by Russell et al. [1969] and Mosier [1971]. Two mechanisms for the generation of the BLH based on radiation from energetic electrons are considered. However, in order to explain the observed intensities, some form of wave growth or a coherency mechanism is required.

B. OBSERVATIONS

The ELF hiss detected by OGO 4 exhibits the typical low frequency cutoff described by Gurnett and Burns [1968] and attributed to the two-ion cutoff in the dispersion relation. It also shows the following remarkable characteristics illustrated in the spectrograms of Fig. 26:

1. The presence of a high intensity hiss band at low to medium latitudes below ~ 600 Hz (BLH). When spectrograms covering a broad latitude range are examined, one generally observes ELF hiss extending from the lower cutoff (associated with the two-ion cutoff frequency) up to 2 or 3 kHz and from the equatorial through the auroral region (auroral hiss). In such a spectrogram, however, the BLH stands out as the strongest and steadiest signal in its latitude range. The hiss above the BLH is irregular and with a variable spectrum from day to day. Figures 26 and 28 illustrate different aspects of the background hiss and the BLH.
2. The upper cutoff of the BLH in the vicinity of 600 Hz, which seems to be independent of latitude and is virtually the same in both hemispheres.
3. The "equatorial erosion" or sloping upper cutoff decreasing in frequency toward the equator, near $\pm 10^{\circ}$ dipole latitude. It affects both the BLH and the background hiss. An equatorial erosion with a similar spectral cutoff has been previously observed in whistlers [Scarabucci, 1970] but, according to that author, it is produced mainly by absorption in the lower ionosphere. There are examples of simultaneous occurrences of erosion in the BLH and in whistlers, although the frequency ranges are different. Also, in some instances, the BLH exhibits the erosion and the whistlers do not.

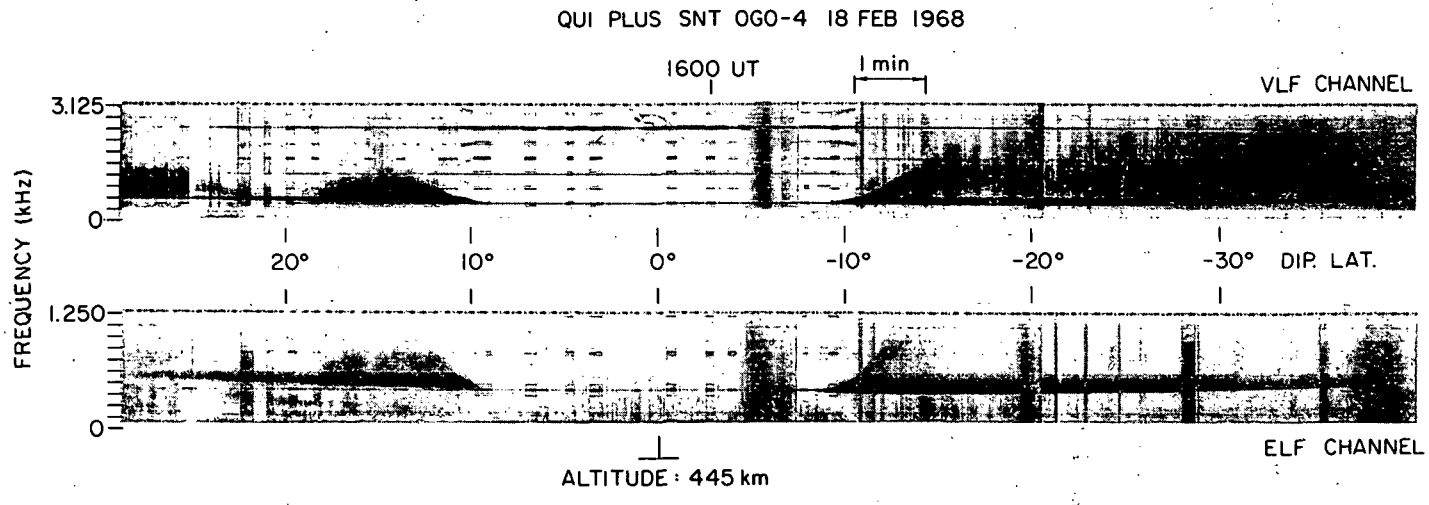

FIGURE 26. SPECTROGRAMS OF THE BLH (FROM THE TWO BROADBAND RECEIVERS OF OGO 4) ACROSS THE EQUATORIAL REGION. Notice the steadiness of the BLH when compared to the variable hiss above 600 Hz.

Prior to this work, observations of ELF hiss by other investigators had established only that the lower frequency was controlled by the two-ion cutoff [Gurnett and Burns, 1968]. Reported observations were confined to invariant latitudes greater than $\sim 35^{\circ}$, which precluded most investigators from observing the equatorial erosion. To the author's knowledge, there are no references to the virtually constant upper cutoff of the BLH with latitude.

The upper and lower cutoffs of the BLH taken from the spectrograms shown in Fig. 26 are plotted vs the absolute value of dipole latitude in Fig. 27. Although the lower cutoff is markedly lower in the southern hemisphere (due to the lower values of local magnetic field near the South Atlantic anomaly) the upper cutoff remains essentially the same in both hemispheres.

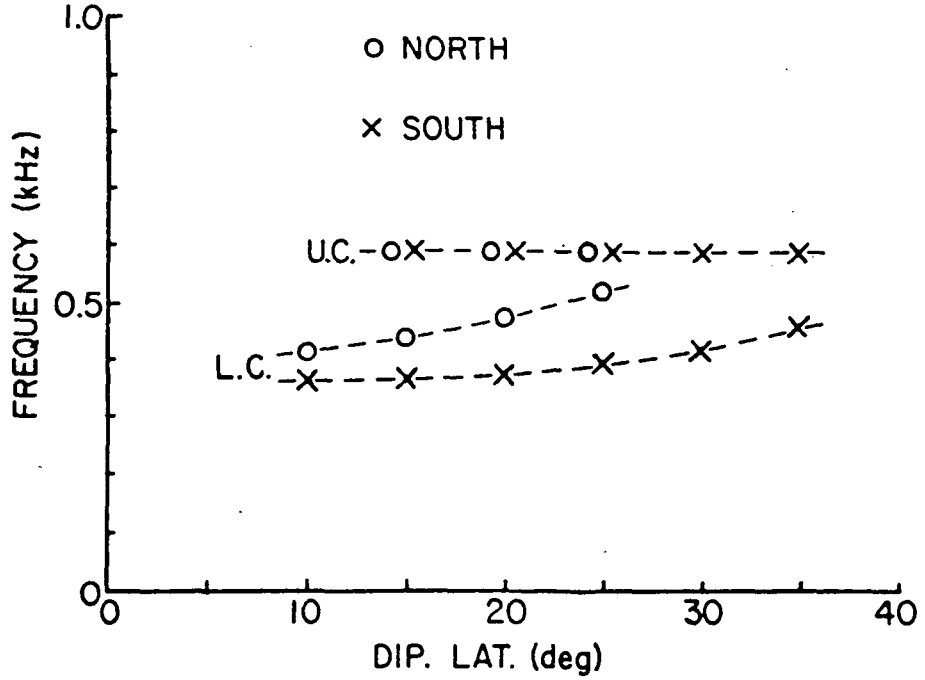

FIGURE 27. VALUES OF THE UPPER AND LOWER CUTOFFS OF THE BLH SHOWN IN THE SPECTROGRAMS OF FIG. 26, PLOTTED VS DIPOLE LATITUDE. Although the lower cutoffs at conjugate latitutdes are markedly different due mainly to differences in local magnetic field, the upper cutoffs are essentially the same.

Figure 28 depicts two other spectrogram similar to the ones in Fig. 26 but recorded at higher latitudes by the Rosman telemetry station. Hiss and chorus up to $\sim$ 2 kHz beyond 65^{o} invariant latitude can be seen. On this record, the BLH is observed up to $\sim 55^{o}$ invariant latitude, where the upper and lower cutoffs merge. Above this latitude the lower cutoff can still be seen in the background hiss until its gradual disappearance around 58^{o} invariant latitude. This disappearance of the lower cutoff is consistent with the reported decrease in the H^{+} relative concentration at high latitudes (see Taylor et al. [1969]), which greatly increases the probability of coupling for downgoing waves around the crossover altitude (for a study of the variations of the coupling coefficient with ion concentration, see Gurnett et al. [1965]; Jones [1969a,b]; Rodriguez and Gurnett [1971]). To the author's knowledge this phenomenon has not been identified previously, although it can be seen in Fig. 5 of Rodriguez and Gurnett [1971]. The light ion trough seems to be a manifestation of the plasmapause. In this case, the decrease and smearing of the lower cutoff of the ELF hiss can provide a convenient way of determining the plasmapause location.

In what follows we will be discussing mostly the properties and characteristics of the BLH. Examination of 270 occurrences (from spectrograms of the OGO-4 broadband receivers) of hiss between September 1967 and March 1968 from Rosman, Quito and Santiago revealed the following characteristics:

1. The BLH was seen in nearly all passes between 0600 and 2200 LT. No occurrences of the BLH were observed in the broadband data after $\sim$ 2300 LT, although a few examples were found in the digital data (with smaller amplitude). The smaller amplitude of the nighttime events may be the reason why they have not been observed in the broadband receivers. A more extensive examination of the digital amplitude data is, therefore, recommended.

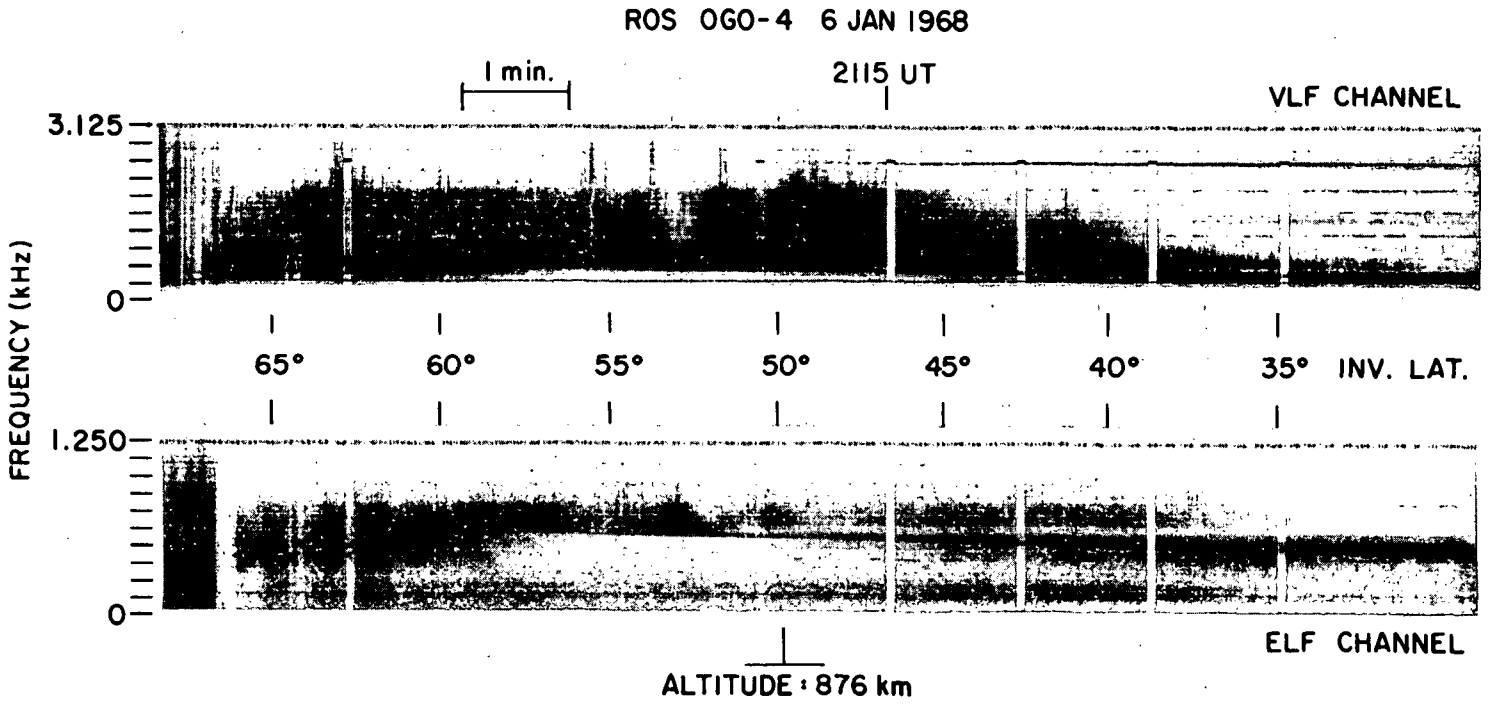

FIGURE 28. ANOTHER EXAMPLE OF BLH RECORDED AT HIGHER LATITUDE (ROSMAN). The BLH is seen up to $\sim 55^{\circ}$ invariant latitude, where the lower and upper cutoffs merge. The gradual disappearance of the lower cutoff of the hiss between 58° and 60° is probably due to the H^{+} trough reportedly observed at the plasmapause and could provide a convenient way to determine its location at low altitudes.

2. The equatorial erosion is present in all records that cover the region around $\pm 10^{\circ}$ dipole latitude, and there is a marked symmetry in the phenomenon with respect to the magnetic equator.

3. The upper cutoff of the BLH in the vicinity of 600 Hz is nearly independent of satellite latitude above $\sim 15^{\circ}$ and its sharpness shows variations from pass to pass. However in $\sim 40\%$ of the passes examined the sharpness is comparable to that in Figs. 26 and 28. After prolonged periods of low magnetic activity the upper cutoff frequency decreases to values as low as 420 Hz, but recovers about one day after a sharp increase in activity (such as a sudden commencement). Figure 29 illustrates the change in upper cutoff after the quiet period from 7 to 9 March 1968. The spectrogram on the left (March 2) is typical of the period indicated from 1 to 6 March and has an upper cutoff of ~ 590 Hz. The spectrogram in the center (March 10) shows the decrease of the upper cutoff to ~ 470 Hz after three days of low activity ($K_p \leq 2$), and finally the one on the right shows the recovery of the upper cutoff to ~ 550 Hz one day after a sudden commencement. Similar decreases of the upper cutoff frequency have been observed during other calm periods (around November 18 and December 13, 1967).

Table 1 shows the average values of upper cutoff from Rosman and Santiago data during the months of January and March 1968. These data were selected from the cases of sharpest upper cutoff, excluding the periods of extremely low magnetic activity, such as the days preceding March 10 (see Fig. 29). The table also shows the standard deviations (σ) and solar zenith angles (χ) for two approximately conjugate points ($\pm 35^{\circ}$ dipole latitude). The months of January and March were chosen in order to provide a variety of ionospheric illumination conditions at both stations (as can be seen by the values of χ). The closeness between the resulting average values of upper cutoff frequency plus the fact that near Santiago the geomagnetic field intensity is $\sim 25\%$ lower than near Rosman indicate a lack of control of the upper cutoff frequency by the local ionosphere. Although the uncertainties involved in the determination of the cutoff frequency from the spectrograms are of the order of 3%, the average values for Rosman were consistently higher than those for Santiago (2.9% in January and 3.7% in March). This small difference

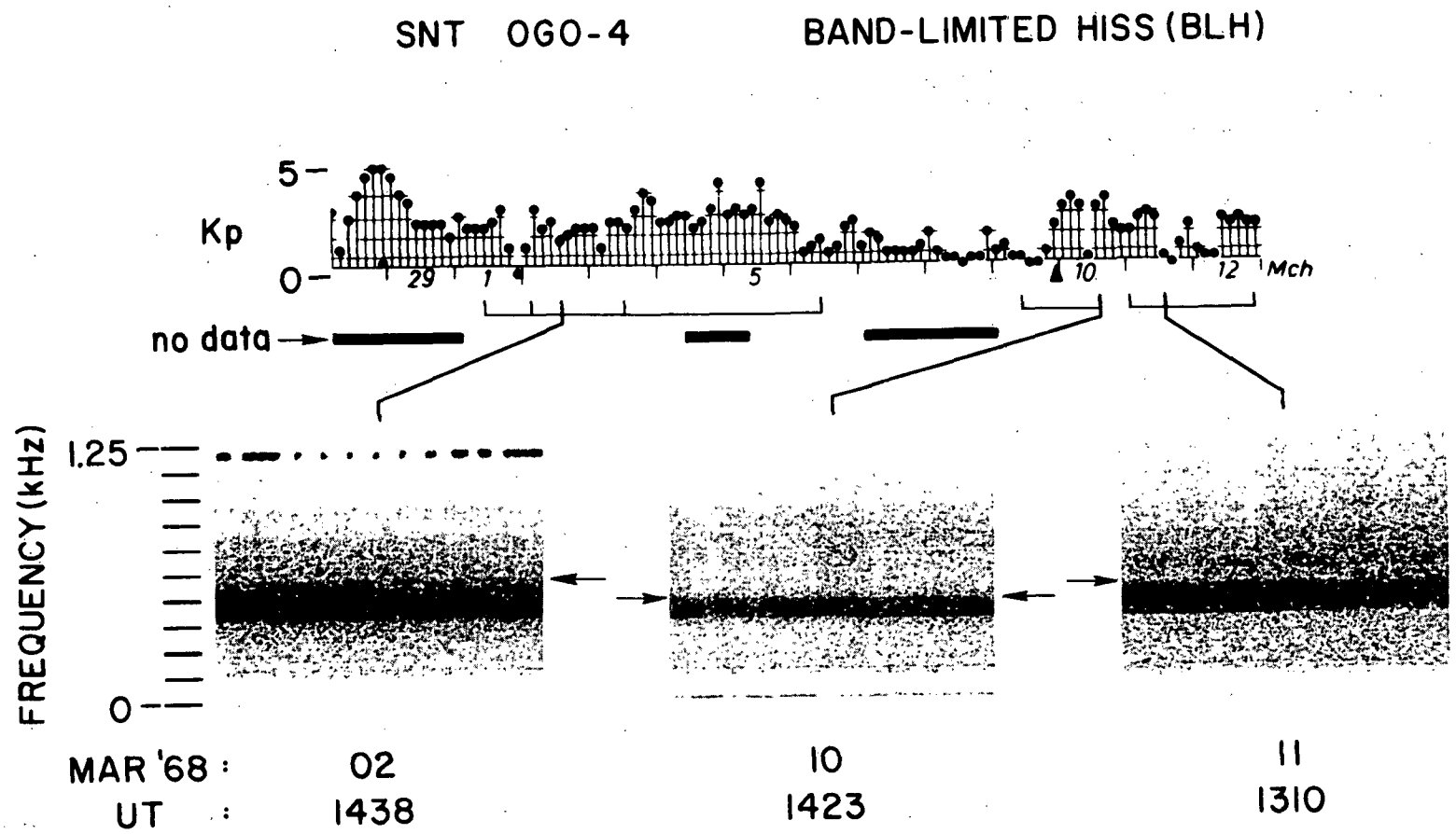

FIGURE 29. DECREASE IN THE UPPER CUTOFF OF THE BLH AFTER PERIODS OF LOW MAGNETIC ACTIVITY AND SUBSEQUENT RECOVERY AFTER A SUDDEN COMMENCEMENT (MARCH 11). Notice the time lag of approximately one day between the sudden commencement and the recovery of the upper cutoff toward its normal value ($\sim$ 590 Hz).

may be attributed to the slight increase in upper cutoff with latitude, which will be discussed later (Fig. 36).

TABLE 1. UPPER CUTOFF FREQUENCY OF THE BLH.

	January 1968 (1330 LT)				March 1968 (0800 LT)			
Station	Average Value (Hz)	σ (Hz)	χ	No. Cases	Average Value (Hz)	σ (Hz)	χ	No. Cases
ROS	582	7	40^{o}	13	591	12	63^{o}	11
SNT	565	19	32^{o}	13	569	15	70^{o}	12

As mentioned in the introduction some measurements of the amplitude of the signals were made using data from the sweeping receivers of OGO 4. These receivers cover three consecutive bands. Band 1, used here, has a bandwidth of 40 Hz and sweeps through 256 steps in the frequency range 0.15 to 1.54 kHz every 73.6 seconds in the low bit rate (4 kb/sec). This information is recorded on magnetic tape aboard the satellite and can be transmitted to the ground on command from the telemetry stations, providing measurements along a full orbit. For more details on the experiment see Rorden et al. [1966]. The quantity measured is the magnetic field B of the waves and Fig. 30 shows an example of such a measurement for the pass illustrated in Fig. 26. The upper panel shows a portion of the spectrogram of Fig. 26 containing the erosion on the northern hemisphere side. The time scale here is expanded in relation to Fig. 26 and the diagonal straight line across the spectrum represents the sweep of the band 1 sweeping receiver shown in the lower panel. The corresponding amplitude, in db below 1γ, versus frequency shows the variation in signal strength

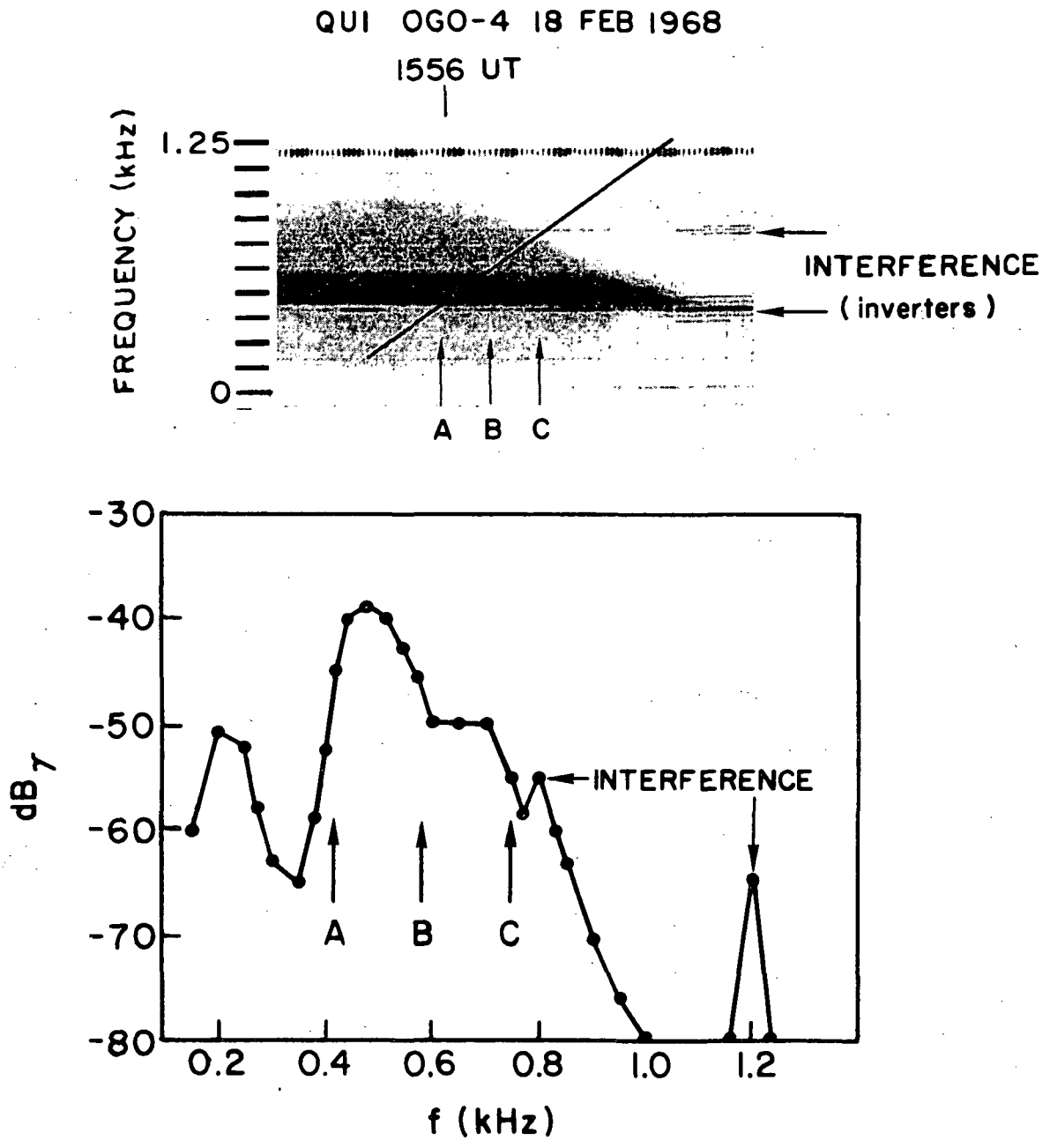

FIGURE 30. MEASUREMENT OF THE AMPLITUDES OF THE BLH AND THE BACKGROUND HISS IN THE REGION OF THE EQUATORIAL EROSION. The quantity being measured is the wave magnetic field.

across the two cutoffs (A and B) and the erosion (C). The spikes identified as interference appear usually at multiples of 400 Hz and are caused by inverters aboard the satellite. Along the sweep reproduced in the figure, the interference at 400 Hz is not seen. However, in the spectrogram, the lines at 400 Hz and 800 Hz can be easily identified. The noise level of the band 1 sweeping receiver varies from -60 dBγ ($2.5 \times 10^{-8} \gamma^2/Hz$) at 200 Hz to -97 dBγ ($5 \times 10^{-12} \gamma^2/Hz$) at 1500 Hz. The small peak at 200 Hz seems to be real since it is only observed at low latitudes, but it has not been interpreted yet.

In order to have a sample of how the amplitude of the noise varies with latitude, measurements were made along four orbits covering a range of $+84^o$ to -84^o invariant latitude. Two of the passes were on February 18 and the other two on February 22, 1968. The result, plotted in units of γ^2/Hz versus invariant latitude appears in Fig. 31a,b. For each of the orbits, the amplitudes at three sets of frequencies were chosen for illustration: 600 Hz (immediately above the BLH) represented by dashed lines, 1000 Hz represented by continuous lines, and the frequency of maximum intensity in the BLH represented by dash-dot lines. Three of the four passes in Fig. 31 do not show recordings of amplitude for the whole range of latitudes covered by the satellite due to changes in the mode of operation of the spacecraft.

The equatorial erosion is clearly visible and amounts to attenuations of 20 to 33 dB (at 600 Hz) between two consecutive sweeps, corresponding to a change in latitude of about 4^o. The maximum intensities at 600 Hz and 1000 Hz occur in the vicinity of $\pm 60^o$ invariant latitude and may be of the order of $10^{-4} \gamma^2/Hz$. Beyond $\pm 70^o$ the intensities decrease quite rapidly and at approximately $\pm 84^o$ the background noise levels of the

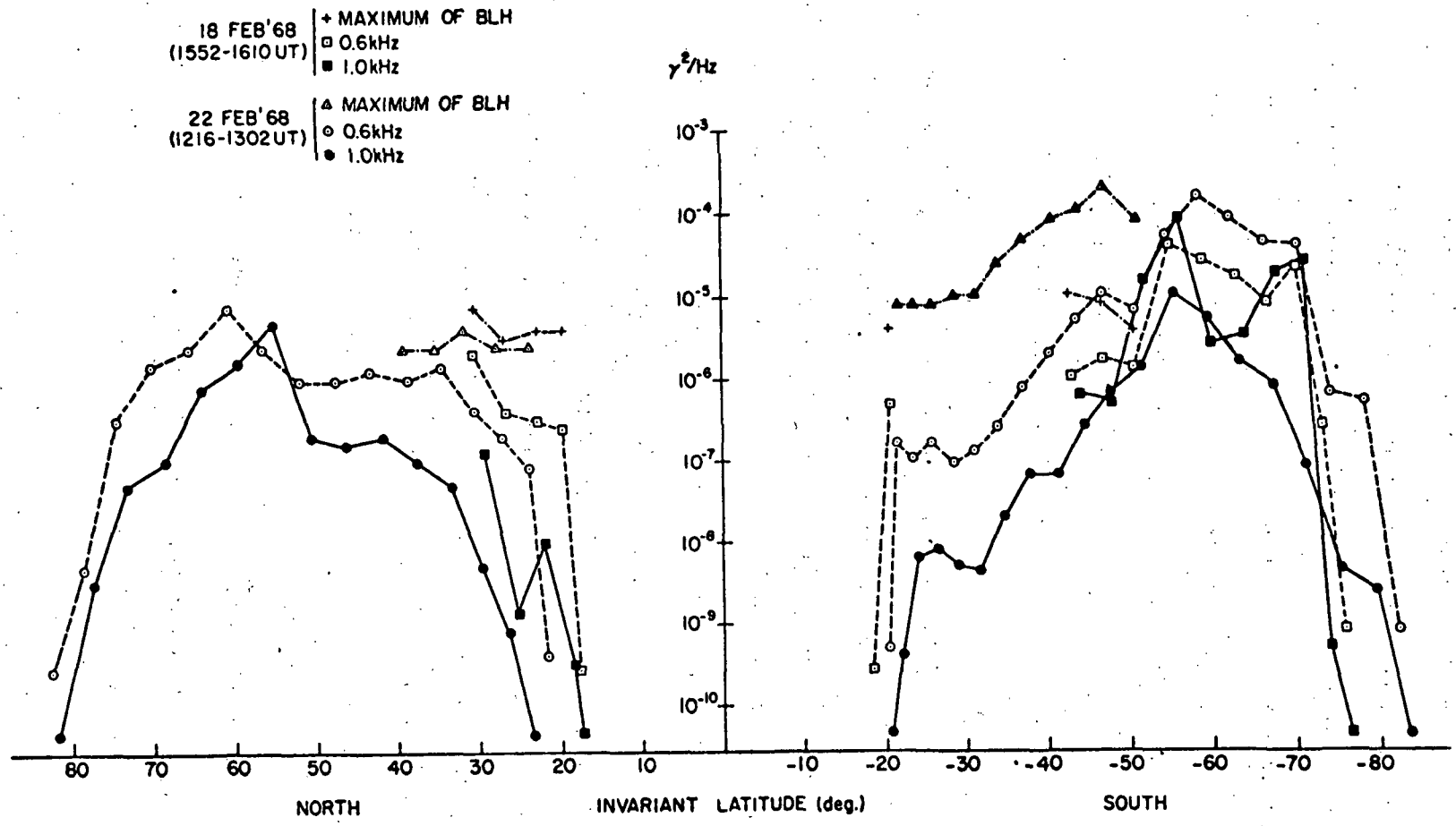

FIGURE 31a. INTENSITY OF THE HISS IN γ^2/Hz VS INVARIANT LATITUDE FOR TWO SATELLITE PASSES DURING FEB '68. Continuous lines correspond to 1000 Hz, dashed lines to 600 Hz (above the BLH) and the dash-dot lines to the maximum intensity of the BLH. The equatorial erosion is clearly seen around 20° invariant latitude.

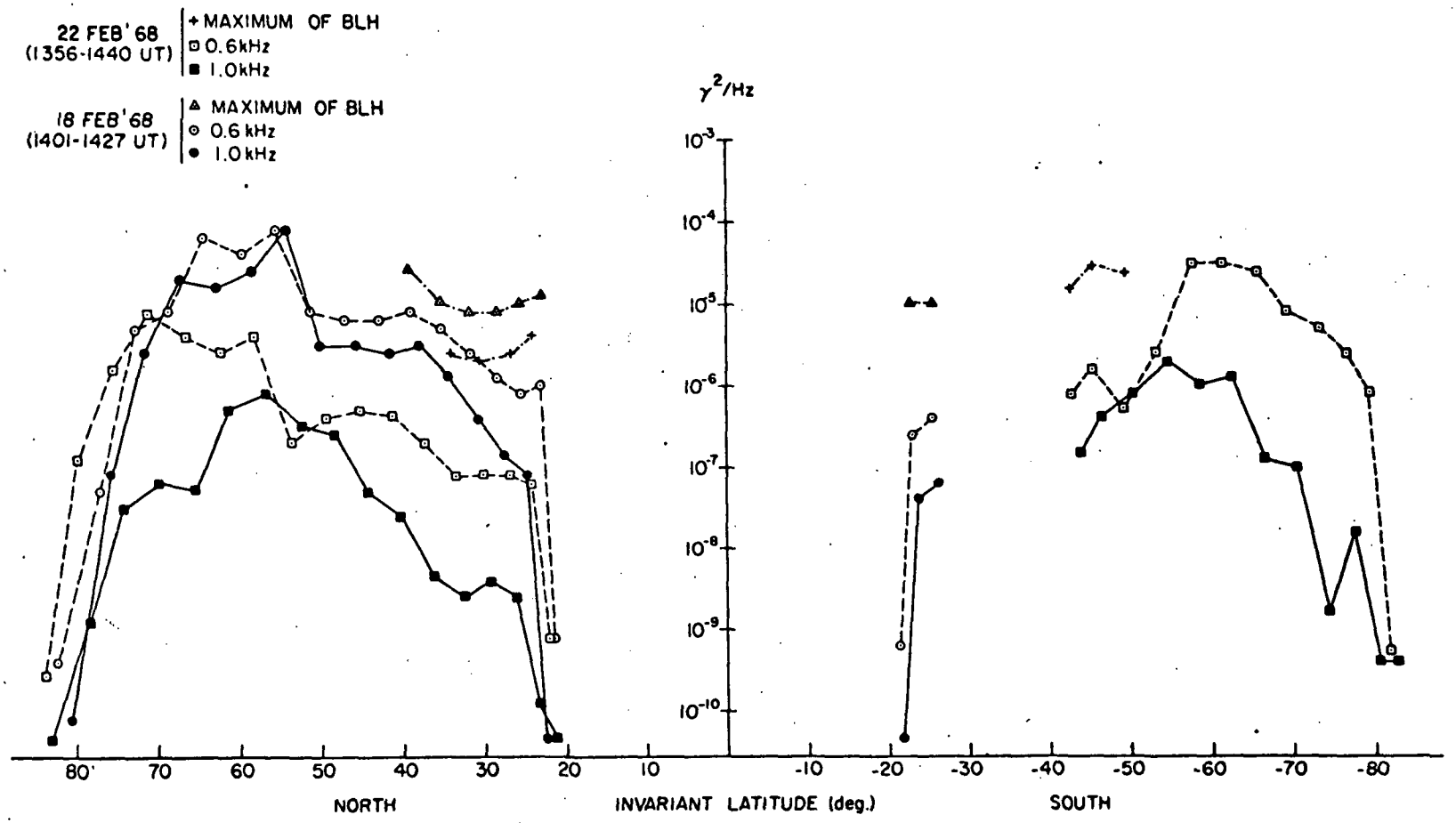

FIGURE 31b. SIMILAR TO FIG. 31a FOR TWO OTHER PASSES ON THE SAME DAYS. The BLH seems to peak between -40^{o} and -50^{o} invariant latitude, but the hiss above the BLH peaks around $\pm 60^{o}$ invariant latitude. The gaps in the latitude coverage correspond to changes in the operating mode of the satellite.

receiver are attained. In the range of 0 to 3 kHz and up to $\sim 55^{o}$ latitude the BLH is the strongest signal observed.

In Fig. 31a the maximum intensity of the BLH for the pass of 22 February in the southern hemisphere increases from -30^{o} to -46^{o} invariant latitude where it peaks at $\sim 2 \times 10^{-4} \gamma^2/\text{Hz}$. A sample of the range of intensities at 1.0 kHz and at the frequency of maximum amplitude in the BLH as a function of local time was taken from 14 OGO-4 passes between 27 December 1967 and 15 April 1968 and is shown in Fig. 32. The four groups of values correspond to longitude ranges of -40^{o} to -84^{o} (values around 1000 LT and 2200 LT) and 115^{o} to 128^{o} (values around 0400 LT and 1600 LT). The four passes of Fig. 31a,b are represented in the group around 1000 LT in Fig. 32. The amplitudes at 1.0 kHz were taken in the same latitude range as the BLH in each pass. This range is limited by the merging of the increasing lower cutoff and the essentially steady upper cutoff, already illustrated in Fig. 28. For a given satellite altitude the lower cutoff frequency increases with latitude due to the corresponding increase in local magnetic field. (At higher altitudes the lower cutoff should occur at lower frequencies and the observation of the BLH would then extend to higher latitudes.)

C. DISCUSSION

The symmetry of both the erosion and the upper cutoff in relation to the magnetic equator suggests that the BLH is generated near the equatorial plane. Since the above properties are independent of local ionospheric conditions and satellite altitude, the source is expected to be quite far away from the OGO-4 orbit.

A comparison with the observations and conclusions of previous papers

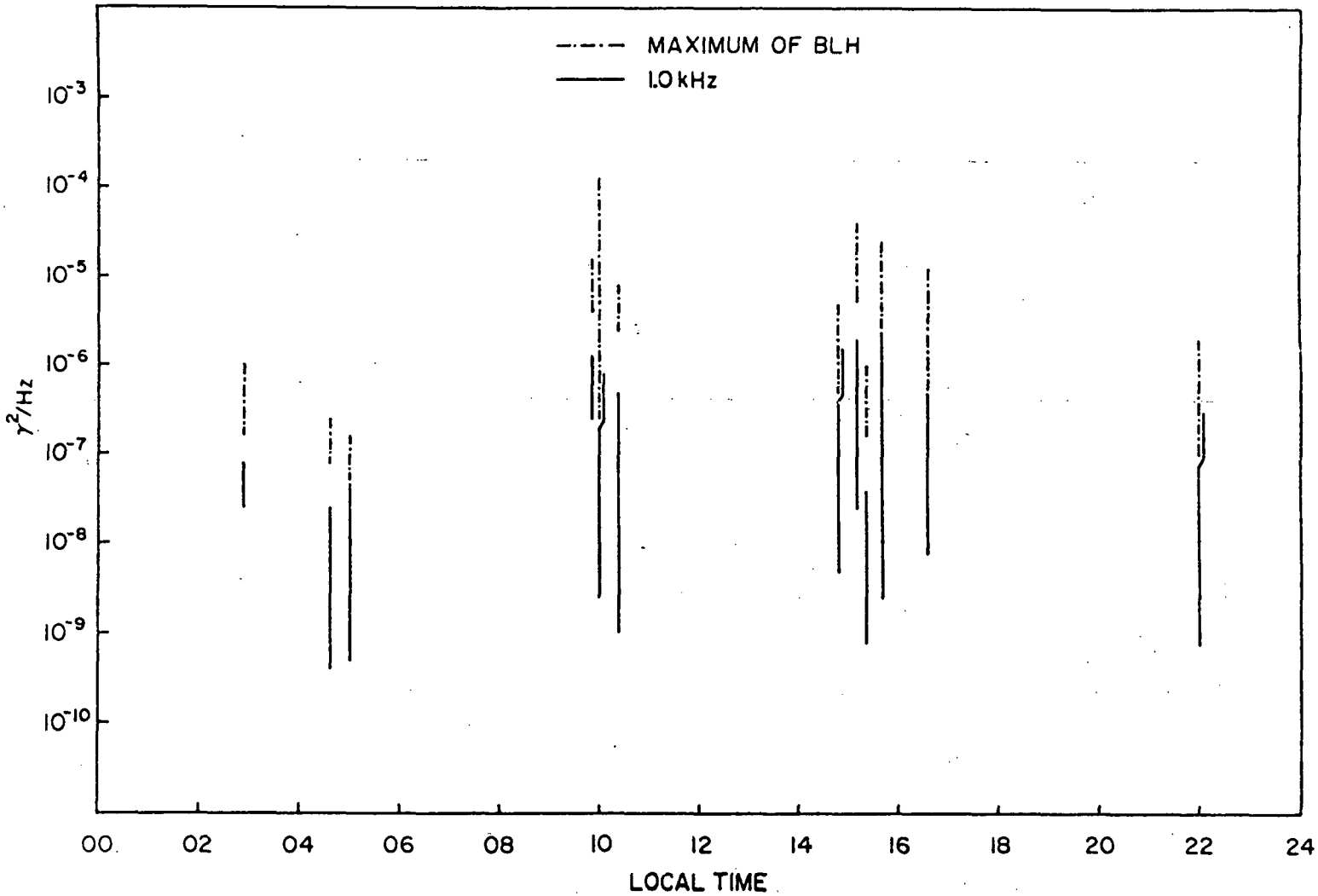

FIGURE 32. VARIATION OF THE HISS INTENSITY WITH LOCAL TIME. Both the BLH and the background hiss seem to peak around 1000 LT.

on ELF hiss is restricted by the fact that most of them deal with high latitude and/or high altitude hiss. Guthart et al. [1968] interpreted the ELF hiss observed on OGO-2 in terms of electrostatic waves. According to their theory "...The electric field $\vec{E}$ must be coupled to the loop antenna, sensitive to magnetic flux density, through its cross product with the satellite velocity $\vec{V}$ giving the magnetic field $\vec{B}$ as follows:

$$\vec{B} = \vec{V} \times \vec{E}/c^2$$

where c is the velocity of light." However, for an amplitude of $\vec{B}$ of -50 dBγ (in a 40 Hz bandwidth) the electric field required is 40 volts/m. On the other hand, our data indicate maximum intensities of $2 \times 10^{-4}\ \gamma^2/\text{Hz}$ (-21 dBγ in the same bandwidth, see Fig. 31a), which would require, in their theory, electric fields of the order of 1000 volts/m. Since electric fields of this order have not been directly observed, it seems appropriate to reject that interpretation.

Gurnett and Burns [1968] report observations of ELF hiss for invariant latitudes larger than 35° and from the description of the lower cutoff mechanism conclude that the source of this kind of emission must be located above 3000 km altitude. Although these authors did not mention the occurrence of the BLH, examination of their Fig. 3 suggests its presence below $\sim$ 600 Hz.

Using data from OGO 3, Russell et al. [1969] studied the spatial extent of ELF noise and concluded that steady noise is most common on the dayside of the magnetosphere within $L = 6$. Their strongest amplitudes of steady signal (> 4 volts in the 100, 300 or 800-Hz channels) showed a marked day-night asymmetry and were seen more frequently within $L = 5$, except between $\sim$ 40 and 50° diople latitude, where high rates of occurrence were found as far out as $L = 9$ or 10. These authors did not report

measurements below $L = 2$. From the intensity of these signals they concluded that "on the dayside at low L values, the steady signals may be generated almost anywhere along a field line up to 40° magnetic latitude but at high L values on the dayside the signals must be generated in the range 40° to 50°."

Reporting on data from OGO 1, Dunckel and Helliwell [1969] observed ELF hiss of relatively constant intensity from 0.3 kHz to as high as 3 kHz, and from $L = 2.5$ up to the vicinity of the plasmapause ($L = 4$). Maximum intensities in the vicinity of the equatorial plane occur between 06 and 16 LMT from $L = 2.5$ up to approximately $L = 4$, extending to $L = 5.5$ in the sector between 10 and 12 LMT. These maximum intensities are 16 dB above $10^{-6}\gamma^2 Hz^{-1}$. Based on the variation of upper cutoff with latitude, these authors concluded that the signals are generated close to the equatorial plane.

Studying the direction of the poynting flux of ELF hiss with the Injun 5 satellite in the region 677 to 2528 km altitude and 35° to 75° invariant latitude (in the northern hemisphere), Mosier [1971] concluded that the hiss is generated outside the plasmasphere and propagates across the plasmspause at altitudes probably below 2500 km. This conclusion is based on his remark that "...downgoing ELF hiss was observed over the entire region of altitude-invariant latitude space under study, whereas the highest latitude at which the net poynting flux of ELF hiss was directed upward is approximately 60° invariant latitude."

The possibilities offered by an equatorial source can be tested using raytracing techniques. The results, as described in the following sections, are used to interpret the several characteristics of the BLH, the observations of ELF hiss outside the plasmapause between 40° and 50°

reported by Russell et l. [1969] and also some of the poynting flux measurements of Mosier [1971]. In these ray tracings, the ionosphere model used is in diffusive equilibrium along magnetic field lines and describes quite well the daytime equatorial anomaly in the electron density. It is the same model used previously in Chapters 2 and 3.

1. Accessibility to Low Latitudes

Figures 33a,b,c show raypaths for a frequency of 600 Hz starting at $L = 3$ in the equatorial plane, for several values of the initial wave normal angle ψ_i. The wave normal angle ψ is measured from the magnetic field direction so that $|\psi| \leq 90^o$, and is positive when the wave normal points toward lower L shells. The field line represnted at $L = 4$ marks the position of a simulated plasmapause obtained by smoothly decreasing the electron density by a factor of 10 over a distance corresponding to $\Delta L \doteq 0.23$.

The lower hybrid resonance (LHR) frequency at $L = 3$ in the equatorial plane is ~ 750 Hz and so the refractive index surface at 600 Hz is closed. After the waves leave the equatorial plane, the behavior of the wave normal angle depends on its initial value, in a manner consistent with that shown by Thorne and Kennel [1967]. In the present case if $\psi_i \leq 50^o$ (Fig. 33a), ψ decreases continuously until it reaches -90^o, at which point the rays are refracted upward.

For $\psi_i > 55^o$, ψ first decreases, reaches a minimum value and then increases again. In addition, with increasing ψ_i, the minimum value of ψ also increases, and the point at which this minimum occurs approaches the equator.

If $\psi_i \geq 70^o$ the minimum wave normal angle is reached so close to the equator that ψ may be able to increase up to $+90^o$, when the rays

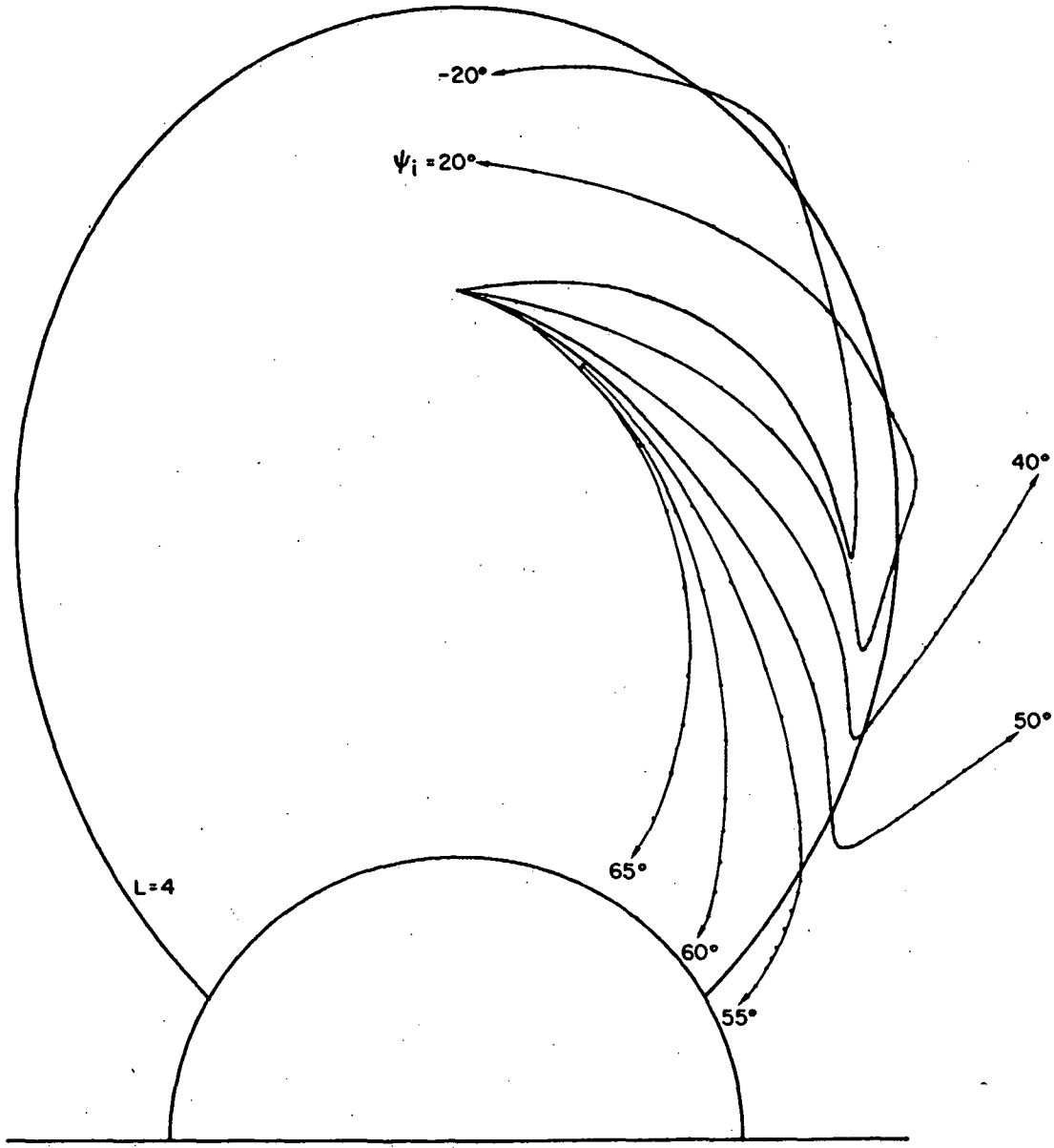

FIGURE 33a. RAY PATHS OF 600 Hz WAVES STARTING IN THE EQUATORIAL PLANE AT L = 3 FOR DIFFERENT VALUES OF THE INITIAL WAVE NORMAL ANGLE ψ_i. The field line at L = 4 marks the position of a simulated plasmapause. The rays corresponding to ψ_i between 40^o and 50^o escape from the plasmasphere.

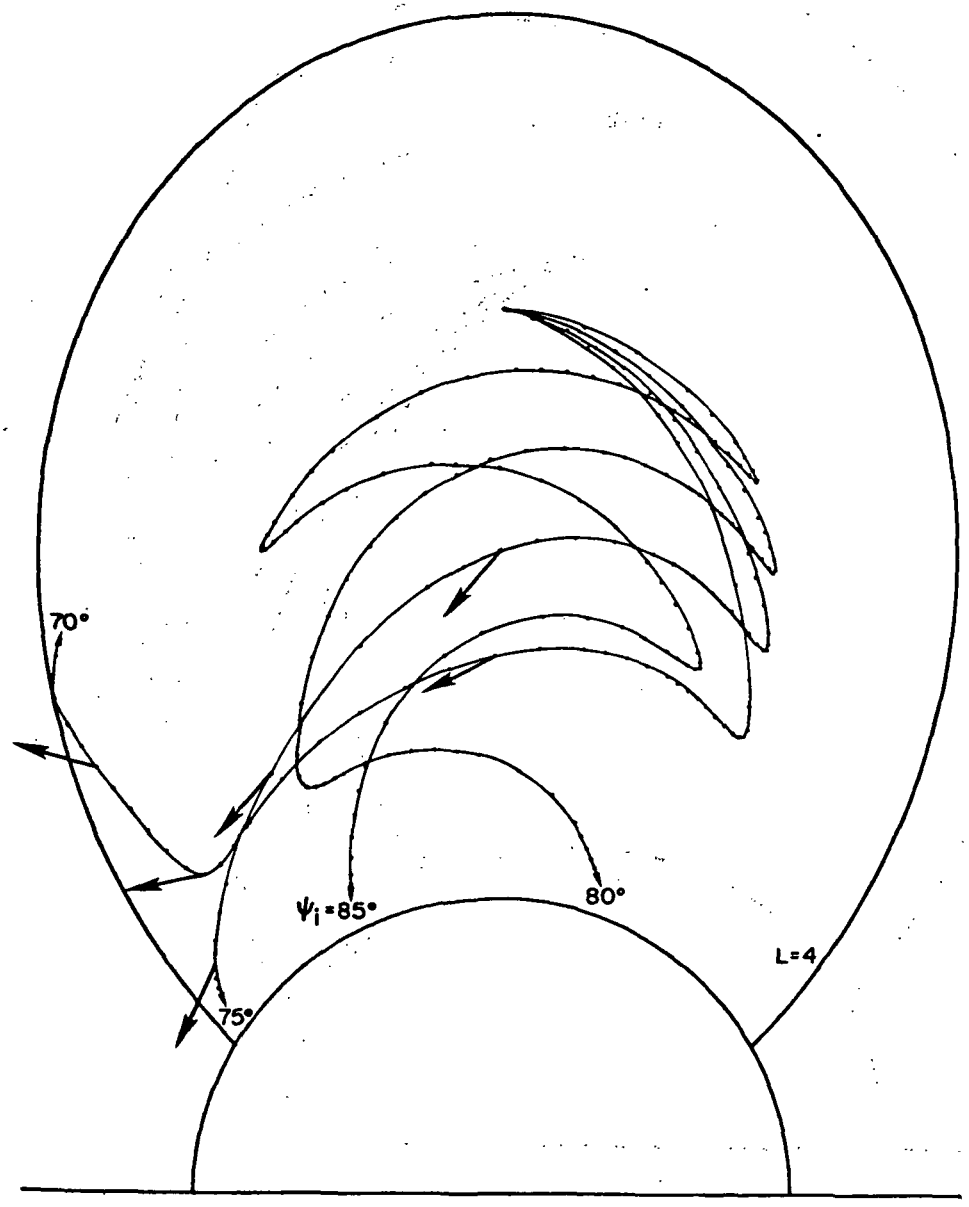

FIGURE 33b. ADDITIONAL RAYS FOR ψ_i BETWEEN 70^o AND 85^o. The arrows indicate wave normals at several points along the rays corresponding to ψ_i equal to 70^o and 75^o.

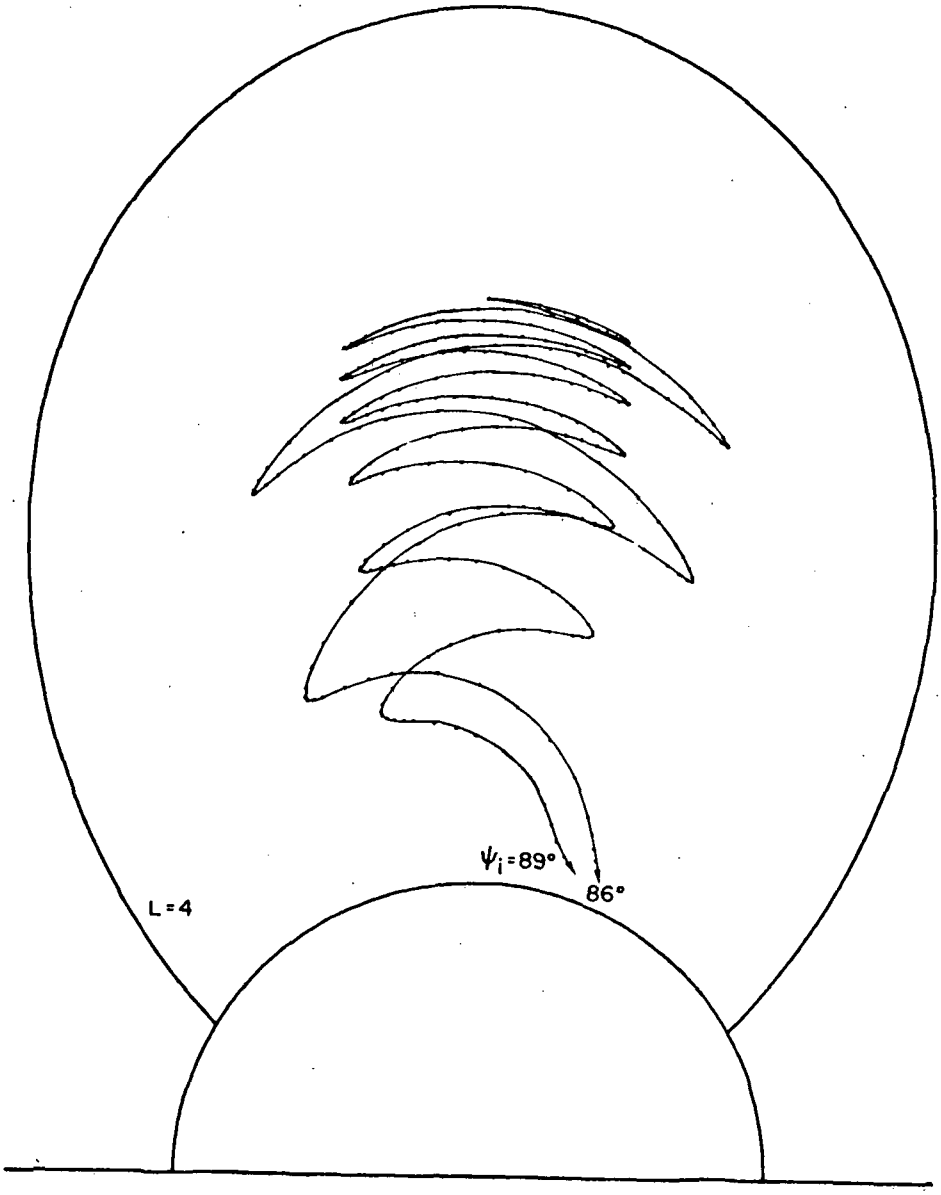

FIGURE 33c. RAYS CORRESPONDING TO ψ_i EQUAL TO 86° AND 89°. In order to reach latitudes below 30° at OGO-4 altitudes, the initial wave normal angles have to be larger than 75°.

will be refracted inward producing the kind of raypaths illustrated in Fig. 33b. For these raypaths, each time the equatorial plane is crossed the wave normal moves closer to the geomagnetic field direction (ψ decreases) and it may happen that after a few zig-zags, the equatorial value of ψ will be so low as to cause the next refraction to be upward (as for $\psi_i = 70^o$ in Fig. 33b after the first refraction). If the initial wave normal angle is sufficiently large ($\psi_i > 75^o$ in the figure) the rays will bounce back and forth across the equatorial plane on their way down and these are the only rays capable of reaching latitudes less than $\sim 30^o$ (Figure 33b,c; the wave normals corresponding to $\psi_i = 70^o$ and 75^o are indicated by arrows in Fig. 33b). Although the initial wave normal angles have to be large, the wave normal angles at low altitudes will be influenced by the ionospheric density gradients and can assume different values.

2. Erosion

In order to understand the distribution of energy around the equator, ray tracings were made at intervals $\Delta\psi_i = 0.1^o$ from 85.5^o up to 89^o. Two frequencies were used, 500 Hz and 600 Hz and the results are plotted in Fig. 34 as latitudes of arrival (at 700 km altitude) vs initial wave normal angles. The points distribute themselves in two groups on both sides of the equator and for a uniform increase in ψ_i there are sudden jumps from one hemisphere to the other. This defocusing effect produces an attenuation of signals across the equator, as observed in the satellite recordings. It is possible to make a rough estimate of the relative intensity of the signals by assuming that the intensity is inversely proportional to the spacing between adjacent points. For the distribution points in Fig. 34 the result is shown in Fig. 35, where intensities (in an arbitrary linear scale) are plotted vs the absolute

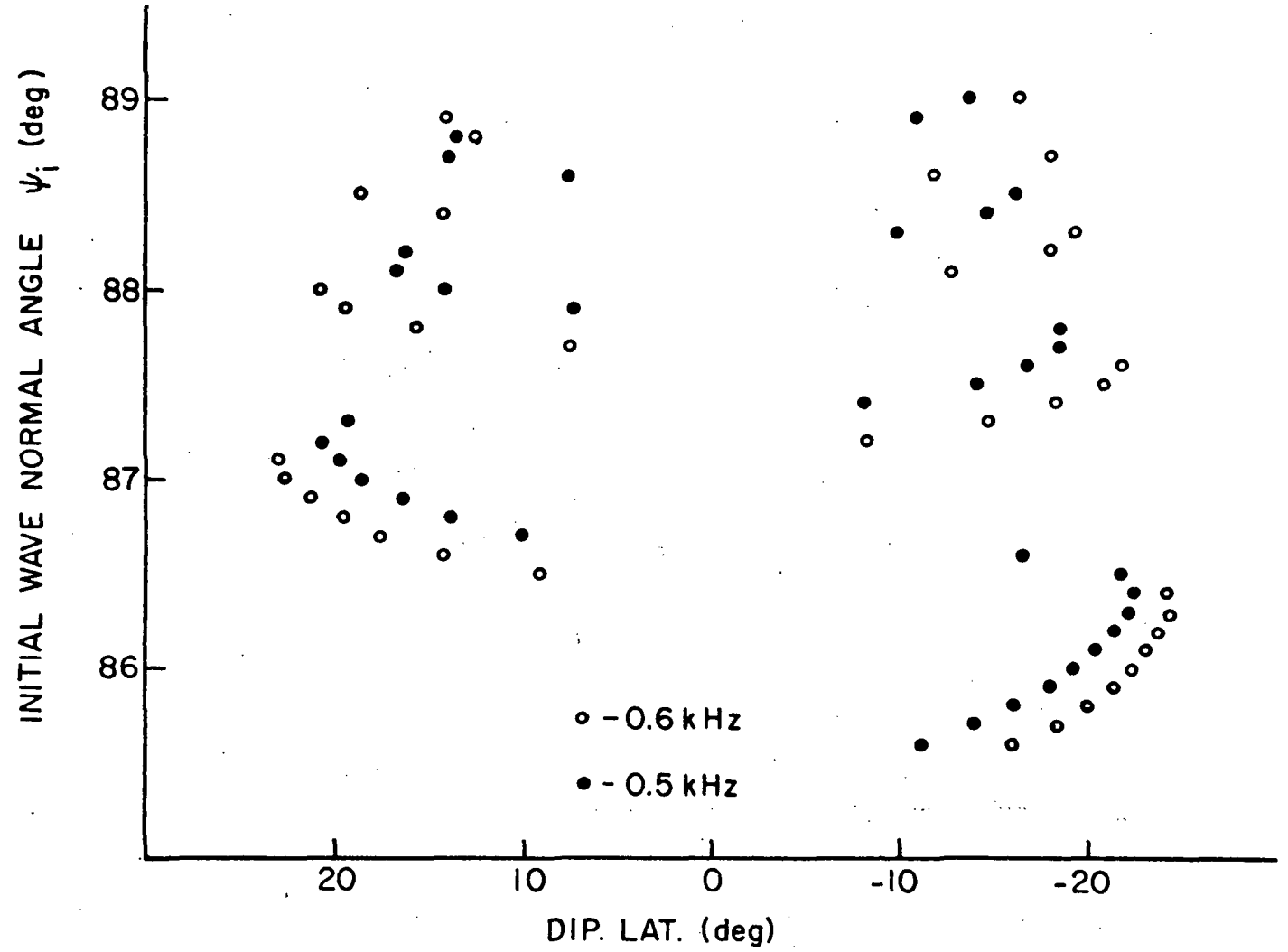

FIGURE 34. LATITUDES OF ARRIVAL OF RAYS AS IN FIG. 33, AS A FUNCTION OF INITIAL WAVE NORMAL ANGLE ψ_i. Two frequencies were used (500 and 600 Hz) and ψ_i was varied in steps of 0.1^o from 85.5^o to 89^o.

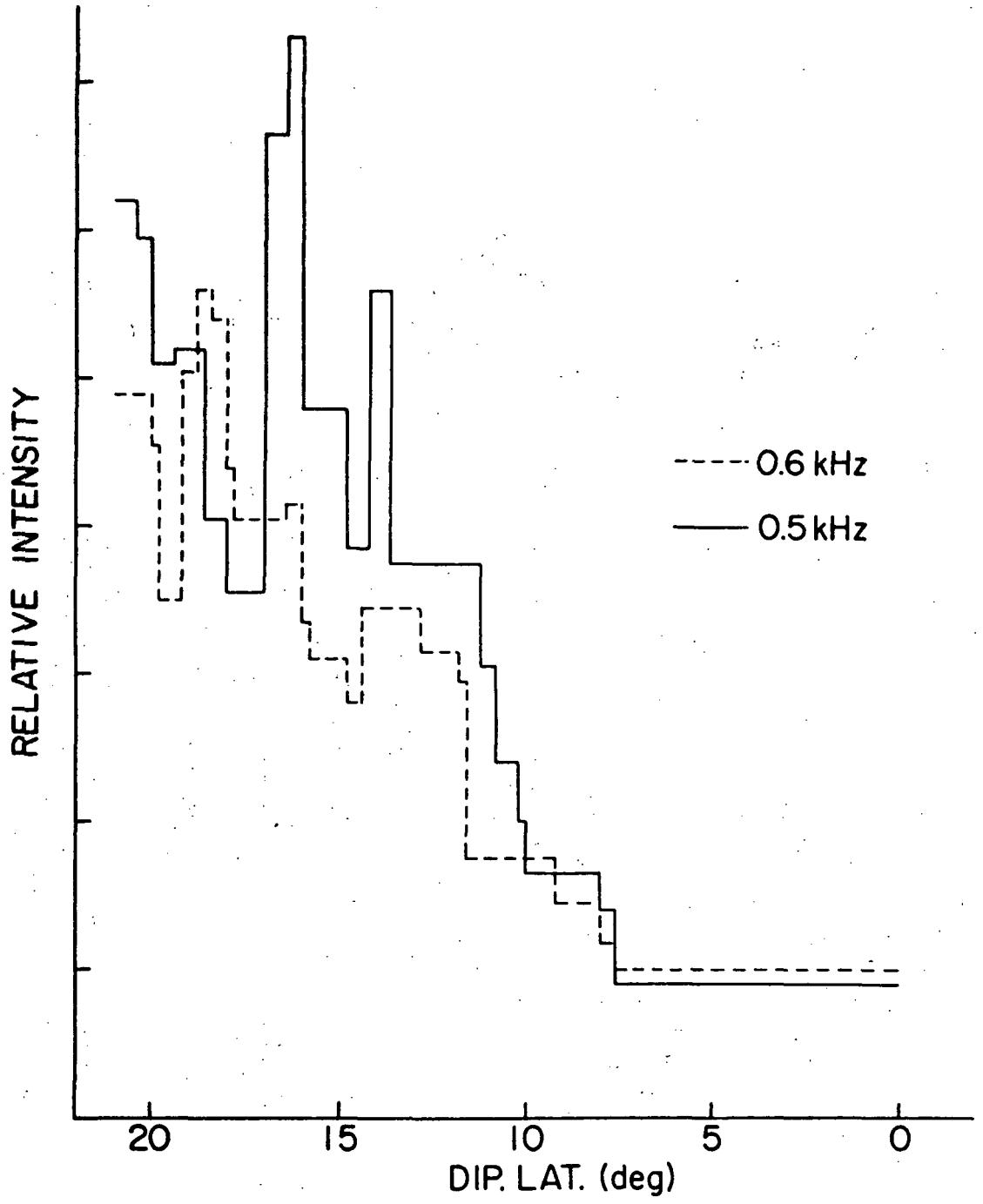

FIGURE 35. RELATIVE INTENSITIES OBTAINED FROM THE DISTRIBUTION OF POINTS OF FIG. 34 VS DIPOLE LATITUDE. The variation in intensity is consistent with the equatorial erosion.

value of dipole latitude. The irregularities in the resulting curves are due to the utilization of the discrete (and small) number of points from Fig. 34. If a larger number of points had been used, the intensity vs latitude curves of Fig. 35 would be smoother and also their slope would be steeper. Nonetheless, from $\sim 10^{o}$ to $\sim 17^{o}$ the intensity for 500 Hz is consistently higher than the one for 600 Hz, and a receiver with a constant threshold sensitivity in this range of frequencies (as in OGO 4) would observe an erosion as in Fig. 26.

3. Upper Cutoff

Another characteristic of the BLH reported here is the apparent constancy of the upper cutoff frequency observed in spectrograms from the broadband receivers. However, when examining the amplitude data from the sweeping receivers one sometimes notices a slight displacement (variable from pass to pass) of the upper cutoff toward higher frequencies with increasing latitudes. This displacement is, however, much smaller than the corresponding variation of the lower cutoff. To illustrate that displacement the outputs of the band 1 sweeping receiver corresponding to parts of three OGO-4 passes are shown in Fig. 36. For each of the passes the consecutive sweeps are shown closely spaced in order to enhance their differences. Latitudes increase toward the bottom of the figure and the mentioned displacement is quite noticeable, mainly in the pass of 22 February 2200 LT. The sharpness of the upper cutoff is also variable and for the pass of 27 December it has a slope ranging from 8 to 15 dB/100 Hz. In the sample of 14 passes examined, this slope varied between 8 and 20 dB/100 Hz, while the lower cutoff was usually steeper (between 15 and 50 dB/100 Hz).

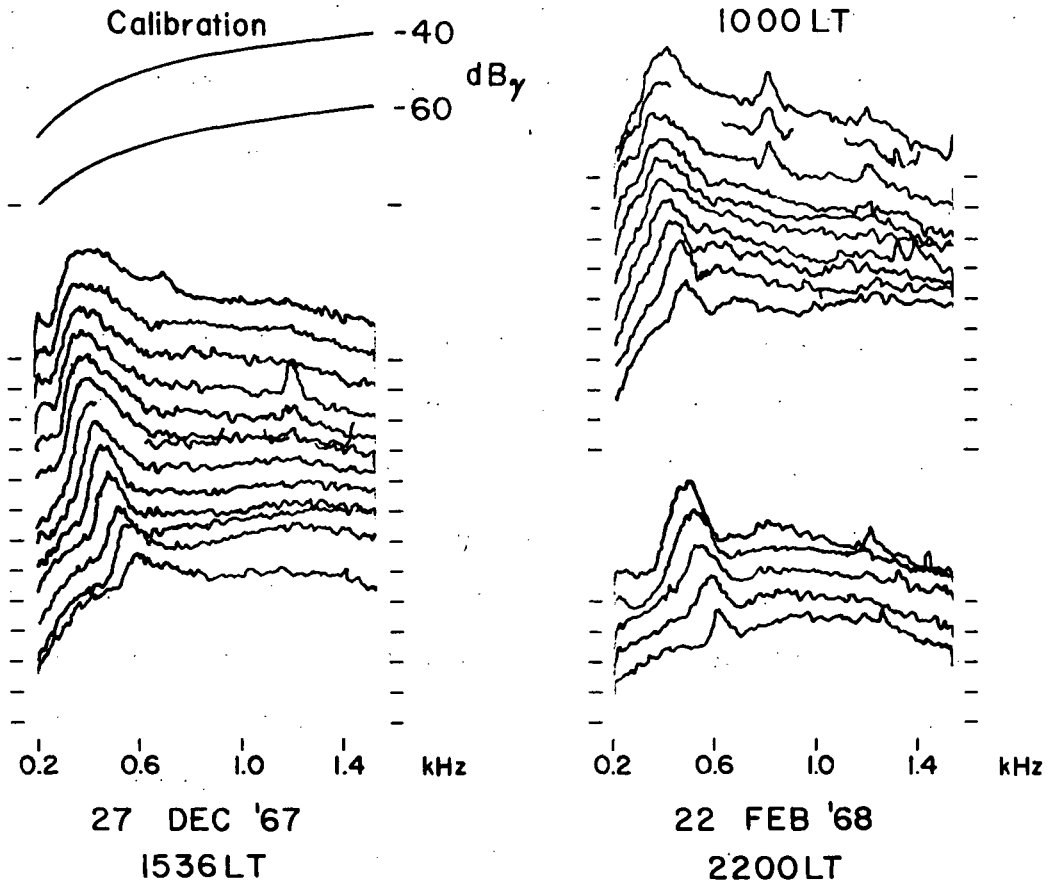

FIGURE 36. REPRODUCTION OF BAND 1 SWEEPING RECEIVER OUTPUTS FOR PART OF THREE OGO-4 PASSES. Subsequent sweeps are reproduced closely spaced in order to enhance the variations in shape of the BLH. Latitudes increase toward the bottom of the page and one can notice a slight displacement of the upper cutoff toward higher frequencies with increasing latitudes.

The upper cutoff of the BLH can also be understood if the source is located in the equatorial plane. The ray tracings of Fig. 33, starting at $L = 3$, were intended to illustrate the general behavior of rays inside the plasmasphere and they indicate the need for large initial wave normal angles in order to reach latitudes less than $\sim 30^{o}$ at low altitudes. If the source altitude is varied, however, the behavior of rays will not differ much from those illustrated. In the discussion of the erosion effect it was mentioned that the refractive index surfaces corresponding to the waves propagating toward lower L shells in Fig. 33 were closed. (The LHR frequency at $L = 3$ in the equatorial plane is ~ 750 Hz.) It is necessary that the surfaces be closed in order to produce the sudden refraction characteristic of the zig-zag ray paths, otherwise the wave normal angle could never attain 90^{o}. When the frequency is increased past the equatorial or initial value of the LHR, the refractive index surfaces become open in that region but it is still possible to generate zig-zag ray paths provided the ratio $(f/f_{LHR})_{initial}$ is not much greater than unity. This is so because the rays will be moving away from the quatorial plane approximately along magnetic field lines and the local magnetic field intensity will increase quite rapidly (and the f_{LHR} with it). Soon a point will be reached where the local f_{LHR} becomes larger than the wave frequency and the refractive index surfaces will be closed again. From the results of ray tracings with frequencies that obey the above condition it was found that when the frequency is increased:

1. There is an increase in the minimum value of initial wave normal angle (ψ_i) necessary to generate a zig-zag raypath down to OGO-4 altitudes.
2. For this minimum value of ψ_i, the latitude of arrival of the rays also increases slightly.

However, as the frequency is increased above the LHR frequency the resonance angle (where the refractive index $\mu \rightarrow \infty$) decreases. Actually when ψ_i becomes larger than ψ_m (defined as the value of ψ for which the product $\mu\cos\psi$ is minimum) the rays begin to move toward larger L shells and are not able to reach low altitudes and low latitudes. If the source of the hiss is in the equatorial plane, therefore, a low altitude satellite like OGO 4 will observe an upper cutoff (somewhat above the LHR frequency at the generating region) that should increase slightly with latitude. In the examples of Fig. 33 with the origin at $L = 3$ this upper cutoff happens above 1 kHz. In order to obtain a cutoff close to 600 Hz the source has to be moved to a higher altitude. If the source is moved to $L = 4$ the equatorial value of the LHR frequency is reduced to approximately 320 Hz. Some rays were actually traced for a frequency of 600 Hz starting at that altitude and it was found impossible to make any rays arrive at latitudes lower than 50° and low altitudes. A source close to $L = 4$ would, therefore produce a hiss band with characteristics similar to the observed BLH and its upper cutoff would be essentially independent of the magnetic latitude and local conditions at the satellite.

The observed decrease of the upper cutoff of the BLH shown in Fig. 29 would also be understood, in the context of the present interpretation, as an outward drift of the generation region during periods of very low magnetic activity.

4. Leakage from Plasmasphere

Transmission of rays to regions outside the plasmasphere can occur for initial wave normal angles ψ_i varying from 40° to 50° as shown in Fig. 33a. This result may be used to explain the observations of

Russell et al. [1969] of daytime occurrences of "steady noise" outside the plasmasphere between 40^{o} and 50^{o} dipole latitude. The rays with $\psi_i < 40^{o}$ are refracted back to the plasmasphere by the steep density gradient that constitutes the plasmapause and are trapped inside. The ray path corresponding to $\psi_i = 55^{o}$ is bent downward, also by the gradient at the plasmapause, and if $\psi_i > 55^{o}$ the rays are confined within the plasmasphere. Even when the rays were started at higher altitudes, as mentioned in the previous section, the leakage to the outside across the plasmapause could still be observed around $\sim 45^{o}$ dipole latitude.

5. Direction of Poynting Flux

In his study of the direction of poynting flux using data from the Injun 5 satellite, Mosier [1971] reported the occurrence of downgoing ELF hiss over a range of invariant latitudes from $\sim 40^{o}$ to more than 70^{o} (across the plasmapause). The highest invariant latitude at which he observed the poynting flux of the hiss directed upward was about 60^{o} (approximately the plasmapause location) and during daytime these occurrences were always above 1500 km. Again, from the ray paths in Fig. 33a, it can be concluded that below ~ 3000 km and outside the plasmasphere the rays are always propagating downward, but in the plasmasphere rays propagating both downward and upward are encountered (Fig. 33b). If $70^{o} \leq \psi_i \leq 75^{o}$ for example, some rays were traced and refracted upward at altitudes as low as 2500 km. With a nighttime density model this altitude was easily lowered to 1200 km, using frequencies as high as 900 Hz. As mentioned before, the wave normal angles at low altitudes are sensitive to density gradients and are, therefore, dependent on the model used.

D. GENERATION MECHANISMS

The characteristics of the BLH presented and discussed in previous sections suggest a source location near the equatorial plane in the vicinity of $L = 4$ and the necessity of large initial wave normal angles. In this section we discuss briefly two possible generation mechanisms and make a simple estimate of the energy levels and particle numbers that can reproduce the measured values of hiss intensity.

The two most popular radiation mechanisms to explain VLF and ELF emissions from the magnetosphere are Cerenkov and Doppler-shifted cyclotron (DSC) radiation from electrons trapped in the earth's magnetic field (Ellis [1957]; Gallet [1959]; Gallet and Helliwell [1959]; Dowden [1962,1963]; Mackenzie [1963,1967]; Bell and Buneman [1964]; Brice [1964]; Liemohn [1965]; Kennel [1966]; Kennel and Thorne [1967]; Helliwell [1967]; Mansfield [1967]; Jørgensen [1968]; Melrose [1968]; Russell and Thorne [1970]; Trulsen and Fejer [1970]). Without going into details of the radiation processes (see above references) the conditions for Cerenkov (or Landau) and DSC resonance between waves and electrons can be described by the following expressions [Liemohn, 1965]:

$$\mu\cos\psi = \frac{1}{\beta_{\parallel}} \quad \text{for Cerenkov (or Landau) resonance}$$

$$\mu\cos\psi = \frac{1}{\beta_{\parallel}} \left(1 - m \frac{f_H}{\gamma f}\right) \quad \text{for DSC resonance}$$

In these expressions μ is the wave refractive index, ψ is the wave normal angle of the emitted radiation, $\beta_{\parallel}$ is the parallel component of the normalized particle velocity $\left(\beta = \frac{v}{c}\right)$, f_H is the electron gyrofrequency, f is the frequency of the radiation, $\gamma = (1 - \beta^2)^{-1/2}$ accounts for relativistic effects and m is an integer (the case $m = 0$

corresponds to the Cerenkov emission). When $\frac{f_H}{\gamma f} > 1$, the emission is either in the forward or the backward hemisphere depending on the sign of the integer m. If $m \leq 0$ the emission is in the forward hemisphere (c sψ and β of the same sign) and if $m > 0$ the emission is in the backward hemisphere (cosψ and β of opposite signs) as illustrated in Fig. 37.

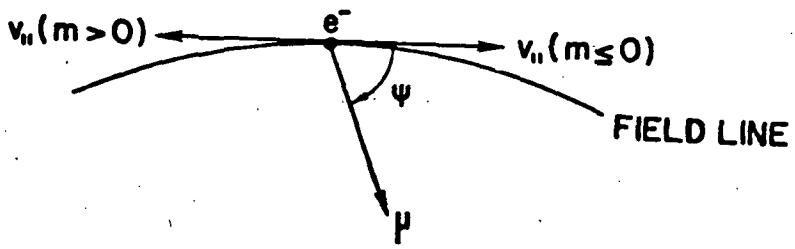

FIGURE 37. RELATIVE POSITIONS OF THE PARALLEL COMPONENT OF THE VELOCITY OF THE EMITTING ELECTRON AND THE WAVE NORMAL, IN A MAGNETIC MERIDIAN PLAN, FOR THE CASE OF CERENKOV (OR LANDAU) RESONANCE (m = 0) AND DOPPLER SHIFTED CYCLOTRON RESONANCES ($m \gtrless 0$).

For the range of frequencies encountered in the BLH and the source location discussed here (near L = 4) the product $\mu\cos\psi$ can be as low as 18 due to the large wave normal angles involved. If one considers the Cerenkov process the above expression for the condition of resonance indicates electron energies of the order of 1 kev On the other hand the DSC mechanism will involve electron energies near 1 Mev.

Expressions for computing the power emitted by a single electron on the Cerenkov and DSC mechanisms can be found elsewhere (see Mansfield

[1967]; Melrose [1968]; Trulsen and Fejer [1970]). The quantity computed is the power radiated per frequency interval (dP/df) as a function of the particle velocity components v and $v_\perp$, respectively parallel and perpendicular to the earth's magnetic field, and the characteristics of the medium. For a frequency of 400 Hz and a wave normal $\psi_i = 87^o$ in the equatorial plane at $L = 3.8$ we found:

1. For the Cerenkov mechanism:

$$\text{electron energy: } 0.56 \text{ kev}$$

$$\frac{dP}{df} \doteq 4. \times 10^{-34} \text{ watts/Hz}$$

2. For the DSC mechanism:

$$\text{electron energy: } 780 \text{ kev}$$

$$\frac{dP}{df} \doteq 1. \times 10^{-34} \text{ watts/Hz}$$

The emitted power per electron is of the same order of magnitude in both mechanism. Frank [1968] indicates omni-directional electron fluxes (0.3 to 3 kev) of 2×10^9 el/cm^2 sec around $L = 4$. For the high energy particles ($E > 500$ kev) Vernov et al. [1969] indicate intensities of about 6×10^6 el/cm^2 sec. Comparing these two intensities and considering the differences in particle velocities, the number density of the low energy electrons will be from 10^4 to 3×10^4 times larger than that of the high energy electrons.

Taking the above value of dP/df obtained for the Cerenkov emission mechanism, the power flux emitted by a single electron can be computed. By comparing this result with the power fluxes measured by OGO 4, an estimation of the order of magnitude of the number of emitting electrons can be made. In a frequency interval Δf each electron radiates through an annulus subtending a wave normal angle $\Delta\psi$ around ψ_i but only a small

segment of this annulus, pointing toward the earth, will contribute to the power received by the satellite. Taking for instance a segment of 2^{o} (that is, considering wave normals slightly off the meridian plane) and making the conservative assumption that only rays starting inside this segment will propagate down to OGO-4 altitudes it is possible to estimate the area ΔA illuminated by this segment of spherical zone at OGO-4 altitudes for a given frequency band Δf and the corresponding $\Delta\psi$. (The rays off the meridian plane were traced utilizing a three-dimensional computer ray tracing program developed by F. Walter.) Taking for Δf the bandwidth of the band 1 sweeping receiver (40 Hz) the area ΔA is found to be

$$\Delta A \doteq 3.6 \times 10^{11} \text{ m}^2$$

which corresponds to an emitted power flux per electron (S_E) of

$$S_E \doteq 2.5 \times 10^{-46} \text{ watts/m}^2$$

From the intensity found in the BLH at low latitudes ($\sim 5 \times 10^{-6}$ γ^2/Hz, Fig. 31a,b) and assuming a value of 50 for the refractive index, the measured power flux on the same 40-Hz bandwidth is found to be of the order of:

$$S_M \doteq 4 \times 10^{-10} \text{ watts/m}^2$$

Assuming that the hiss is generated incoherently, the ratio of these power fluxes gives the number of emitting electrons:

$$N = \frac{S_M}{S_E} \doteq 1.6 \times 10^{36} \text{ electrons}$$

It is easily verified that this is an excessively large number, since even for a density of 10 el/cm^{-3}, it corresponds to a volume greater

than ten thousand magnetospheres. Therefore, some form of coherency in the emission generation, or wave growth, is needed to produce the observed power fluxes. It can easily be verified that similar requirements also hold for the Doppler-shifted cyclotron generation. However, a detailed study of the possibilities of wave growth in the DSC mechanism is outside the scope of this work. An excellent treatment of the problem can be found in Russell and Thorne [1970], although these authors give emphasis to small wave normal angles and frequencies higher than in the BLH.
A greater knowledge of the low energy electron fluxes in the vicinities of the plasmapause and their drifts with magnetic activity could provide a test for comparison of the two emission mechanisms.

V. CONCLUSION

A. INFLUENCE OF THE MEDIUM ON $d\psi/ds$

The study made in Chapter 2 of the problem of orientation of the wave normals established the relative importance of several factors such as the electron and ion densities, the magnitude and inclination of the earth's magnetic field on the rate of variation of the wave normal angle ψ. In the examples given, the frequency of the waves and the range of altitudes chosen put emphasis on the effects of the hydrogen ions, which are the most important in connection with the ion whistlers studied in Chapter 3.

The inclination of the magnetic field (dipole) plays a small role in the altitude range examined (450 to 2000 km) and its effect can safely be neglected, when compared to the other two terms of $d\psi/ds$. The effects of these two terms are mode dependent and can be summarized as follows:

1. The Particle Density Term

For the slow mode, it is possible to separate two altitude ranges where different contributions dominate. Below this transition altitude the important contribution is that of the electrons and the wave normal will turn toward the direction of ∇N_e. The transition altitude is situated close to the minimum of $\mu(r)$. It approaches the crossover altitude from below as the wave normal angle tends to zero. Above the transition, the important contribution is that of the hydrogen ions and the wave normal will turn toward the direction of ∇N_{H^+}. For any wave normal angle different from zero, the particle density term goes to infinity at resonance. In Appendix A, curves of $d\psi/ds$ are plotted for

the same conditions as in Figs. 8 to 11, but for a wave normal angle of 89^{o}. The decrease in the resonance altitude toward the two-ion resonance can be seen in those curves.

For the fast mode, which exists only above the two-ion cutoff altitude, there are also two regions where different contributions dominate. The transition altitude approaches the crossover altitude from above when the wave normal angle decreases to zero. Below the transition the dominant contribution comes from the hydrogen ions and the wave normal turns toward the direction of ∇N_{H^+}. Above that altitude the principal contribution is from the electrons and the wave normal turns toward the direction of ∇N_e.

2. The Term Due to the Magnitude of $\vec{B}$

For the slow mode and small wave normal angles, this term becomes important between the crossover and the proton gyrofrequency altitudes, where the refractive index varies appreciably with B. Its magnitude grows to infinity at resonance, but unlike the particle density term the sign is conserved.

In the fast mode this term is important either near the two-ion cutoff altitude (where $\frac{1}{\mu}\frac{\partial \mu}{\partial B} \rightarrow \infty$) or at large altitudes where the particle density term becomes negligible.

B. ELF HISS

Analysis of ELF and VLF data from OGO 4 from September 1967 to April 1968 revealed some features of the ELF hiss that has not been previously identified (until recently, the only special feature of the hiss that had been identified was the lower cutoff). In particular, the hiss band below approximately 600 Hz (called BLH, for band limited ELF hiss) presents the following features:

1. A lower cutoff frequency increasing with latitude, typical of downward propagating hiss and attributed to the two-ion cutoff in the dispersion relation [Gurnett and Burns, 1968].

2. An upper cutoff frequency close to 600 Hz which seems to be essentially indepeneent of latitude above $\sim 15^{o}$ or 20^{o} (cf. Fig. 26)(sometimes it can show a slight increase toward higher latitudes--cf. Fig. 36). After a prolonged period of low magnetic activity ($K_p \leq 2$) the upper cutoff frequency may decrease to approximately 420 Hz but recovers about one day after a sharp increase in K_p or a sudden commencement (Fig. 29). (The data examined did not include any period of intense magnetic activity, $K_p > 6$.)

3. The upper cutoff decreases in frequency toward the equator near 10^{o} dipole latitude (equatorial erosion)(Fig. 26). The attenuation rates in the region of erosion are in the range of 20 to 33 db at 600 Hz for a latitude change of $\sim 4^{o}$ (Fig. 31a,b).

4. The latitude of occurrence extends from $\sim 10^{o}$ up to $\sim 55^{o}$ dipole latitude, where the essentially constant upper cutoff and the increasing lower cutoff merge (cf. Fig. 28). This limiting latitude depends on the local magnetic field intensity and the satellite altitude.

5. The most frequent times of occurrence lie between 0600 and 2200 LT (when it showed up in almost every OGO-4 pass), although some occurrences have been found between 0200 and 0500 LT (with less intensity).

6. The local ionosphere has no apparent affect upon the upper cutoff frequency, which is virtually the same at conjugate points.

Between the latitudes of $\sim 10^{o}$ and $\sim 55^{o}$ the BLH contains the strongest signals in the frequency range of 0 to 3 kHz. Its intensity peaks between 40^{o} and 50^{o} dipole latitude and may reach $2 \times 10^{-4}\ \gamma^2/\text{Hz}$ during daytime ($\sim$ 1000 LT, cf. Fig. 31b). The decrease and smearing of the lower cutoff of the background hiss, observed above 58^{o} invariant latitude, is an indication of the light ion trough.

The characteristics of the BLH suggest a source location in the equatorial region near $L = 4$ and the need for large initial wave normal angles. This source location provides an explanation of:

1. The presence of the BLH at low latitudes and the equatorial erosion;

2. The nearly constant upper cutoff of BLH;

3. The daytime observation of hiss outside the plasmapause between 40^{o} and 50^{o} latitude reported by Russell et al. [1969];

4. Some observations of poynting flux direction reported by Mosier [1971].

The Cerenkov and Doppler-shifted cyclotron (DSC) generation mechanisms from trapped electrons are briefly examined as possible sources of the BLH. For the frequency range in question the electron resonance energies are of the order of 1 kev for the Cerenkov emission and close to 1 Mev for the DSC emission and the power radiated by a single electron is comparable in both mechanisms. In either case, however, some degree of coherency or amplification is necessary in order to explain the observed power fluxes. At this point it is not clear which one of the two emission processes is responsible for the BLH.

The interpretation of the upper cutoff is consistent with a decrease in the population of the generating particles inside $L = 3.5$ or $L = 4$ and an outward movement of this generating region at times of very low magnetic activity. Therefore, a correlation study between the variations in the upper cutoff of the BLH and movements of energetic electrons could aid in finding which particles are responsible for the BLH.

The conclusions of the present work do not preclude the possibility that the same mechanism that is responsible for the BLH may also be generating the background hiss. As a matter of fact, the equatorial erosion seen in the background hiss in Fig. 26 suggests exactly this. In this context, differences in particle fluxes at different altitudes could be the important factor in explaining the different hiss intensities above and below $\sim$ 600 Hz.

C. SUGGESTIONS FOR FUTURE WORK

Based on the analysis and interpretation of OGO-4 ELF hiss observations (and the BLH in particular) presented here, the following topics are recommended for further study:

1. The variation of the upper cutoff of the BLH with magnetic activity. The study made in Chapter 4 was limited by the availability of good data at times of very strong and very weak activity. The question of the time lag between particular magnetic fluctuations and the corresponding effects on the upper cutoff needs to be ascertained more accurately.
2. The variations of the amplitude of the BLH with local time. The results shown in Fig. 32 are preliminary (only 14 satellite passes were examined). Also the variations of amplitude of the BLH with magnetic activity should be examined.
3. Correlation of the properties of ELF hiss with fluxes and movements of energetic particles (electrons) near the plasmapause This study can help clarify the question of which particles are responsible for the observed hiss bands.

A great deal can be learned about the above problems by an extensive analysis, on a global scale, of amplitude data recorded by the PCM receivers of OGO 4.

The possibilities of physical bunching or emission coherency should also be investigated together with an examination of the required lifetime of the emitting particles.

4. Correlation of the smearing and disappearance of the lower cutoff of the ELF hiss at higher latitudes and the plasmapause location. If a good correlation can be found the above phenomenon could provide a very easy and efficient way of determining the plasmapause location.

APPENDIX A. DERIVATION OF AN EXPRESSION FOR $d\psi/ds$

In what follows the medium is assumed to be lossless, so that the energy flow will be along the group velocity vector [Stix, 1962]. This direction is also called ray direction and will be denoted by s. The velocity of the wave fronts in the ray direction, or ray velocity has a magnitude related to the magnitude of the phase velocity by the expression:

$$v_R = \frac{ds}{dt} = \frac{v}{\cos\alpha} = \frac{c}{\mu\cos\alpha} \tag{A.1}$$

where α is the angle between the direction of the phase and ray velocities (see Fig. 38), and can be expressed by:

$$\tan\alpha = -\frac{1}{\mu}\left(\frac{\partial\mu}{\partial\psi}\right)_{r,\theta} \tag{A.2}$$

In the present work the earth's magnetic field (see Stix [1962]) is assumed to be a dipole. A further simplification will be made by only dealing with waves propagating in magnetic meridian planes. Polar coordinates are therefore very convenient, and the polar axis is chosen along the axis of the dipole. So at the point $P(r,\theta)$, $\vec{B}$ is the magnetic field vector and $\vec{v}$ and $\vec{v}_R$ are the phase and ray velocity vectors, respectively. The components of the ray velocity are:

$$\frac{dr}{dt} = v_R \cos(\delta + \alpha) \tag{A.3}$$

$$r\frac{d\theta}{dt} = v_R \sin(\delta + \alpha) \tag{A.4}$$

$$\frac{d\theta}{dt} = \frac{v_R}{r}\cos\alpha(\sin\delta + \tan\alpha\cos\delta)$$

and by virtue of Eqs. (A.1) and (A.2)

$$\frac{d\theta}{dt} = \frac{c}{r\mu^2}\left[\mu\sin\delta - \left(\frac{\partial\mu}{\partial\psi}\right)_{r,\theta}\cos\delta\right] \tag{A.5}$$

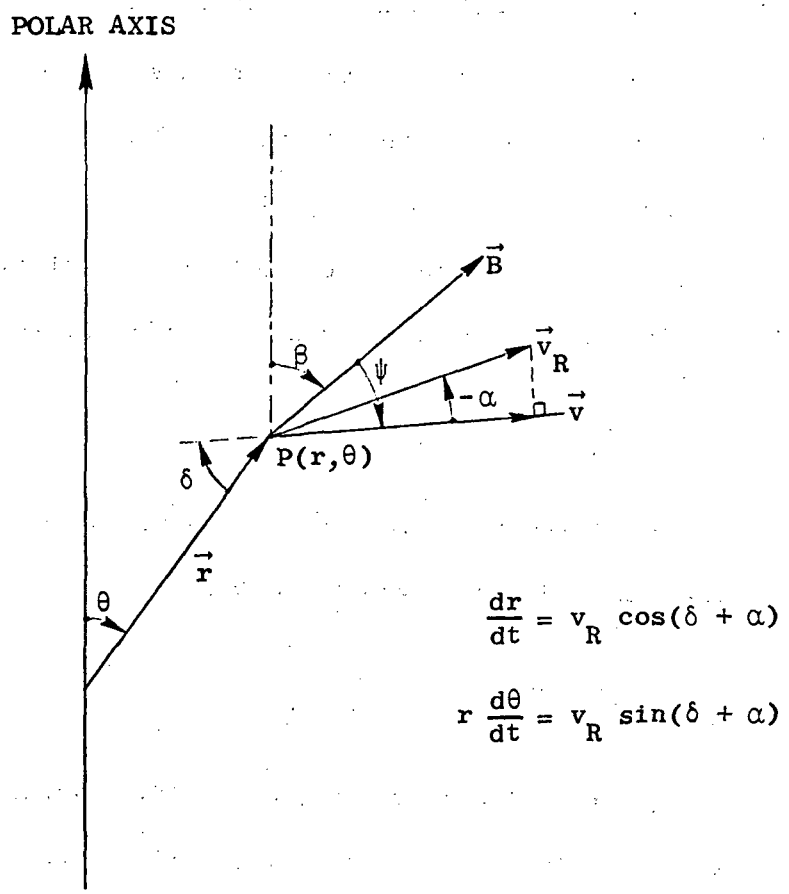

FIGURE 38. POLAR COORDINATE SYSTEM. All angles are measured clockwise from the references shown.

In Fig. 39, $\overline{AB}$ represents a small extent of a wave front at instant t, and $\overline{CD}$ is part of the same wave front after an interval Δt. If the phase speed of point A is v, after the interval Δt this point will be displaced by an amount:

$$\overline{AC} = v\, dt$$

Point B will be displaced by:

$$\overline{BD} = \left[v + \frac{dv}{d\ell}_{\phi} d\ell \right] dt$$

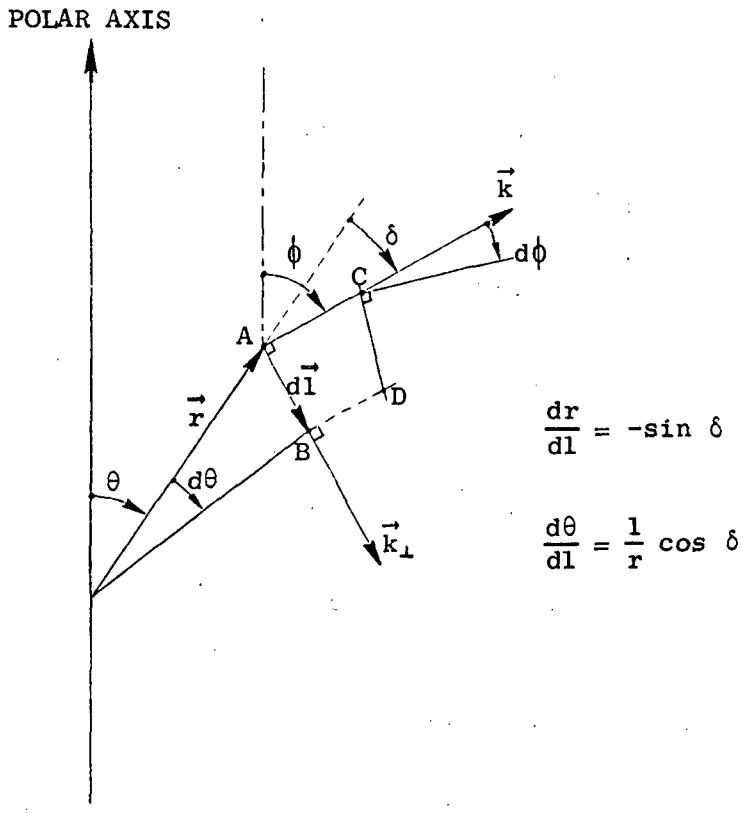

FIGURE 39. GEOMETRY OF A PROPAGATING WAVE FRONT. After a time interval Δt the wave front $\overline{AB}$ moves to $\overline{CD}$.

Therefore:

$$\tan(d\phi) \doteq d\phi = -\left(\frac{dv}{d\ell}\right)_\phi dt$$

and using the refractive index $\mu = \frac{c}{v}$:

$$\frac{d\phi}{dt} = \frac{c}{\mu^2}\left(\frac{d\mu}{d\ell}\right)_\phi \qquad (A.6)$$

It is important to note that the derivative of μ in Eq. (A.6) is obtained by keeping the wave normal direction fixed in space.

Because $\mu = \mu[r,\theta,\psi(r,\theta,\phi)]$, the term $(d\mu/d\ell)_\phi$ may be written as:

$$\left(\frac{d\mu}{d\ell}\right)_\phi = \left(\frac{\partial\mu}{\partial r}\right)_{\theta,\psi}\frac{dr}{d\ell} + \left(\frac{\partial\mu}{\partial\theta}\right)_{r,\phi}\frac{d\theta}{d\ell} + \left(\frac{\partial\mu}{\partial\psi}\right)_{r,\theta}\left[\left(\frac{\partial\psi}{\partial r}\right)_{\theta,\phi}\frac{dr}{d\ell} + \left(\frac{\partial\psi}{\partial\theta}\right)_{r,\phi}\frac{d\theta}{d\ell}\right] \qquad (A.7)$$

but $\psi = \phi - \beta$

$$\therefore \left(\frac{\partial \psi}{\partial \theta}\right)_{r,\phi} = -\left(\frac{\partial \beta}{\partial \theta}\right)_{r} \tag{A.8}$$

and for a dipole field:

$$\left(\frac{\partial \psi}{\partial r}\right)_{\theta,\phi} = 0$$

From Fig. 39 it can also be seen that:

$$\frac{dr}{d\ell} = -\sin\delta \tag{A.9}$$

and

$$\frac{d\theta}{d\ell} = \frac{1}{r}\cos\delta \tag{A.10}$$

Therefore, Eq. (A.7) can be written as:

$$\left(\frac{d\mu}{d\ell}\right)_{\phi} = -\sin\delta \left(\frac{\partial \mu}{\partial r}\right)_{\theta,\psi} + \frac{1}{r}\cos\delta \left[\left(\frac{\partial \mu}{\partial \theta}\right)_{r,\psi} - \left(\frac{\partial \mu}{\partial \psi}\right)_{r,\theta}\left(\frac{\partial \beta}{\partial \theta}\right)_{r}\right] \tag{A.11}$$

Now if the unit vectors $\hat{k}$ and $\hat{k}_{\perp}$ are defined as:

$$\hat{k} = \hat{r}\cos\delta + \hat{\theta}\sin\delta$$

$$\hat{k}_{\perp} = \hat{r}\sin\delta + \hat{\theta}\cos\delta$$

$\hat{k}$ and $\hat{k}_{\perp}$ are, respectively along the perpendicular to the wave normal direction. Consequently, Eq. (A.11) becomes:

$$\left(\frac{d\mu}{d\ell}\right)_{\phi} = (\nabla\mu)_{\psi} \cdot \hat{k}_{\perp} - \frac{1}{r}\cos\delta \left(\frac{\partial \mu}{\partial \psi}\right)_{r,\theta}\left(\frac{\partial \beta}{\partial \theta}\right)_{r} \tag{A.12}$$

Now the rate of change of the wave normal angle will be:

$$\frac{d\psi}{dt} = \frac{d\phi}{dt} - \frac{d\beta}{dt}$$

and using Eq. (A.6):

$$\frac{d\psi}{dt} = \frac{c}{\mu^2}\left(\frac{\partial \mu}{\partial \ell}\right)_{\phi} - \frac{d\beta}{dt} \tag{A.13}$$

For a dipole field

$$\frac{d\beta}{dt} = \left(\frac{\partial\beta}{\partial\theta}\right)_r \frac{d\theta}{dt}$$

and combining with Eq. (A.5):

$$\frac{d\beta}{dt} = \frac{c}{r\mu^2} \left(\frac{\partial\beta}{\partial\theta}\right)_r \left[\mu \sin\delta - \left(\frac{\partial\mu}{\partial\psi}\right)_{r,\theta} \cos\delta\right] \qquad (A.14)$$

So, from Eqs. (A.12), (A.13) and (A.14), the rate of change of the wave normal angle can be expressed as:

$$\frac{d\psi}{dt} = \frac{c}{\mu}\left[\frac{(\nabla\mu)_\psi}{\mu} \cdot \hat{k}_\perp - \frac{1}{r}\left(\frac{\partial\beta}{\partial\theta}\right)_r \sin\delta\right] \qquad (A.15)$$

Now from Eq. (A.1):

$$\frac{d\psi}{dt} = \frac{d\psi}{ds} \frac{c}{\mu \cos\alpha}$$

and again for a dipole field:

$$\frac{1}{r}\left(\frac{\partial\beta}{\partial\theta}\right)_r \sin\delta = \nabla\beta\cdot\hat{k}$$

Therefore, the rate of change of the wave normal angle along the ray path will be:

$$\frac{d\psi}{ds} = \cos\alpha \left[\frac{(\nabla\mu)_\psi}{\mu} \cdot \hat{k}_\perp - \nabla\beta\cdot\hat{k}\right]$$

The gradient of μ at a constant ψ may be written in terms of the electron and ion densities and the magnitude of the magnetic field, so:

$$\frac{d\psi}{ds} = \cos\alpha\left[\sum_j \frac{1}{\mu}\frac{\partial\mu}{\partial N_j} \nabla N_j\cdot\hat{k}_\perp + \frac{1}{\mu}\frac{\partial\mu}{\partial\beta} \nabla\beta\cdot\hat{k}_\perp - \nabla\beta\cdot\hat{k}\right] \qquad (A.16)$$

It is interesting to note that, if the direction of $\hat{k}_\perp$ had been chosen to be $\psi - \pi/2$ instead of $\psi + \pi/2$, the vector $\hat{k}_\perp$ would be written as:

$$\hat{k}_\perp = \hat{r}\sin\delta - \hat{\theta}\cos\delta$$

and the expression for $d\psi/ds$ would be:

$$\frac{d\psi}{ds} = -\cos\alpha\left[\sum_j \frac{1}{\mu}\frac{\partial\mu}{\partial N_j}\nabla N_j\cdot\hat{k}_\perp + \frac{1}{\mu}\frac{\partial\mu}{\partial\beta}\nabla\beta\cdot\hat{k}_\perp + \nabla\beta\cdot\hat{k}\right]$$

as in Cerisier [1967].

APPENDIX B. MAGNETOSPHERE DENSITY MODEL

The magnetosphere density model is composed of electrons and the ions of hydrogen, helium and oxygen. Electrons and ions are in diffusive equilibrium along lines of the earth's magnetic field (see Angerami and Thomas [1964]). The temperature is assumed to be the same for all particles. The electron density N_e at a given point $P(r,\theta)$ (see Fig. 40) depends only on its value at a reference level r_o along the same magnetic field line. Because of this constraint, the latitudinal variations of density may be described at this reference level by a function $n(\theta_E)$ of the magnetic colatitude θ_E of the base of the field line in question. In other words:

$$N_e(r_o,\theta_o) = N_{e_o} \cdot n(\theta_E) \tag{B.1}$$

in which N_{e_o} is a constant.

Therefore, given a point $P(r,\theta)$, the corresponding colatitude at the base of the field line is immediately determined:

$$\theta_E = \theta_E(r,\theta) \tag{B.2}$$

and the electron density at the point will be:

$$N_e(r,\theta) = N_{e_o} \cdot n(\theta_E) \cdot n_D(r,\theta_E) \tag{B.3}$$

where $n_D(r,\theta_E)$ is a function describing the radial dependence (diffusive equilibrium) and also eventual latitudinal variations in composition and temperature. If the composition and temperature are to be constant with latitude this last function will simply be:

$$n_D(r,\theta_E) = n_D(r) \tag{B.4}$$

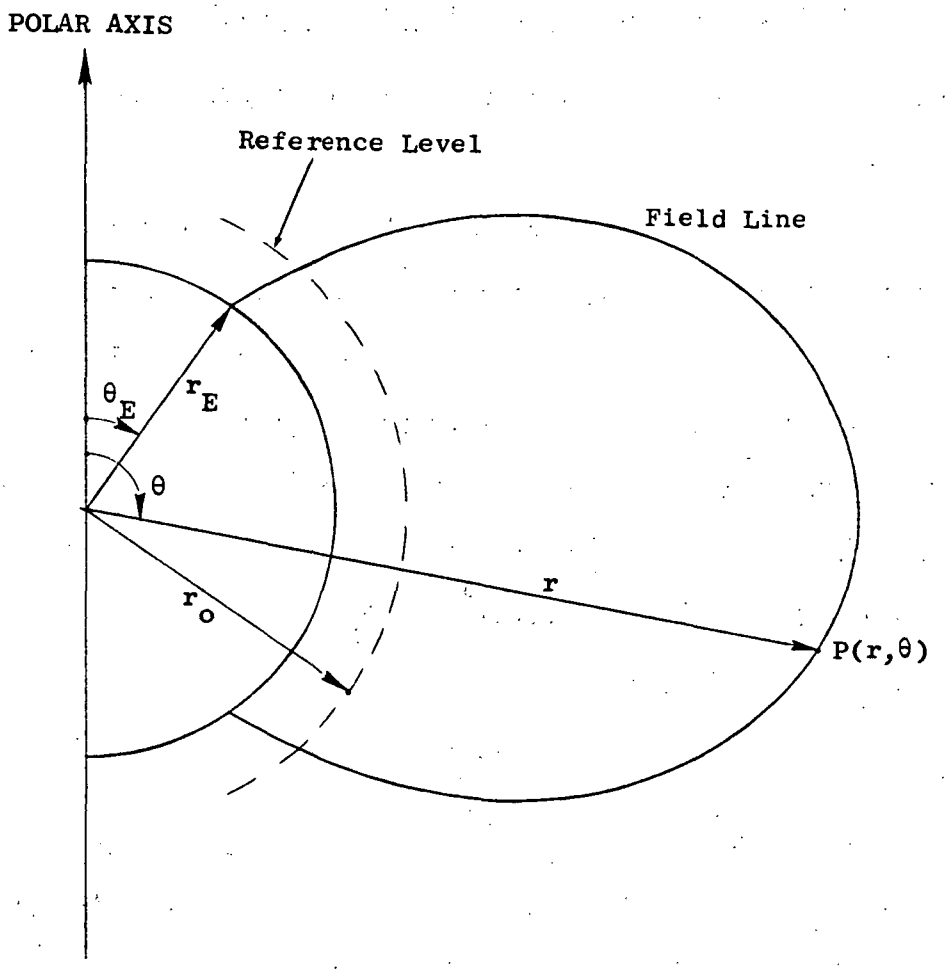

FIGURE 40. COORDINATES FOR THE IONOSPHERE MODEL (DIFFUSIVE EQUILIBRIUM ALONG FIELD LINES).

The relation implicit in Eq. (B.2) is given by:

$$\sin^2\theta_E = \frac{r_E}{r}\sin^2\theta = \frac{1}{L} \qquad \text{(B.5)}$$

where r_E is the earth's radius and L is the McIlwain shell parameter. The function n_D may be expressed in terms of the relative ion composition (see Angerami and Thomas [1964]):

$$n_D = \left[\sum_{i'} \alpha_{o_i} \cdot e^{-z/H_i}\right]^{1/2} \qquad \text{(B.6)}$$

where:

$z = r_o(1 - \frac{r_o}{r})$ is the geopotential height(neglecting the centrifugal force)

$\alpha_{o_i} = \alpha_{o_i}(\theta_E)$ is the relative concentration of the i^{th} ion species at the reference level and may be variable with latitude

$H_i = \frac{KT}{m_i g_o}$ is the scale height of the i^{th} neutral species

K is the Boltzmann constant

T is the electron and ion temperature

g_o is the acceleration of gravity ft r_o

Due to the electrical neutrality of the medium:

$$\sum_i \alpha_{o_i} = 1$$

The ion densities will then be:

$$N_i = \alpha_i \cdot N_e \tag{B.7}$$

where:

$$\alpha_i = \frac{\alpha_{o_i} \cdot e^{-z/H_i}}{n_D^2} \tag{B.8}$$

and also:

$$\sum_i \alpha_i = 1$$

Therefore, from Eq. (B.3) the derivatives of the electron density may be written as:

$$\frac{1}{N_e}\frac{\partial N_e}{\partial r} = \frac{1}{n_D}\frac{\partial n_D}{\partial r} + \frac{1}{n}\frac{\partial n}{\partial \theta_E}\frac{\partial \theta_E}{\partial r} \tag{B.9}$$

$$\frac{1}{N_e}\frac{\partial N_e}{\partial \theta} = \frac{1}{n_D}\frac{\partial n_D}{\partial \theta} + \frac{1}{n}\frac{\partial n}{\partial \theta_E}\frac{\partial \theta_E}{\partial \theta} \tag{B.10}$$

and for the ions:

$$\frac{1}{N_i}\frac{\partial N_i}{\partial r} = \frac{1}{N_e}\frac{\partial N_e}{\partial r} + \frac{1}{\alpha_i}\frac{\partial \alpha_i}{\partial r} \tag{B.11}$$

$$\frac{1}{N_i}\frac{\partial N_i}{\partial \theta} = \frac{1}{N_e}\frac{\partial N_e}{\partial \theta} + \frac{1}{\alpha_i}\frac{\partial \alpha_i}{\partial \theta} \tag{B.12}$$

The derivatives of θ_E in Eqs. (B.9) and (B.10) can be obtained from Eq. (B.5):

$$\frac{\partial \theta_E}{\partial r} = -\frac{1}{2r\cdot(L-1)^{1/2}} \tag{B.13}$$

$$\frac{\partial \theta_E}{\partial \theta} = \frac{1}{\tan\theta\cdot(L-1)^{1/2}} \tag{B.14}$$

(It is important to note that $\theta_E \leq \pi/2$.)

The derivatives of the function n_D appearing in Eqs. (B.9) and (B.10) can be obtained from Eq. (B.6):

$$\frac{1}{n_D}\frac{\partial n_D}{\partial r} = \frac{1}{2n_D^2}\sum_i \left[\frac{\partial \alpha_{o_i}}{\partial \theta_E}\frac{\partial \theta_E}{\partial r} - \frac{\alpha_{o_i}}{H_i}\left(\frac{r_o}{r}\right)^2\right] e^{-z/H_i} \tag{B.15}$$

$$\frac{1}{n_D}\frac{\partial n_D}{\partial \theta} = \frac{1}{2n_D^2}\sum_i \frac{\partial \alpha_{o_i}}{\partial \theta_E}\frac{\partial \theta_E}{\partial \theta} e^{-z/H_i} \tag{B.16}$$

also:

$$\frac{1}{\alpha_i}\frac{\partial \alpha_i}{\partial r} = -\frac{1}{H_i}\left(\frac{r_o}{r}\right)^2 - \frac{2}{n_D}\frac{\partial n_D}{\partial r} + \frac{1}{\alpha_{o_i}}\frac{\partial \alpha_{o_i}}{\partial \theta_E}\frac{\partial \theta_E}{\partial r} \tag{B.17}$$

$$\frac{1}{\alpha_i}\frac{\partial \alpha_i}{\partial \theta} = \frac{1}{\alpha_{o_i}}\frac{\partial \alpha_{o_i}}{\partial \theta_E}\frac{\partial \theta_E}{\partial \theta} \tag{B.18}$$

In order to completely determine the model it is necessary to specify the functions $n(\theta_E)$ and $\alpha_{o_i}(\theta_E)$, which describe, respectively, the variations of electron density and composition with latitude. Throughout the present work, the composition is made constant with latitude,

e.g., $\alpha_{o_i}(\theta_E)$ = constant. The function that represents the latitudinal variations in electron density, on the other hand, is made out of the product of two other functions n_G and n_K that reproduce the so-called equatorial anomaly and the "knee" or plasmapause. These functions are, respectively:

$$n_G = 1 + A \cdot \exp\left[-\frac{1}{2}\left(\frac{\theta_{peak} - \theta_E}{\sigma} \right)^2 \right] \tag{B.19}$$

$$n_K = B + C \cdot \mathrm{erf}\left(\frac{\theta_E - \theta_K}{2\sqrt{\gamma}} \right) \tag{B.20}$$

and they are reproduced in Fig. 41a,b, with the values of the constants used in the examples. The function n_G is a gaussian curve, and the function n_K is made with the so-called "error function." Their derivatives which appear in Eq. (B.9) and Eq. (B.10) can be written:

$$\frac{1}{n_G} \frac{\partial n_G}{\partial \theta_E} = \left(1 - \frac{1}{n_G} \right) \left(\frac{\theta_{peak} - \theta_E}{\sigma^2} \right) \tag{B.21}$$

$$\frac{1}{n_K} \frac{\partial n_K}{\partial \theta_E} = \frac{c}{n_K \sqrt{\pi\gamma}} \exp\left[-\left(\frac{\theta_E - \theta_K}{2\sqrt{\gamma}} \right)^2 \right] \tag{B.22}$$

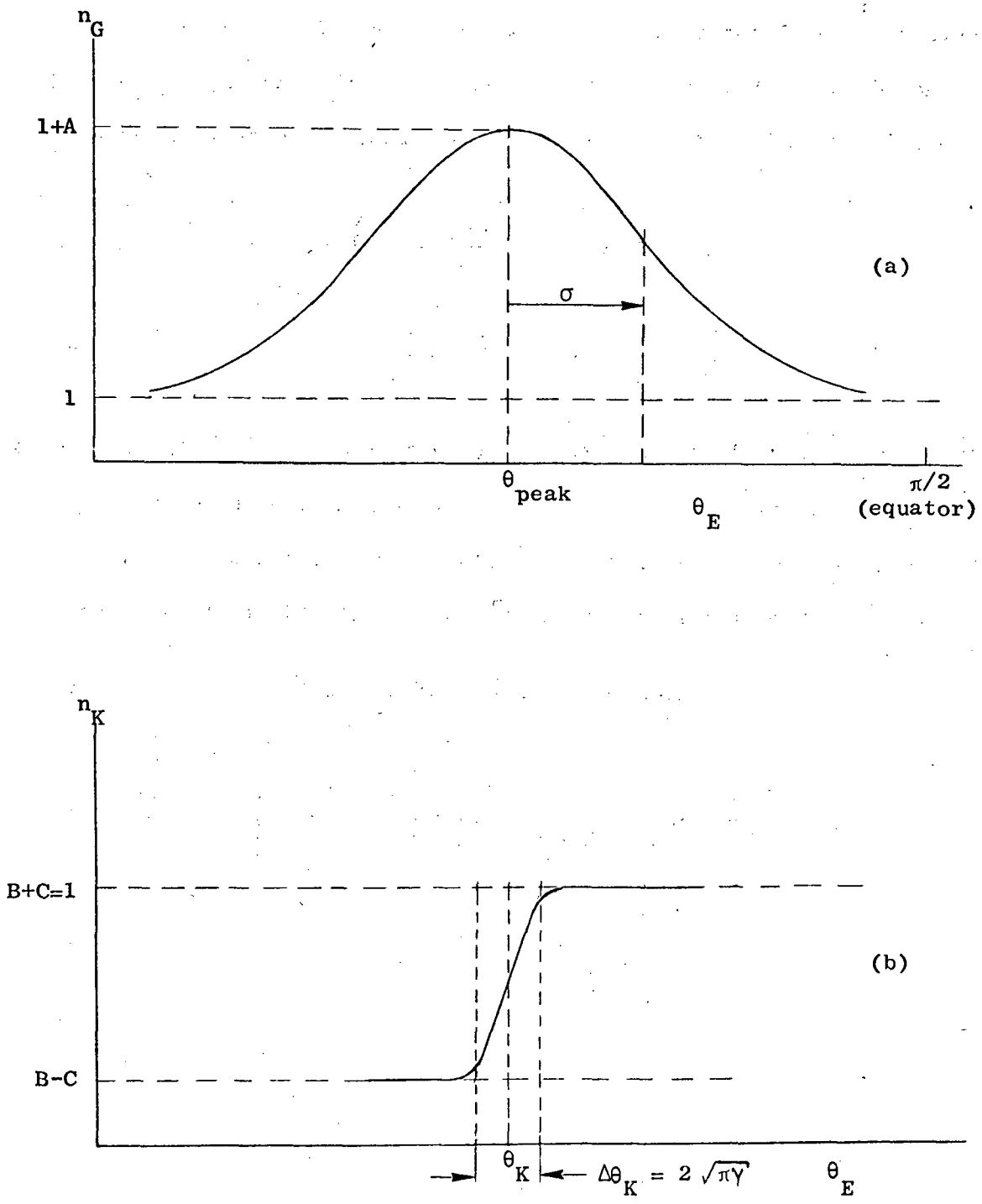

FIGURE 41a,b. FUNCTIONS USED TO SIMULATE THE EQUATORIAL ANOMALY (a) AND THE PLASMAPAUSE (b) IN THE MODEL IONOSPHERE.

APPENDIX C. DERIVATION OF EXPRESSIONS FOR $\partial\mu/\partial N_j$ AND $\partial\mu/\partial B$

The refractive index μ satisfies the following equation:

$$\tan^2\psi \left[(1-R/\mu^2)^{-1} + (1-L/\mu^2)^{-1} - 2 \right] + 2 \left[(1-P/\mu^2)^{-1} - 1 \right] = 0 \tag{C.1}$$

where the quantities R, L and P have been defined in Chapter 2. In other words:

$$\mu = \mu(R,L,P,\psi) \tag{C.2}$$

Therefore:

$$\frac{\partial\mu}{\partial N_j} = \frac{\partial\mu}{\partial R}\frac{\partial R}{\partial N_j} + \frac{\partial\mu}{\partial L}\frac{\partial L}{\partial N_j} + \frac{\partial\mu}{\partial P}\frac{\partial P}{\partial N_j} \tag{C.3}$$

where:

$$\frac{\partial R}{\partial N_j} = -\frac{R_j}{N_j}\ ; \quad \frac{\partial L}{\partial N_j} = -\frac{L_j}{N_j}; \quad \frac{\partial P}{\partial N_j} = -\frac{X_j}{N_j} \tag{C.4}$$

Consequently:

$$\frac{1}{\mu}\frac{\partial\mu}{\partial N_j} = -\frac{1}{N_j}\left(\frac{1}{\mu}\frac{\partial\mu}{\partial R} R_j + \frac{1}{\mu}\frac{\partial\mu}{\partial L} L_j + \frac{1}{\mu}\frac{\partial\mu}{\partial P} X_j \right) \tag{C.5}$$

Similarly:

$$\frac{\partial\mu}{\partial B} = \frac{\partial\mu}{\partial R}\frac{\partial R}{\partial B} + \frac{\partial\mu}{\partial L}\frac{\partial L}{\partial B} \tag{C.6}$$

where:

$$\frac{\partial R}{\partial B} = -\sum_j \frac{\partial R_j}{\partial B} = \frac{1}{B}\sum_j \frac{\epsilon_j Y_j}{X_j} R_j^2\ ; \quad \frac{\partial L}{\partial B} = -\sum_j \frac{\partial L_j}{\partial B} = -\frac{1}{B}\sum_j \frac{\epsilon_j Y_j}{X_j} L_j^2 \tag{C.7}$$

Consequently:

$$\frac{1}{\mu}\frac{\partial\mu}{\partial B} = \frac{1}{B}\sum_j \frac{\epsilon_j Y_j}{X_j}\left(\frac{1}{\mu}\frac{\partial\mu}{\partial R} R_j^2 - \frac{1}{\mu}\frac{\partial\mu}{\partial L} L_j^2 \right) \tag{C.8}$$

The derivatives of μ with respect to R, L and P can be easily obtained from Eq. (C.1) above:

$$\frac{1}{\mu}\frac{\partial\mu}{\partial R} = \frac{1/2}{R + \left(\frac{\mu^2-R}{\mu^2-L}\right)^2 L + \left(\frac{\mu^2-R}{\mu^2-P}\right)^2 \cdot 2P\ \text{cotan}^2\psi} \qquad (C.9)$$

Analogously:

$$\frac{1}{\mu}\frac{\partial\mu}{\partial L} = \frac{1/2}{L + \left(\frac{\mu^2-L}{\mu^2-R}\right)^2 R + \left(\frac{\mu^2-L}{\mu^2-P}\right)^2 \cdot 2P\ \text{cotan}^2\psi} \qquad (C.10)$$

$$\frac{1}{\mu}\frac{\partial\mu}{\partial P} = \frac{1}{2P + \left[\left(\frac{\mu^2-P}{\mu^2-R}\right)^2 R + \left(\frac{\mu^2-P}{\mu^2-L}\right)^2 L\right] \tan^2\psi} \qquad (C.11)$$

Limits of the above derivatives at resonance ($\mu \to \infty$). The condition for resonance can be found from Eq. (C.1):

$$\tan^2\psi = -\frac{P}{S}$$

where $S = \frac{1}{2}(R + L)$ (see Stix [1962]). Therefore, at resonance (and for $\psi \neq 0$):

$$\lim_{\mu\to\infty} \frac{1}{\mu}\frac{\partial\mu}{\partial R} = \frac{1/2}{R + L - 2S} \to \infty$$

$$\lim_{\mu\to\infty} \frac{1}{\mu}\frac{\partial\mu}{\partial L} = \frac{1/2}{R + L - 2S} \to \infty$$

and

$$\lim_{\mu\to\infty} \frac{1}{\mu}\frac{\partial\mu}{\partial P} = \frac{1}{2P - \frac{2SP}{S}} \to \infty$$

So, at resonance (and $\psi \neq 0$):

$$\frac{1}{\mu}\frac{\partial\mu}{\partial N_j} \to -\infty$$

If, on the other hand $\psi = 0$:

$$\mu^2 = L$$

So

$$\frac{1}{\mu}\frac{\partial \mu}{\partial L} = \frac{1}{2L} \; ; \quad \frac{1}{\mu}\frac{\partial \mu}{\partial R} = \frac{1}{\mu}\frac{\partial \mu}{\partial P} = 0$$

and therefore:

$$\frac{1}{\mu}\frac{\partial \mu}{\partial N_j} = - \lim_{L_j \to \infty} \frac{L_j}{2N_j L} = - \lim_{L_j \to \infty} \frac{L_j}{2N_j\left(1 - L_j - \sum_{i \neq j} L_i\right)}$$

Consequently, if $\psi = 0$ at resonance:

$$\frac{1}{\mu}\frac{\partial \mu}{\partial N_j} = \frac{1}{2N_j}$$

From the above limits and Eq. (C.8) it can be seen that, for any wave normal angle:

$$\frac{1}{\mu}\frac{\partial \mu}{\partial B} \Rightarrow \pm \infty \quad (\text{if} \quad R_j^2 \gtrless L_j^2)$$

at resonance.

APPENDIX D. CURVES OF THE COMPONENTS OF $d\psi/ds$ FOR THE SAME CONDITIONS AS IN CHAPTER 2, BUT FOR $\psi = -89^{o}$

The following curves in Figs. 42 to 45 represent the several terms of $d\psi/ds$ for both propagating modes in the same conditions as illustrated in Figs. 7 to 10 in Chapter 2, but for a large wave normal angle ($\psi = -89^{o}$). The main differences from the small wave normal example examined in Chapter 2 are in the slow mode, due to the decrease of the resonance level to an altitude below the crossover altitude. If $\psi = 90^{o}$ this resonance level would have been reduced to the two-ion resonance level also marked in the figures. In this example, the tendency of the particle density term toward infinity at resonance (see Fig. 42) is more apparent than in the case of small wave normal angle.

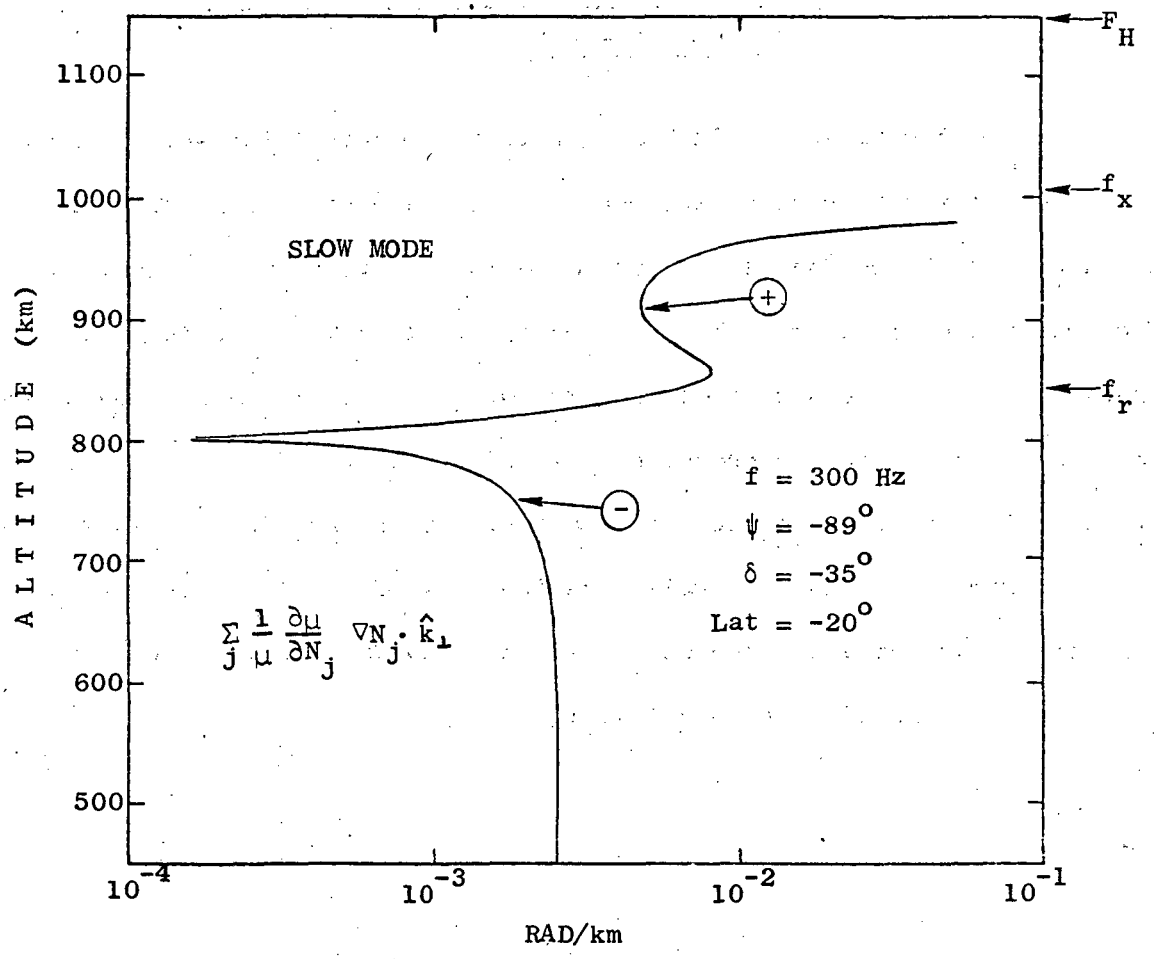

FIGURE 42. CURVES OF THE COMPONENT OF $d\psi/ds$ DUE TO THE ELECTRON AND ION DENSITIES (N_j), FOR A WAVE PROPAGATING IN THE SLOW MODE.

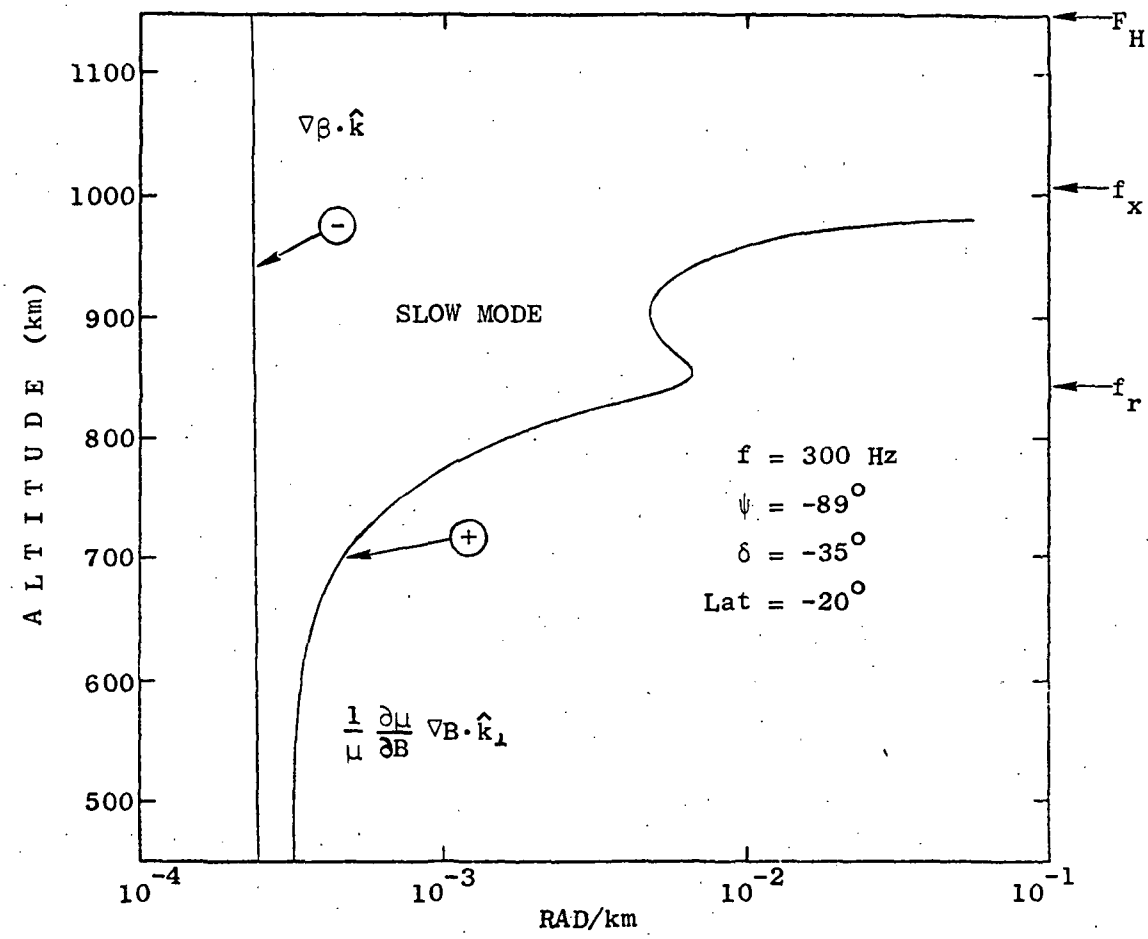

FIGURE 43. CURVES OF THE COMPONENTS OF $d\psi/ds$ DUE TO THE MAGNITUDE (B) AND INCLINATION (β) OF THE EARTH'S MAGNETIC FIELD, FOR A WAVE PROPAGATING IN THE SLOW MODE.

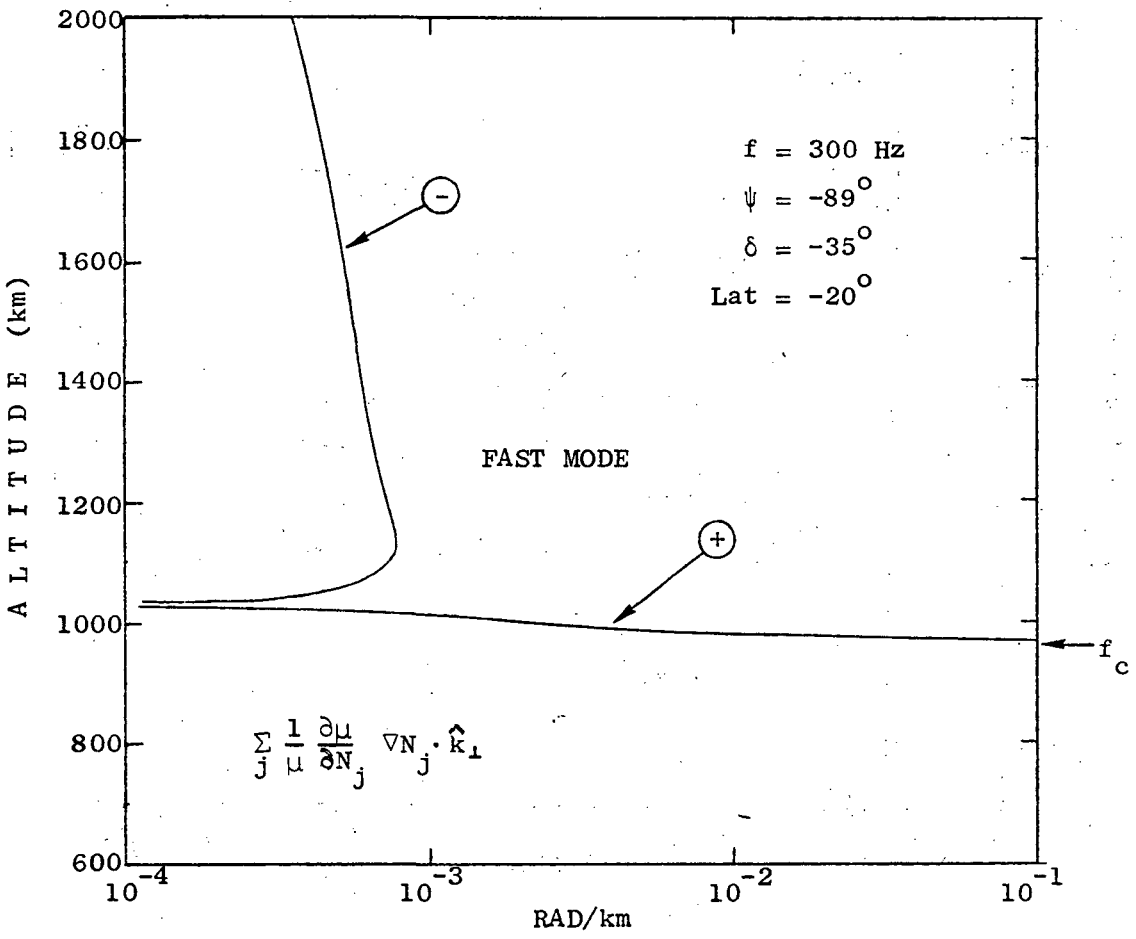

FIGURE 44. CURVES OF THE COMPONENT OF $d\psi/ds$ DUE TO THE ELECTRON AND ION DENSITIES (N_j), FOR A WAVE PROPAGATING IN THE FAST MODE.

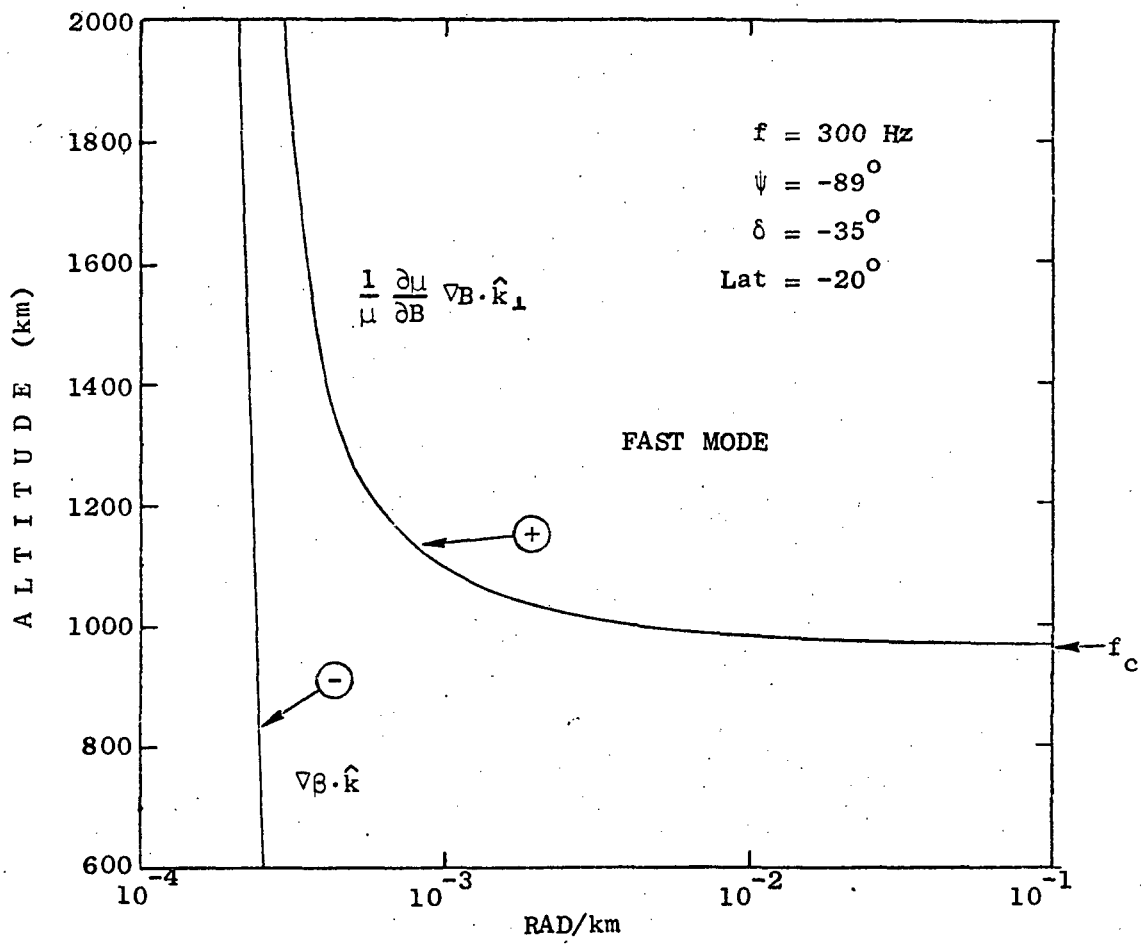

FIGURE 45. CURVES OF THE COMPONENTS OF $d\psi/ds$ DUE TO THE MAGNITUDE (B) AND INCLINATION (β) OF THE EARTH'S MAGNETIC FIELD, FOR A WAVE PROPAGATING IN THE FAST MODE.

REFERENCES

Angerami, J. J. and J. O. Thomas, Studies of planetary atmospheres, 1, the distribution of electrons and ions in the earth's exosphere, J. Geophys. Res., 69, 4537, 1964.

Barrington, R. E., J. S. Belrose and W. E. Mather, A helium whistler observed in the Canadian satellite Alouette 2, Nature, 210, 80 1966.

Bell, T. F. and O. Buneman, Plasma instability in the whistler mode caused by a gyrating electron stream, Phys. Rev., 5A, A1300, 1964.

Brice, N. M., Fundamentals of very low frequency emission generation mechanisms, J. Geophys. Res., 69, 4515, 1964.

Budden, K. G., Radio Waves in the Ionosphere, Cambridge University Press, Cambridge, England, 1961.

Cerisier, J. C., Accessibilite par propagation aux resonances tres basse frequency dans l'ionosphere, Ann. de Geophys., 23, 249, 1967.

Dowden, R. L., Theory of generation of exospheric very low frequency noise (hiss), J. Geophys. Res., 67, 2223, 1962.

Dowden, R. L., Doppler shifted cyclotron generation of exospheric very low frequency noise (hiss), Planet. Space Sci., 11, 361, 1963.

Dunckel, N. and R. A. Helliwell, Whistler-mode emissions on the OGO-1 satellite, J. Geophys. Res., 74, 6371, 1969.

Ellis, G. R. A., Low frequency radio emission from aurorae, J. Atmos. Terr. Phys., 10, 302, 1957.

Frank, L. A., On the distribution of low energy protons and electrons in the earth's magnetosphere, Earth's Particles and Fields, ed. B. M. McCormac, Reinhold Book Corp., New York, 1968.

Gallet, R. M., The very low frequency emissions generated in the earth's exosphere, Proc. IRE, 47, 211, 1959.

Gallet, R. M. and R. A. Helliwell, Origin of very low frequency emissions, J. Res. NBS, 63D, 21, 1959.

Gurnett, D. A. and B. Burns, The low frequency cutoff of ELF emissions, J. Geophys. Res., 73, 7437, 1968.

Gurnett, D. A., S. D. Shawhan, N. M. Brice and R. L. Smith, Ion cyclotron whistlers, J. Geophys. Res., 70, 1665, 1965.

Guthart, H., T. L. Crystal, B. P. Ficklin, W. E. Blair and T. J. Yung, Proton gyrofrequency band emissions observed aboard OGO-2, J. Geophys. Res., 73, 3592, 1968.

Haselgrove, J., Ray theory and a new method for ray tracing, Physics of the Ionosphere, Physical Society, London, 355, 1955.

Helliwell, R. A., A theory of discrete VLF emissions from the magnetosphere, J. Geophys. Res., 72, 4773, 1967.

Helliwell, R. A., J. H. Crary, J. P. Katsufrakis and M. L. Trimpi, The Stanford University real-time spectra analyzer, Tech. Rept. No. 10, Radioscience Lab., Stanford Electronics Labs., Stanford University, Stanford, Calif., Nov. 1961.

Jones, D., The theory of the effect of collisions on ion-cyclotron whistlers, Plasma Waves in Space and Laboratory, eds., J. O. Thomas and B. F. Landmark, Edinburgh University Press, Edinburgh, 1969a.

Jones, D., The effect of the latitudinal variation of the terrestrial magnetic field strength on ion cyclotron whistlers, J. Atmos. & Terr. Phys., 31, 971, 1969b.

Jørgensen, T. S., Interpretation of auroral hiss measured on OGO-2 and at Byrd Station in terms of incoherent Cerenkov radiation, J. Geophys. Res., 73, 1055, 1968.

Kennel, C. F., Low-frequency whistler mode, Phys. Fluids, 9, 2190, 1966.

Kennel, C. F. and R. M. Thorne, Unstable growth of unducted whistlers propagating at an angle to the geomagnetic field, J. Geophys. Res., 72, 871, 1967.

Kimura, I., Effects of ions on whistler-mode ray tracing, Radio Science, 1(new series), 269, 1966.

Laaspere, T., W. C. Johnson and L. C. Sempribon, Observations of auroral hiss, LHR noise, and other phenomena in the frequency range 20 Hz to 540 kHz on OGO-6, J. Geophys. Res., 76, 4477, 1971.

Liemohn, H. B., Radiation from electrons in magnetoplasma, Radio Science, 69D, 741, 1965.

Mansfield, V. N., Cerenkov and cyclotron radiation as VLF emission sources, Astrophys. J., 147, 672, 1967.

McKenzie, J. F., Cerenkov radiation in a magneto-ionic medium (with application to the generation of low frequency electromagnetic radiation in the exosphere by the passage of charged corpuscular streams), Phil. Trans. Roy. Soc., London, A255, 585, 1963.

McKenzie, J. F., Radiation losses from a test particle in a plasma, Phys. Fluids, 10, 2680, 1967.

Melrose, D. B., The emissivity in the magneto-ionic modes, Astrophys. J., 154, 803, 1968.

Mosier, S. R., VLF measurements of the component of the poynting flux along the geomagnetic field with the Injun 5 satellite, Paper presented in Commission 4 of Spring URSI Meeting, Washington, D.C., April 1969.

Mosier, S. R., Poynting flux studies of hiss with the Injun 5 satellite, J. Geophys. Res., 76, 1713, 1971.

Muzzio, J. L. R., Reflection of whistlers in the ionosphere, Paper presented in Commission 4 of Spring URSI Meeting, Washington, D.C., April 1968a.

Muzzio, J. L. R., Ion cutoff whistlers, J. Geophys. Res., 73, 7526, 1968b.

Muzzio, J. L. R., OGO-4 observations of downcoming proton whistlers, Paper presented in Commission 4 of Spring URSI Meeting, Washington, D.C., April 1969.

Nicolet, M., The collision frequency of electrons in the ionosphere, J. Atmos. & Terr. Phys., 3, 200, 1953.

Ratcliffe, J. A., The Magneto-Ionic Theory & Its Applications to the Ionosphere, Cambridge University Press, Cambridge, 1962.

Rodriguez, P. and D. A. Gurnett, An experimental study of very-low frequency mode coupling and polarization reversal, J. Geophys. Res., 76, 960, 1971.

Rorden, L. H., L. E. Orsak, B. P. Ficklin and R. H. Stehle, Instruments for the Stanford University/Stanford Research Institute VLF experiment (4917) on the EOGO satellite, Instrument Rept., Stanford Res. Institute, Menlo Park, Calif., 1966.

Russell, C. T., R. E. Holzer and E. J. Smith, OGO-3 observations of ELF noise in the magnetosphere, 1. Spatial extent and frequency of occurrence, J. Geophys. Res., 74, 755, 1969.

Russell, C. T. and R. M. Thorne, On the structure of the inner magnetosphere, Cosmic Electrodynamics, 1., D. Reidel Publ. Co., Dordrecht-Holland, p. 67-89, 1970.

Scarabucci, R. R., Analytical and numerical treatment of wave-propagation in the lower ionosphere, Tech. Rept. 3412-11, Radioscience Lab., Stanford Electronics Labs., Stanford University, Stanford, Calif., August 1969.

Scarabucci, R. R., Satellite observations of equatorial phenomena and defocusing of VLF electromagnetic waves, J. Geophys. Res., 75, 69, 1970.

Smith, R. L. and J. J. Angerami, Magnetospheric properties deduced from OGO-1 observations of ducted and nonducted whistlers, J. Geophys. Res., 73, 1, 1968.

Smith, R. L. and N. M. Brice, Propagation in multicomponent plasmas, J. Geophys. Res., 69, 5029, 1964.

Stix, T. H., The Theory of Plasma Waves, McGraw Hill Book Co., New York, 1962.

Taylor, H. A., H. C. Brinton, D. L. Carpenter, F. M. Bonner, and R. L. Heyborne, Ion depletion in the high-latitude exosphere; simultaneous OGO-2 observations of the light ion trough and the VLF cutoff, J. Geophys. Res., 74, 3517, 1969.

Taylor, W. W. L., and D. A. Gurnett, Morphology of VLF emissions observed with the Injun 3 satellite, J. Geophys. Res., 73, 5615, 1968.

Thorne, R. M. and C. F. Kennel, Quasi-trapped VLF propagation in the outer magnetosphere, J. Geophys. Res., 72, 857, 1967.

Trulsen, J. and J. A. Fejer, Radiation from a charged particle in a magnetoplasma, J. Plasma Phys., 4, 825, 1970.

Vernov, S. N., E. V. Gortchakov, S. N. Kuznetsov, Yu. I. Logachev, E. N. Sosnovets and V. G. Stolpovsky, Particle fluxes in the outer geomagnetic field, Rev. Geophys., 7, 257, 1969.